Title
The SPTpol Extended Cluster Survey

Journal
The Astrophysical Journal Supplement Series, 247(1)

ISSN
0067-0049

Authors
Bleem, LE
Bocquet, S
Stalder, B
et al.

Publication Date
2020-03-01

DOI
10.3847/1538-4365/ab6993

Peer reviewed

DES-2019-0442
FERMILAB-PUB-19-513-AE

Draft version December 17, 2019
Typeset using LaTeX **twocolumn** style in AASTeX63

The SPTpol Extended Cluster Survey

L. E. Bleem,[1,2] S. Bocquet,[3,1,2] B. Stalder,[4,5] M. D. Gladders,[6,2] P. A. R. Ade,[7] S. W. Allen,[8,9,10] A. J. Anderson,[11] J. Annis,[11] M. L. N. Ashby,[5] J. E. Austermann,[12] S. Avila,[13] J. S. Avva,[14] M. Bayliss,[15,16] J. A. Beall,[12] K. Bechtol,[4,17] A. N. Bender,[1,2] B. A. Benson,[11,2,6] E. Bertin,[18,19] F. Bianchini,[20] C. Blake,[21] M. Brodwin,[22] D. Brooks,[23] E. Buckley-Geer,[11] D. L. Burke,[8,10] J. E. Carlstrom,[2,24,1,6,25] A. Carnero Rosell,[26,27] M. Carrasco Kind,[28,29] J. Carretero,[30] C. L. Chang,[2,1,6] H. C. Chiang,[31,32] R. Citron,[33] C. Corbett Moran,[33,34] M. Costanzi,[35,36] T. M. Crawford,[2,6] A. T. Crites,[2,6,37] L. N. da Costa,[27,38] T. de Haan,[14,39] J. De Vicente,[26] S. Desai,[40] H. T. Diehl,[11] J. P. Dietrich,[3,41] M. A. Dobbs,[31,42] T. F. Eifler,[43,44] W. Everett,[45] B. Flaugher,[11] B. Floyd,[22] J. Frieman,[11,2] J. Gallicchio,[2,46] J. García-Bellido,[13] E. M. George,[47,14] D. W. Gerdes,[48,49] A. Gilbert,[31] D. Gruen,[9,8,10] R. A. Gruendl,[28,29] J. Gschwend,[27,38] N. Gupta,[20] G. Gutierrez,[11] N. W. Halverson,[45,50] N. Harrington,[14] J. W. Henning,[1,2] C. Heymans,[51,52] G. P. Holder,[53,54,42] D. L. Hollowood,[55] W. L. Holzapfel,[14] K. Honscheid,[56,57] J. D. Hrubes,[33] N. Huang,[14] J. Hubmayr,[12] K. D. Irwin,[10,9] D. J. James,[58] T. Jeltema,[55] S. Joudaki,[59] G. Khullar,[2,6] M. Klein,[3,60] L. Knox,[61] N. Kuropatkin,[11] A. T. Lee,[14,39] D. Li,[12,10] C. Lidman,[62] A. Lowitz,[6] N. MacCrann,[56,57] G. Mahler,[48] M. A. G. Maia,[27,38] J. L. Marshall,[63] M. McDonald,[15] J. J. McMahon,[49] P. Melchior,[64] F. Menanteau,[28,29] S. S. Meyer,[2,24,6,25] R. Miquel,[65,30] L. M. Mocanu,[6,2,66] J. J. Mohr,[3,60,41] J. Montgomery,[31] A. Nadolski,[54,53] T. Natoli,[6,2] J. P. Nibarger,[12] G. Noble,[31] V. Novosad,[67] S. Padin,[2,6,37] A. Palmese,[11] D. Parkinson,[68] S. Patil,[20] F. Paz-Chinchón,[28,29] A. A. Plazas,[64] C. Pryke,[69] N. S. Ramachandra,[1,2] C. L. Reichardt,[20] J. D. Remolina González,[48] A. K. Romer,[70] A. Roodman,[8,10] J. E. Ruhl,[71] E. S. Rykoff,[8,10] B. R. Saliwanchik,[72] E. Sanchez,[26] A. Saro,[73,36,35] J.T. Sayre,[45,50] K. K. Schaffer,[2,25,74] T. Schrabback,[75] S. Serrano,[76,77] K. Sharon,[48] C. Sievers,[33] G. Smecher,[31,78] M. Smith,[79] M. Soares-Santos,[80] A. A. Stark,[5] K. T. Story,[8,9] E. Suchyta,[81] G. Tarle,[49] C. Tucker,[7] K. Vanderlinde,[82,83] T. Veach,[84] J. D. Vieira,[54,53] G. Wang,[1] J. Weller,[41,60,3] N. Whitehorn,[85] W. L. K. Wu,[2] V. Yefremenko,[1] and Y. Zhang[11]

[1] *High Energy Physics Division, Argonne National Laboratory, 9700 South Cass Avenue, Lemont, IL 60439, USA*
[2] *Kavli Institute for Cosmological Physics, University of Chicago, 5640 South Ellis Avenue, Chicago, IL 60637, USA*
[3] *Department of Physics, Ludwig-Maximilians-Universität,Scheinerstr. 1, 81679 München, Germany*
[4] *LSST, 933 North Cherry Avenue, Tucson, AZ 85721, USA*
[5] *Center for Astrophysics | Harvard & Smithsonian, 60 Garden Street, Cambridge, MA 02138, USA*
[6] *Department of Astronomy and Astrophysics, University of Chicago, 5640 South Ellis Avenue, Chicago, IL 60637, USA*
[7] *Cardiff University, Cardiff CF10 3XQ, United Kingdom*
[8] *Kavli Institute for Particle Astrophysics & Cosmology, P. O. Box 2450, Stanford University, Stanford, CA 94305, USA*
[9] *Department of Physics, Stanford University, 382 Via Pueblo Mall, Stanford, CA 94305, USA*
[10] *SLAC National Accelerator Laboratory, 2575 Sand Hill Road, Menlo Park, CA 94025, USA*
[11] *Fermi National Accelerator Laboratory, P. O. Box 500, Batavia, IL 60510, USA*
[12] *NIST Quantum Devices Group, 325 Broadway Mailcode 817.03, Boulder, CO 80305, USA*
[13] *Instituto de Fisica Teorica UAM/CSIC, Universidad Autonoma de Madrid, 28049 Madrid, Spain*
[14] *Department of Physics, University of California, Berkeley, CA 94720, USA*
[15] *Kavli Institute for Astrophysics and Space Research, Massachusetts Institute of Technology, 77 Massachusetts Avenue, Cambridge, MA 02139, USA*
[16] *Department of Physics, University of Cincinnati, Cincinnati, OH 45221, USA*
[17] *Physics Department, 2320 Chamberlin Hall, University of Wisconsin-Madison, 1150 University Avenue Madison, WI 53706-1390*
[18] *CNRS, UMR 7095, Institut d'Astrophysique de Paris, F-75014, Paris, France*
[19] *Sorbonne Universités, UPMC Univ Paris 06, UMR 7095, Institut d'Astrophysique de Paris, F-75014, Paris, France*
[20] *School of Physics, University of Melbourne, Parkville, VIC 3010, Australia*
[21] *Centre for Astrophysics & Supercomputing, Swinburne University of Technology, P.O. Box 218, Hawthorn, VIC 3122, Australia*
[22] *Department of Physics and Astronomy, University of Missouri, 5110 Rockhill Road, Kansas City, MO 64110, USA*
[23] *Department of Physics & Astronomy, University College London, Gower Street, London, WC1E 6BT, UK*
[24] *Department of Physics, University of Chicago, 5640 South Ellis Avenue, Chicago, IL 60637, USA*
[25] *Enrico Fermi Institute, University of Chicago, 5640 South Ellis Avenue, Chicago, IL 60637, USA*
[26] *Centro de Investigaciones Energéticas, Medioambientales y Tecnológicas (CIEMAT), Madrid, Spain*

Corresponding author: L. Bleem
lbleem@anl.gov

[27] *Laboratório Interinstitucional de e-Astronomia - LIneA, Rua Gal. José Cristino 77, Rio de Janeiro, RJ - 20921-400, Brazil*
[28] *Department of Astronomy, University of Illinois at Urbana-Champaign, 1002 W. Green Street, Urbana, IL 61801, USA*
[29] *National Center for Supercomputing Applications, 1205 West Clark St., Urbana, IL 61801, USA*
[30] *Institut de Física d'Altes Energies (IFAE), The Barcelona Institute of Science and Technology, Campus UAB, 08193 Bellaterra (Barcelona) Spain*
[31] *Department of Physics, McGill University, 3600 Rue University, Montreal, Quebec H3A 2T8, Canada*
[32] *School of Mathematics, Statistics & Computer Science, University of KwaZulu-Natal, Durban, South Africa*
[33] *University of Chicago, 5640 South Ellis Avenue, Chicago, IL 60637, USA*
[34] *TAPIR, Walter Burke Institute for Theoretical Physics, California Institute of Technology, 1200 E California Blvd, Pasadena 91125, CA, USA*
[35] *INAF-Osservatorio Astronomico di Trieste, via G. B. Tiepolo 11, I-34143 Trieste, Italy*
[36] *Institute for Fundamental Physics of the Universe, Via Beirut 2, 34014 Trieste, Italy*
[37] *California Institute of Technology, MS 249-17, 1216 E. California Blvd., Pasadena, CA 91125, USA*
[38] *Observatório Nacional, Rua Gal. José Cristino 77, Rio de Janeiro, RJ - 20921-400, Brazil*
[39] *Physics Division, Lawrence Berkeley National Laboratory, Berkeley, CA 94720, USA*
[40] *Department of Physics, IIT Hyderabad, Kandi, Telangana 502285, India*
[41] *Excellence Cluster Universe, Boltzmannstr. 2, 85748 Garching, Germany*
[42] *Canadian Institute for Advanced Research, CIFAR Program in Gravity and the Extreme Universe, Toronto, ON, M5G 1Z8, Canada*
[43] *Department of Astronomy/Steward Observatory, University of Arizona, 933 North Cherry Avenue, Tucson, AZ 85721-0065, USA*
[44] *Jet Propulsion Laboratory, California Institute of Technology, 4800 Oak Grove Dr., Pasadena, CA 91109, USA*
[45] *Department of Astrophysical and Planetary Sciences, University of Colorado, Boulder, CO 80309, USA*
[46] *Harvey Mudd College, 301 Platt Blvd., Claremont 91711, CA*
[47] *European Southern Observatory, Karl-Schwarzschild-Str. 2, 85748 Garching bei München, Germany*
[48] *Department of Astronomy, University of Michigan, 1085 S. University Ave, Ann Arbor, MI 48109, USA*
[49] *Department of Physics, University of Michigan, 450 Church Street, Ann Arbor, MI 48109, USA*
[50] *Department of Physics, University of Colorado, Boulder, CO 80309, USA*
[51] *Institute for Astronomy, University of Edinburgh, Royal Observatory, Blackford Hill, Edinburgh EH9 3HJ, UK*
[52] *German Centre for Cosmological Lensing (GCCL), Astronomisches Institut, Ruhr-Universität Bochum, Universitätsstr. 150, 44801 Bochum, Germany*
[53] *Department of Physics, University of Illinois Urbana-Champaign, 1110 W. Green Street, Urbana, IL 61801, USA*
[54] *Astronomy Department, University of Illinois at Urbana-Champaign, 1002 W. Green Street, Urbana, IL 61801, USA*
[55] *Santa Cruz Institute for Particle Physics, Santa Cruz, CA 95064, USA*
[56] *Center for Cosmology and Astro-Particle Physics, The Ohio State University, Columbus, OH 43210, USA*
[57] *Department of Physics, The Ohio State University, Columbus, OH 43210, USA*
[58] *Center for Astrophysics | Harvard & Smithsonian, 60 Garden Street, Cambridge, MA 02138, USA*
[59] *Department of Physics, University of Oxford, Denys Wilkinson Building, Keble Road, Oxford OX1 3RH, UK*
[60] *Max-Planck-Institut für extraterrestrische Physik,Giessenbachstr. 85748 Garching, Germany*
[61] *Department of Physics, University of California, One Shields Avenue, Davis, CA 95616, USA*
[62] *The Research School of Astronomy and Astrophysics, Australian National University, ACT 2601, Australia*
[63] *George P. and Cynthia Woods Mitchell Institute for Fundamental Physics and Astronomy, and Department of Physics and Astronomy, Texas A&M University, College Station, TX 77843, USA*
[64] *Department of Astrophysical Sciences, Princeton University, Peyton Hall, Princeton, NJ 08544, USA*
[65] *Institució Catalana de Recerca i Estudis Avançats, E-08010 Barcelona, Spain*
[66] *Institute of Theoretical Astrophysics, University of Oslo, P.O.Box 1029 Blindern, N-0315 Oslo, Norway*
[67] *Materials Sciences Division, Argonne National Laboratory, 9700 South Cass Avenue, Lemont, IL 60439, USA*
[68] *Korea Astronomy and Space Science Institute, 776 Daedeokdae-ro, Yuseong-gu, Daejeon 34055, Republic of Korea*
[69] *School of Physics and Astronomy, University of Minnesota, 116 Church Street S.E. Minneapolis, MN 55455, USA*
[70] *Department of Physics and Astronomy, Pevensey Building, University of Sussex, Brighton, BN1 9QH, UK*
[71] *Physics Department, Center for Education and Research in Cosmology and Astrophysics, Case Western Reserve University, Cleveland, OH 44106, USA*
[72] *Department of Physics, Yale University, 217 Prospect Street, New Haven, CT 06511, USA*
[73] *Astronomy Unit, Department of Physics, University of Trieste, via Tiepolo 11, I-34131 Trieste, Italy*
[74] *Liberal Arts Department, School of the Art Institute of Chicago, 112 S Michigan Ave, Chicago, IL 60603, USA*
[75] *Argelander-Institut für Astronomie, Universität Bonn, Auf dem Hügel 71, 53121, Bonn, Germany*
[76] *Institut d'Estudis Espacials de Catalunya (IEEC), 08034 Barcelona, Spain*
[77] *Institute of Space Sciences (ICE, CSIC), Campus UAB, Carrer de Can Magrans, s/n, 08193 Barcelona, Spain*
[78] *Three-Speed Logic, Inc., Victoria, B.C., V8S 3Z5, Canada*

[79] School of Physics and Astronomy, University of Southampton, Southampton, SO17 1BJ, UK
[80] Brandeis University, Physics Department, 415 South Street, Waltham MA 02453
[81] Computer Science and Mathematics Division, Oak Ridge National Laboratory, Oak Ridge, TN 37831
[82] Dunlap Institute for Astronomy & Astrophysics, University of Toronto, 50 St George St, Toronto, ON, M5S 3H4, Canada
[83] Department of Astronomy & Astrophysics, University of Toronto, 50 St George St, Toronto, ON, M5S 3H4, Canada
[84] Department of Astronomy, University of Maryland College Park, MD 20742, USA
[85] Department of Physics and Astronomy, University of California, Los Angeles, CA 90095, USA

ABSTRACT

We describe the observations and resultant galaxy cluster catalog from the 2770 deg^2 SPTpol Extended Cluster Survey (SPT-ECS). Clusters are identified via the Sunyaev-Zel'dovich (SZ) effect, and confirmed with a combination of archival and targeted follow-up data, making particular use of data from the Dark Energy Survey (DES). With incomplete followup we have confirmed as clusters 244 of 266 candidates at a detection significance $\xi \geq 5$ and an additional 204 systems at $4 < \xi < 5$. The confirmed sample has a median mass of $M_{500c} \sim 4.4 \times 10^{14} M_{\odot} h_{70}^{-1}$ and a median redshift of $z = 0.49$, and we have identified 44 strong gravitational lenses in the sample thus far. Radio data are used to characterize contamination to the SZ signal; the median contamination for confirmed clusters is predicted to be $\sim$1% of the SZ signal at the $\xi > 4$ threshold, and < 4% of clusters have a predicted contamination > 10% of their measured SZ flux. We associate SZ-selected clusters, from both SPT-ECS and the SPT-SZ survey, with clusters from the DES redMaPPer sample, and find an offset distribution between the SZ center and central galaxy in general agreement with previous work, though with a larger fraction of clusters with significant offsets. Adopting a fixed *Planck*-like cosmology, we measure the optical richness-to-SZ-mass ($\lambda - M$) relation and find it to be 28% shallower than that from a weak-lensing analysis of the DES data—a difference significant at the 4 σ level—with the relations intersecting at $\lambda = 60$. The SPT-ECS cluster sample will be particularly useful for studying the evolution of massive clusters and, in combination with DES lensing observations and the SPT-SZ cluster sample, will be an important component of future cosmological analyses.

Keywords: cosmology: observations – galaxies: clusters: general – large-scale structure of universe, gravitational lensing: strong

1. INTRODUCTION

Clusters of galaxies, as tracers of the extreme peaks in the matter density field, are valuable tools for constraining cosmological and astrophysical models (see e.g., Voit 2005; Allen et al. 2011; Weinberg et al. 2013; Kravtsov & Borgani 2012 and references therein). Clusters imprint signals on the sky across the electromagnetic spectrum which have led to three main ways of observationally detecting these systems: as overdensities of galaxies in optical and/or near-infrared surveys (e.g., Abell 1958; Koester et al. 2007; Wen et al. 2012; Rykoff et al. 2014; Bleem et al. 2015a; Eisenhardt et al. 2008; Wen et al. 2018; Oguri et al. 2018; Gonzalez et al. 2019), as sources of extended extragalactic emission at X-ray wavelengths (e.g., Gioia et al. 1990; Böhringer et al. 2004; Piffaretti et al. 2011; Ebeling et al. 2010; Mehrtens et al. 2012; Liu et al. 2015b; Adami et al. 2018; Klein et al. 2019), and via their Sunyaev-Zel'dovich (SZ) signature (Sunyaev & Zel'dovich 1972) in millimeter (mm)-wave surveys. The latter two techniques rely on observables arising from the hot ($10^7 - 10^8$K) gas in the intracluster medium. While wide-field SZ-cluster selection is the newest realized technique—with the first cluster blindly detected in mm-wave survey data in 2008 (Staniszewski et al. 2009)—the field has rapidly advanced with over 1,000 SZ-selected clusters published to date (Bleem et al. 2015b; Planck Collaboration et al. 2016a; Hilton et al. 2018; Huang et al. 2019). SZ-selected cluster samples from high-resolution mm-wave surveys are of particular interest as they have low-scatter mass-observable proxies and, given the redshift-independence of the thermal SZ surface brightness, they are in principle mass-limited (Carlstrom et al. 2002; Motl et al. 2005). Indeed, such samples have enabled SZ-cluster cosmological results that are competitive (Planck Collaboration et al. 2016b; Hasselfield et al. 2013; Bocquet et al. 2019) with samples selected at other wavelengths (e.g., Vikhlinin et al. 2009; Mantz et al. 2010, 2015).

Cosmological constraints from samples of clusters are currently limited by an imperfect knowledge of both cluster selection and the connection of cluster observables to theoretical models. The multi-wavelength na-

ture of cluster signals allows for considerable opportunities to test and improve our understanding of these relations. Such explorations with SZ data and observations at other wavelengths can take many forms including: (a) the use of optical, near-infrared, and X-ray data to both confirm SZ-cluster candidates and to provide empirical tests of models of SZ selection (e.g., Andersson et al. 2011; Planck Collaboration et al. 2012, 2013; Liu et al. 2015a; Bleem et al. 2015b; Planck Collaboration et al. 2016a; Hilton et al. 2018; Burenin et al. 2018; Barrena et al. 2018); (b) using SZ data to probe X-ray samples (e.g., Bender et al. 2016; Czakon et al. 2015; Mantz et al. 2016) and to (c) test mass-optical observable scaling relations (Planck Collaboration et al. 2011; Biesiadzinski et al. 2012; Sehgal et al. 2013; Rozo et al. 2014, 2015; Mantz et al. 2016; Saro et al. 2017; Jimeno et al. 2018). Multi-wavelength observables are also used to constrain relevant quantities such as the spatial distribution of proxies for the cluster centers that feed into the derivation of such relations (e.g., Lin & Mohr 2004; George et al. 2012; Saro et al. 2015; Zhang et al. 2019).

In this work we expand the sample of SZ-selected clusters available for such studies using a new survey conducted using the SPTpol receiver (Austermann et al. 2012) on the South Pole Telescope (SPT). This wide and shallow survey complements the deeper surveys conducted with the SPT (Henning et al. 2018; Benson et al. 2014) and will provide additional overlap for the comparison of cluster properties with the ACTPol (De Bernardis et al. 2016) and *Planck* surveys. Here we present 266 cluster candidates detected at a signal-to-noise $\xi > 5$, 244 of which are confirmed as clusters using optical and near-infrared data as well as via a search of the literature. We also report an additional 204 confirmed systems at $4 < \xi < 5$. Combining this dataset with the previously published SPT-SZ cluster sample (Bleem et al. 2015b, hereafter B15), we use this expanded cluster sample to explore the SZ properties of massive optically selected clusters identified using the red-sequence Matched-Filter Probabilistic Percolation (redMaPPer) algorithm (Rykoff et al. 2014) in the Dark Energy Survey Year 3 dataset.

We organize this work as follows. In Section 2 we describe the survey observations and data reduction process. In Section 3 we describe the identification of cluster candidates including checks on the radio contamination of the sample and in Section 4 the cluster confirmation process including details on the external datasets used for this process. In Section 5 we present the full sample and several internal consistency checks with the SPT-SZ cluster sample. Detailed comparisons to the Dark Energy Survey redMaPPer sample including determination of the SZ-optical center offsets and SZ-mass-to-optical richness relation are presented in Section 6. We conclude in Section 7.

All optical magnitudes are quoted in the AB system (Oke 1974). Except when noted, all masses are reported in terms of M_{500c}, defined as the mass enclosed within a radius at which the average density is 500 times the critical density at the cluster redshift. We assume a fiducial spatially flat ΛCDM cosmology with $\sigma_8 = 0.80$, $\Omega_b = 0.046$, $\Omega_m = 0.30$, $h = 0.70$, $n_s(0.002) = 0.972$, and $\Sigma m_\nu = 0.06$ eV. The normal distribution with mean $\boldsymbol{\mu}$ and variance $\boldsymbol{\Sigma}$ is written as $\mathcal{N}(\boldsymbol{\mu}, \boldsymbol{\Sigma})$. Selected data reported in this work, as well as future updates to the properties of these clusters, will be hosted at http://pole.uchicago.edu/public/data/sptsz-clusters.

2. MILLIMETER-WAVE OBSERVATIONS AND DATA PROCESSING

The SPTpol Extended Cluster Survey (SPT-ECS) is a 2770-square-degree survey that covers two separate regions of sky with low dust emission that lie north of previous areas surveyed using the SPT: a 2200 deg^2 region bounded in right ascension (R.A.) and declination (δ) by $22^h \leq$ R.A.$\leq 6^h$ and $-40° < \delta < -20°$ and a second 570 square degree region bounded by $10^h \leq$ R.A. $\leq 14^h$ and $-30° \leq \delta \leq -20°$. These observations—conducted during the 2013, 2014, and 2015 austral summer months when data from the main 500-square degree SPTpol survey field (centered at R.A=0^h, $\delta = -57.5°$, see Henning et al. 2018) would have been contaminated by scattered sunlight—serve to significantly increase the overlap of data from the SPT with that from other surveys including the Dark Energy Survey (DES; Flaugher et al. 2015), Kilo-Degree Survey (KIDS; de Jong et al. 2013), 2-degree Field Lensing Survey (2dFLenS; Blake et al. 2016), VISTA Kilo-Degree Infrared Galaxy Survey (VIKING, Edge et al. 2013), and *Herschel*-ATLAS (Eales et al. 2010); see Figure 1.

2.1. *Observations*

The survey was conducted using the SPTpol receiver that was installed on the 10 m South Pole Telescope (Carlstrom et al. 2011) from 2012-2016. As detailed in Austermann et al. (2012), the receiver is composed of 768 feedhorn-coupled polarization-sensitive pixels split between the two channels with 588 pixels at 150 GHz and 180 pixels at 95 GHz; each pixel contains two transition-edge-sensor bolometers resulting in 1536 detectors in total. The primary mirror is slightly underilluminated resulting in beams well approximated by Gaussians with full width at half maximum of 1.2 and 1.7 arcmin at 150 and 95 GHz, respectively.

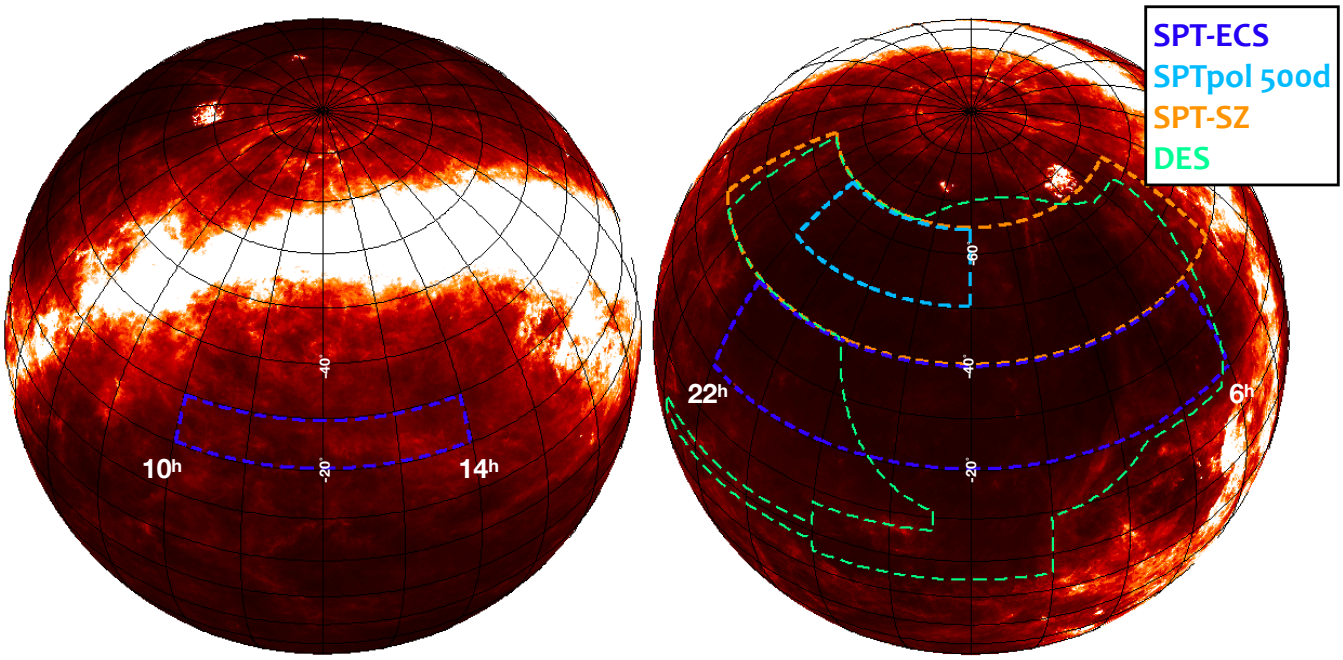

Figure 1. Footprint of the SPTpol Extended Cluster Survey (dark blue) as compared to the SPT-SZ (orange) and SPTpol 500d survey (light blue). Optical-near infrared imaging from the Dark Energy Survey (green-dashed region) covers $\sim 58\%$ of the survey footprint and is used to confirm a significant number of survey clusters presented in this work. The survey outlines are overlaid on the IRAS 100 μm dust map (Schlegel et al. 1998) with the orthographic projection chosen such that the South Celestial Pole is at the top of the globe. Beyond DES, SPT-ECS also has significant overlap with the southern field of the Kilo-Degree Survey, the *Herschel*–ATLAS survey, and the 2dFLenS spectroscopic survey.

The survey is composed of ten separate $\sim 250 - 270$ deg^2 "fields", each imaged to noise levels of $\sim 30 - 40$ μK-arcmin at 150 GHz; see Table 1. The fields were observed by scanning the telescope at fixed elevation back and forth in azimuth at ~ 0.55 degrees/sec, stepping 10 arcmin in elevation, and then scanning in azimuth again. This process is repeated until the full field is covered in a complete "observation". Each field was observed > 80 times and twenty different dithered elevation starting points were used to provide uniform coverage in the final coadded maps.

2.2. *Data Processing*

The data processing and map-making procedures in this work follow closely those in previous SPT-SZ and SPTpol publications (see e.g., Schaffer et al. 2011; Bleem et al. 2015b; Crites et al. 2015; Henning et al. 2018). First, for each observation, the time-ordered bolometer data (TOD) is corrected for electrical cross talk between detectors and a small amount of bandwidth (~ 1.4 Hz and harmonics) is notch filtered to remove spurious signals from the pulse tube coolers that cool the optics and receiver cryostats. Next, using the cut criteria detailed in Crites et al. (2015), detectors with poor noise performance, poor responsivity to optical sources, and/or anomalous jumps in TOD, are removed. As this work is focused on temperature-based science we relax the requirement that both bolometers in a pixel polarization pair be active for an observation. Relative gains across the array are then normalized using a combination of regular observations of both an internal calibrator source and the galactic HII region RCW38. For the first field observed in the survey—ra23hdec−35[1]—the internal calibrator was inadvertently disabled during summer maintenance for $\sim 50\%$ of the observations and so these data were relatively calibrated only with RCW38 observations.

The TOD is then processed on a per-azimuth scan basis by fitting and subtracting a seventh-order Legendre polynomial, applying an isotropic common mode filter that removes the mean of all detectors in a given frequency, high-passing the data at angular multipole $\ell = 300$ and low-passing the data at $\ell = 20,000$. Sources detected in preliminary map making runs at $\geq 5\sigma$ ($\sim 9 - 15$ mJy depending on field depth) at 150 GHz as well as bright radio sources detected in the Australia Telescope 20-GHz Survey (AT20G; Murphy

[1] SPT fields are named for their central coordinates.

et al. 2010) at the edges of the field are masked with a 4′ radius during these filtering steps. The SPT-ECS also contains a small number of sources with extended mm-wave emission (see Section 3.2) and more conservative masks around these sources are applied in the filtering steps.[2] Following filtering, the TOD for each detector is then weighted based on the inverse noise-variance in the 1-3 Hz signal band and binned into 0.′25 pixels in maps in the Sanson-Flamsteed projection (Calabretta & Greisen 2002) using reconstructed telescope pointing. We have extended the characterization of the SPT pointing model to incorporate position information from all mm-wave-bright AT20G sources (typically 45-60 sources/field detected at S/N > 10 were used compared to the 2-3 bright sources that proved sufficient in previous SPT analyses) to better constrain boom flexure and other mechanical aspects of the telescope at the elevations of these fields. With this extension we achieve reconstructed pointing performance of $\sim 3-4''$ root-mean-squared (rms) when comparing SPT source locations to AT20G positions.

The single observation maps for each field are then characterized based on both noise properties and coverage; maps with significant outliers from the median of these distributions are flagged and excluded from the coaddition step. The remaining maps are combined in a weighted sum based on their total pixel weights from the previous binning step; final maps consist of 78-150 observations per field.

The SPT-ECS fields were taken at significantly higher levels of atmospheric loading compared to other SPTpol survey data.[3] We found it necessary to augment our standard absolute calibration process (see e.g., Staniszewski et al. 2009) with two additional steps that make use of the 143 GHz full and half-mission temperature maps from the 2015 *Planck* data release (Planck Collaboration et al. 2015, 2016c). The first step follows a similar method as the absolute temperature calibration conducted in previous SPT power spectrum analyses (e.g, Hou et al. 2018; Henning et al. 2018). We derive normalization factors to rescale each coadded map by first convolving the *Planck* maps with the SPT beams and transfer functions (the latter resulting from the TOD filtering process described above) and the SPT maps with the *Planck* beam and window function. Then, masking bright point sources in the field, we set the normalization as the ratio from $900 \leq \ell \leq 1600$ of the cross spectrum of the *Planck* half mission maps to the cross spectrum of the *Planck* full mission map with the SPT maps. The 95 GHz data required an additional calibration step as we found—especially in the fields centered at $\delta = -25°$—that the responsivity of the detectors decreased with increasing airmass. This trend is well represented as a linear decline in sensitivity as a function of declination and we used the *Planck* data to fit for and correct this variation across the fields.

[2] Given the arcminute scale beam, essentially all extragalactic sources at $z > 0.05$ are unresolved in SPT data. See e.g., discussion of such sources in the SPT-SZ survey in W. Everett et al. (2019, in preparation).

[3] From 1.5–3 airmasses as compared to the median airmass of ~ 1.2 for the SPTpol main survey field.

3. CLUSTER IDENTIFICATION

Identification of cluster candidates in the SPT-ECS proceeds in essentially identical fashion to previous SPT analyses (see, e.g., B15 for a recent example). This section provides an overview of the process; readers are referred to previous publications for more details.

3.1. *Sky Model and Matched Filter*

The thermal SZ signal is produced by the inverse Compton scattering of CMB photons off high-energy electrons, such as those that reside in the intracluster medium of galaxy clusters. This produces a spectral distortion of the observed CMB temperature at the location $\mathbf{x}$ of clusters given by the line-of-sight integral (Sunyaev & Zel'dovich 1972):

$$\begin{aligned}\Delta T(\mathbf{x},\nu) &= T_{\rm CMB}\ f_{\rm SZ}(\nu) \int n_{\rm e}(\mathbf{r}) \frac{k_{\rm B} T_{\rm e}(\mathbf{r})}{m_{\rm e}c^2} \sigma_{\rm T} dl \\ &\equiv T_{\rm CMB}\ f_{\rm SZ}(\nu)\ y_{\rm SZ}(\mathbf{x})\end{aligned} \quad (1)$$

where $T_{\rm CMB} = 2.7260 \pm 0.0013$ K is the mean CMB temperature (Fixsen 2009), $f_{\rm SZ}(\nu)$ is the frequency (ν) dependence of the thermal SZ effect (Sunyaev & Zel'dovich 1980), $n_{\rm e}$ the electron density, $T_{\rm e}$ the electron temperature, $k_{\rm B}$ the Boltzmann constant, $m_{\rm e}c^2$ the electron rest mass energy, $\sigma_{\rm T}$ the Thomson cross-section, and $y_{\rm SZ}$ is the Compton y-parameter. This effect results in a decrement at the two channels measured by the SPTpol receiver; for a non-relativistic thermal SZ spectrum the effective band centers are 95.9 and 148.5 GHz.[4]

To identify candidate galaxy clusters we use a spatial-spectral filter designed to optimally extract thermal SZ cluster signals (Melin et al. 2006). This "matched-filter" approach has been widely used in both previous SPT publications as well as in analyses by other experiments (see e.g., Planck Collaboration et al. 2016a; Hilton et al.

[4] Though see e.g., Wright (1979); Nozawa et al. (2000); Itoh & Nozawa (2004); Chluba et al. (2012) for discussion of relativistic corrections which become relevant at $T_{\rm e} \gtrsim 8$ keV.

Table 1. Summary information for the 10 fields that comprise the 2770-square-degree SPTpol Extended Cluster Survey.

Name	R.A. (°)	δ (°)	Area (deg^2)	σ_{95} (μK-arcmin)	σ_{150} (μK-arcmin)	$\gamma_{\rm field}$
RA23HDEC-25	345.0	-25.0	276.0	61.3	30.5	0.84
RA23HDEC-35	345.0	-35.0	250.2	59.4	36.6	0.80
RA1HDEC-25	15.0	-25.0	275.2	80.4	39.2	0.69
RA1HDEC-35	15.0	-35.0	251.8	61.5	36.6	0.79
RA3HDEC-25	45.0	-25.0	272.9	54.6	28.6	0.90
RA3HDEC-35	45.0	-35.0	248.8	43.8	25.3	1.04
RA5HDEC-25	75.0	-25.0	277.0	57.0	31.4	0.85
RA5HDEC-35	75.0	-35.0	250.3	54.8	31.6	0.88
RA11HDEC-25	165.0	-25.0	274.3	77.6	40.0	0.68
RA13HDEC-25	195.0	-25.0	270.8	50.7	30.0	0.90

Note—Listed are the field name, center, source-masked effective area, and noise levels at both 95 and 150 GHz, as well as the "field-renormalization" factors discussed in Section 5.1.1. The survey contains an additional 122 square degrees that are masked in the cluster analysis owing to the presence of mm bright sources. Following Schaffer et al. (2011), the noise levels are measured from $4000 < \ell < 5000$ using a Gaussian beam approximation with full-width at half maximum (FWHM) of 1.7 (1.2) arcmin at 95 (150) GHz respectively. The field renormalization factors are normalized with respect to the values from Reichardt et al. (2013) and de Haan et al. (2016) for the SPT-SZ survey.

2018). We model the cluster profile as a projected spherical β-model with β fixed to 1 (Cavaliere & Fusco-Femiano 1976):

$$\Delta T = \Delta T_0 (1 + \theta^2/\theta_{\rm c}^2)^{-(3\beta-1)/2} \quad (2)$$

where the normalization ΔT_0 is a free parameter and the core radius, $\theta_{\rm c}$, is allowed to vary in twelve equally spaced steps from $0.'25$ to $3'$.

3.2. *Masking*

To prevent spurious decrements from the filtering process we mask regions around bright emissive sources before applying the matched filters to the maps. These sources are detected in the 150 GHz data using a matched filter designed to optimize the signal-to-noise of point sources. Masks of $4'$ radius are placed over sources detected at $> 5\sigma$ and candidates detected within $8'$ of these sources are excluded from the final cluster lists. Additionally, as referenced above in Section 2.2, there are three extended sources in these fields—NGC 55, 253, and 7293 (Dreyer 1888) and one exceptionally bright quasar—QSO B0521-365 (e.g., Planck Collaboration et al. 2018)—that require additional masking. Masks of radius 0.33° are used for the NGC sources and radius 0.25° for the quasar. Regions around these sources are also inspected following the cluster filtering process and a small number of spurious candidates are rejected. In total 122 deg^2 are masked, 4.5% of the full survey area.

3.3. *Candidate Identification*

Cluster candidates are identified as peaks in the matched-filtered maps. For each location we define our SZ observable, ξ, as the maximum detection-significance over the twelve filter scales. As in prior SPT analyses, there is a small declination dependence in the noise owing to atmospheric loading, detector responsivity, and coverage changes across each field. To capture this in the ξ estimates, each filtered map is split into $90'$ strips in declination and—as in Huang et al. (2019)—noise in each strip is measured by measuring the standard deviation of a Gaussian fit to unmasked pixels. In this work, all candidates $\xi \geq 5$ are reported, and for $4 < \xi < 5$, where our followup is currently highly spatially incomplete, we also report confirmed systems in the DES common region (see Section 4).

3.4. *Field Depth Scaling and False Detection Rate*

We make use of simulations to estimate the contamination of our catalogs by spurious detections and to renormalize the measured SZ detection significances to account for the varying field depths (see Section 5.1.1). Simulations were previously used to this effect in e.g., Reichardt et al. (2013), de Haan et al. (2016), Huang et al. (2019); we briefly overview the process here and

describe some small changes to the process from the SPT-SZ simulations. For more details on these simulations see Huang et al. (2019).

For each field we construct sets of simulated mm-wave skies consisting of:

- primary lensed CMB (Keisler et al. 2011).
- signals from Poisson and clustered dusty sources that we approximate as Gaussian random fields with amplitude and spectral indices matching George et al. (2015).
- discrete radio sources below the masking threshold with the source population drawn from the model of De Zotti et al. (2005) with spectral indices drawn from the results of George et al. (2015) and Mocanu et al. (2013).
- thermal SZ constructed using a halo light cone from the Outer Rim (Habib et al. 2016; Heitmann et al. 2019) simulation with thermal SZ profiles painted for each halo with $M_{200c} > 10^{13}$ following the methodology of Flender et al. (2016) and using the pressure profiles of Battaglia et al. (2012). The thermal SZ power is consistent with the results of George et al. (2015). The SZ signal is omitted in the false detection simulations.
- atmospheric and instrumental noise from jackknife noise maps constructed via coadding field observations where half of the observations were randomly multiplied by -1.

Each sky realization is convolved with the SPT beam and transfer function. As in Huang et al. (2019), there are two significant changes compared to simulations used for SPT-SZ cluster studies. First, we use discrete radio sources, as opposed to Gaussian random fields, to account for radio contamination. This change was found to be important for properly capturing the false detection rates of the deeper SPTpol 100d and 500d cluster surveys but has negligible impact at the noise levels of the SPT-ECS and SPT-SZ surveys. We adopt it for consistency here. Second, we use the measured SPT beams, as opposed to Gaussian approximations, which enables more consistent scalings between the SPT-SZ and SPTpol experiments.

To estimate the number of spurious detections in each field, we run the cluster detection algorithm on the simulated SZ-free maps. As in de Haan et al. (2016), to reduce shot noise in our estimates from our finite number of simulations, we model the false detection rate with the function:

$$N_{\rm false}(>\xi) = \alpha_{\rm field} e^{-\beta_{\rm field}(\xi-5)} \times \text{field area} \quad (3)$$

All of the fields are well approximated by $\alpha \sim 0.008$ and $\beta = 4.3$; as each field is approximately 260 square degrees this results in ~ 2 false detections/field expected above $\xi = 5$ and $17 - 18$ above $\xi = 4.5$.

As detailed in de Haan et al. (2016), the field depth rescaling factors, which track changes in "unbiased significance" as a function of mass for the varying field depths, are determined by measuring the signal-to-noise of simulated clusters at their known locations and optimal filter scales from the simulated maps (see also 5.1.1). We list the field depth rescaling factors $\gamma_{\rm field}$ in Table 1. Following previous SPT publications, the absolute normalization is set to correspond to the unit scaling adopted in Reichardt et al. (2013). While in principle the field scaling simulations should be sufficient to properly scale the SPT-ECS field depths relative to SPT-SZ, the extra calibration steps required for the SPT-ECS survey make this challenging. To capture any residual uncertainty in this process we introduce a new parameter, $\gamma_{\rm ECS}$, which rescales all field scalings in the SPT-ECS survey $\gamma_{{\rm SPT-ECS},i} = \gamma_{\rm ECS} \times \gamma_{{\rm field},i}$. With this parametrization, $\gamma_{\rm ECS} = 1$ means that our simulations capture the entirety of the relative difference in effective depth between SPT-SZ and SPT-ECS. We empirically calibrate $\gamma_{\rm ECS}$ in sections 5.1.2 and 6.1.

3.5. *Potential Contamination of the SZ Sample From Cluster Member Emission*

Galaxy clusters contain an overdensity of galaxies relative to the field, and galaxies emit radiation at mm wavelengths. Since the thermal SZ signal from the cluster gas is a decrement in the frequency bands used in this work, any positive emission above the background will act as a negative bias to the SZ signature. We can classify the potential bias from cluster galaxy emission into two regimes, one in which the integrated emission from many cluster members produces an average bias to all clusters in a given mass and redshift range, with little variation from cluster to cluster; and one in which a single bright galaxy (or a very small number of bright galaxies) imparts a significant bias to a random subsample of clusters. We can also separate the contributions to this effect from the two primary classes of mm-wave-emissive sources: active galactic nuclei producing synchrotron emission ("radio sources") and star-forming galaxies producing thermal dust emission ("dusty sources").

The contribution to the second type of bias from dusty sources is expected to be negligible, because the dusty source population falls off steeply at high flux (e.g., Mocanu et al. 2013), so that the areal density of dusty sources bright enough to fill in a cluster decrement at

a level important for this work is very low. This statement is for the field galaxy population, so if galaxies in clusters were more likely than field galaxies to be dusty and star-forming, the bright population could still be an issue. In fact, the opposite is expected to be true; i.e., compared to the field population, galaxies in clusters are less likely to be dusty and star-forming, at least at $z < 1$ (e.g., Bai et al. 2007; Brodwin et al. 2013; Alberts et al. 2016). In Vanderlinde et al. (2010), it was argued that the other regime of bias from dusty sources is also negligible for clusters more massive than $\sim 2\times10^{14} M_{\odot}$, which includes all the clusters in this sample (see also, e.g., Soergel et al. 2017 for an analysis of a sample of low-z optically selected clusters, and Erler et al. 2018, Melin et al. 2018 for explorations of the *Planck* sample).

To assess the potential contamination from radio sources, we make use of the publicly available maps from the 1.4 GHz National Radio Astronomy Observatory (NRAO) Very Large Array (VLA) Sky Survey (NVSS, Condon et al. 1998).[5] NVSS covers the full sky north of declination $-40°$ and thus has nearly 100% overlap with the survey fields in this work. The data for the NVSS were taken between 1993 and 1997, so source variability will limit the fidelity of the estimate of contamination to any individual cluster, but we can make some statements about the average or median contamination across the catalog and the fraction of clusters expected to be strongly affected by radio source contamination.

For each of our survey fields, we download all NVSS postage-stamp maps (each 4×4 degrees) that have any overlap with that field and reproject them onto the same pixel grid as used in our cluster analysis. We then make beam- and transfer-function-matched NVSS maps for each of the SPTpol observing frequencies by convolving the NVSS maps with a kernel defined by the Fourier-space ratio of the SPTpol beam and transfer function at that frequency and the effective NVSS beam (a 45-arcsec FWHM Gaussian). We scale the intensity in these maps from 1.4 GHz to SPTpol frequencies assuming a spectral index of -0.7 (roughly the mean value found for radio sources in clusters by Coble et al. 2003), and we convert the result to CMB fluctuation temperature.

We then combine the SPTpol-matched NVSS maps in our two bands using the same band weights as used in the cluster-finding process (Section 3) and filter the output with the same β-model-matched filters as used in the cluster-finding process. For each cluster candidate in the catalog, we take the combined NVSS map filtered with the same β-model profile as the cluster candidate, and we record the value of the combined, filtered NVSS map at the candidate location. We divide that value by the same noise value used in the denominator of the ξ value for the cluster candidate, and we record that value as our best estimate of the contamination to the ξ value of that cluster candidate from radio sources. Since the NVSS maps contain all the radio flux at 1.4 GHz (not just the sources bright enough to be included in the NVSS catalog), this test accounts for both regimes of bias discussed above.

The median contamination calculated in this way is $\Delta\xi_{\rm med} = -0.05$, or 1% of the threshold value for inclusion in the catalog of $\xi = 5$. Of the 266 candidates in the catalog, 13 ($\sim$5%) have a predicted contamination of greater than 10% of their measured SZ flux, and 7 ($\sim$2.6%) have a predicted contamination of greater than 20%. One cluster candidate, SPT-CL J2357-3446, has an anomalously large predicted bias of $\Delta\xi = -11.1$. This candidate is almost certainly the low-redshift ($z = 0.048$) cluster Abell 3068 (separation $0\farcm1$), and it is within $0\farcm6$ of the NVSS source NVSS J235700-344531, which has a catalog 1.4 GHz flux of 1.28 Jy. This NVSS source is a cross-identifcation of PKS 2354-35, which lies at a redshift consistent with being a member of A3068 ($z = 0.049$) and is identified as the central galaxy of this cluster by many authors (e.g., Schwartz et al. 1991). Given the relative redshift dependence of the thermal SZ signature of clusters and the flux density of member emission, it is not surprising that the highest level of radio source contamination occurs in one of the lowest-redshift clusters in the sample. It is somewhat surprising, though, that a cluster with a predicted radio source contamination of $\Delta\xi > 10$ would be detected at $\xi = 5.5$, as this one is in our catalog. The apparent answer to this puzzle is source variability. More recent observations of this source with the Australia Compact Telescope Array (ATCA) at 5 GHz (Burgess & Hunstead 2006) resulted in a measured flux density of 99 mJy, which would imply a spectral index of < -2.0 if naively combined with the NVSS measurement at 1.4 GHz. We conclude that during our observations, the 150 GHz flux of this source was likely < 10 mJy (as implied by the ATCA measurement and a spectral index of -0.7) rather than the $\sim$50 mJy implied by the NVSS measurement. Finally, we also note that all previous SPT cluster cosmology results have cut clusters below $z = 0.3$ or 0.25, so this cluster would not normally be included in an SPT cosmology analysis.

These contamination numbers will be diluted somewhat by any false detections. However, removing the 22 unconfirmed candidates at $\xi > 5$ has negligible effect. If

[5] Maps downloaded via anonymous ftp from https://www.cv.nrao.edu/nvss/postage.shtml

we extend the sample to all confirmed systems at $\xi > 4$ (for a total of 448 clusters), we find a similar median contamination ($\Delta\xi_{\rm med} = -0.050$) and fraction of systems above a given level of contamination: 17 ($\sim$4%) and 8 ($\sim$2%) above 10% and 20% contamination, respectively. We flag candidates with $> 10\%$ potential contamination of their measured SZ signal in Tables 8 and 9.

3.6. *Clusters in Masked Regions*

In addition to the potential bias to our sample from the mm-wave emission from cluster members, there is a potential bias from the avoidance of mm-wave-bright sources in our cluster-finding. As discussed in Section 3.2, we discard any cluster detection within $8'$ of a source detected at 5σ ($\sim$9-15 mJy, field-dependent) at 150 GHz. If there were a strong physical association between galaxy clusters and such sources, our measured cluster abundance would be biased low.

The majority of sources with 150 GHz flux density above 9 mJy are flat-spectrum quasars (see e.g., Mocanu et al. 2013; Gralla et al. 2019), and, based on studies of radio galaxies from lower frequency surveys (e.g., Lin et al. 2009; Gralla et al. 2011, 2014; Gupta et al. 2017), there is not expected to be a significant SZ selection bias from these sources. However, we can perform several checks on the effects of masking with the data in hand. First, as in B15, we perform a secondary cluster search, this time only masking emissive sources detected at $>$ 100 mJy at 150 GHz. Each candidate from this run was visually inspected and, as expected, this candidate list was dominated by filtering artifacts; no new clusters were identified in this secondary run.

We also check for any statistical association between the flux-limited DES redMaPPer optically selected cluster catalog and associated random locations (discussed in more detail below in Section 4.1.1 and in Rykoff et al. 2016) and SPT-selected emissive sources. To increase the sensitivity of this test, we also include sources from the SPT-SZ survey, which had a 5σ source threshold of lower flux ($\sim$6 mJy; W. Everett et al., (2019, in preparation)). We first measure the probability of optical clusters and random locations to be within the $8'$ source masks and find marginal differences between the two. Adopting a $3'$ radius to reduce the noise from chance associations and further restricting the cluster sample to $z > 0.25$ where we expect the SPT selection to be well understood, we find an excess probability over random of $\lesssim 1\%$ for clusters to fall in the source-masked regions (see Table 2). While the purity of the flux-limited sample is expected to decrease at high redshift (thus limiting our ability to test for trends with redshift), we note that we find no significant difference in the fraction of clusters in masked regions between the full sample and two subsamples constructed by splitting the optical sample at its median redshift of $z = 0.755$.

Table 2. Optical Clusters near mm-wave bright sources

λ range	$N_{\rm clusters}$	% in masked region	$N_{\rm clusters}^{\rm SPT\text{-}SZ}$	%
randoms	2.1e6	0.9	1.2e6	1.05
20−30	2.3e4	1.11	1.3e4	1.4
30−50	9.3e3	0.95	5.4e3	1.1
50−80	1.9e3	1.22	1.1e3	1.65
> 80	3.5e2	1.13	2.0e2	1.5

NOTE—Percentage of DES redMaPPer clusters at $z > 0.25$ that fall within $3'$ of bright emissive sources; $N_{\rm clusters}$ corresponds to the total number of clusters in a given richness bin within the SPT-SZ+SPT-ECS (Left) or SPT-SZ only (Right) footprint. The top row provides statistics for random sources. Less than 1% of clusters over random fall in the masked areas.

4. EXTERNAL DATASETS AND CLUSTER CONFIRMATION

To confirm the SZ candidates as galaxy clusters we make use of targeted optical and near-infrared follow-up observations, data drawn from the wide area Dark Energy Survey (Flaugher et al. 2015), the Pan-STARRS1 survey (Chambers et al. 2016), the all sky Wide-field Infrared Survey Explorer (WISE) dataset (Wright et al. 2010), and the literature. In this section we describe each dataset and how it is used to confirm and/or characterize the SZ-selected clusters. Overall, we focus our targeted follow-up efforts on ensuring nearly complete imaging of high-significance ($\xi > 5$) cluster candidates to depths sufficient to confirm clusters to $z \sim 0.8 - 1.0$. For lower-significance targets we rely significantly more on the availability of wide-area imaging datasets.

4.1. *External Datasets*

4.1.1. *The Dark Energy Survey and redMaPPer*

The Dark Energy Survey is a recently completed ~ 5000 deg^2 optical-to-near-infrared imaging survey conducted with the DECam imager (Flaugher et al. 2015) on the 4m Blanco Telescope at Cerro Tololo Inter-American Observatory. The survey was designed to have significant overlap with the original SPT-SZ survey (see Figure 1) and we have increased this overlap with the addition of SPT-ECS. In this work we make use of the DES data acquired in years 1-3 of the survey; this data reaches signal-to-noise 10 in $1.''95$ apertures in the *grizY* bands at [24.33, 24.08, 23.44, 22.69, 21.44] magnitudes with resolution—given by the median FWHM of the

point spread functions—of [1.12, 0.96, 0.88, 0.84, 0.9] arcseconds respectively (Abbott et al. 2018)[6].

We make particular use of the redMaPPer optically selected galaxy cluster sample drawn from the DES data. As its name implies, redMaPPer (hereafter RM) is a red-sequence-based cluster finder that identifies clusters as overdensities of red galaxies based upon galaxy positions, colors, and brightness (Rykoff et al. 2014, 2016). Each RM cluster detection provides—amongst other quantities—a cluster redshift, a probabilistic center (based on the consistency of bright cluster members with the observed properties of cluster central galaxies), a similarly probabilistic cluster member catalog, and a total optical richness, λ, that is the sum of all the cluster member probabilities corrected for various masking and completeness effects. The RM sample has been shown to have excellent redshift precision, with uncertainties in redshift estimates of $\sigma_z/(1+z) \sim 0.01$ for clusters $z < 0.9$.

There are 2 different RM catalogs: a "flux-limited" sample that includes significant numbers of high-redshift clusters for which the optical richness estimates must be extrapolated and a "volume-limited" sample for which the DES data is sufficiently uniform and deep that the richnesses can be well measured; DES cluster cosmology constraints are derived using the volume-limited sample (Rykoff et al. 2016; McClintock et al. 2019). In this work, we explore characteristics of the joint SPT-RM cluster sample using the volume-limited catalog.[7] In total there are 53,610 (21,092) RM clusters at $\lambda > 20$ in the full (volume-limited) DES sample, with $\sim 36,000$ ($\sim 16,000$) and $\sim 14,000$ ($\sim 6,000$) of these clusters within the total SPT and SPT-ECS survey area, respectively.

4.1.2. *The Parallel Imager for Southern Cosmology Observations*

We use the Parallel Imager for Southern Cosmology Observations (PISCO; Stalder et al. 2014)—a new imager with a 9′ field-of-view installed on the 6.5 m Magellan/Clay telescope at Las Campanas Observatory in Chile—to obtain approximately uniform depth *griz'* imaging data for over 500 SPT-selected clusters and cluster candidates, including 173 candidates at $\xi \geq 4.5$ in SPT-ECS. These data were obtained as part of an ongoing effort to characterize the strong lensing and bright galaxy populations of the SPT cluster sample.

To analyze the PISCO data, we have constructed a reduction pipeline that includes standard corrections (i.e., overscan, debiasing, flat-fielding, illumination, though we note defringing is not required) as well as specialized routines that correct the data for non-linearities and artifacts caused by bright stars. After the images have been flatfielded, we use the PHOTPIPE pipeline (Rest et al. 2005; Garg et al. 2007; Miknaitis et al. 2007) for both astrometric and relative calibration prior to coaddition. We make use of stars from the DES DR1 public release (Dark Energy Survey Collaboration et al. 2018), from the second *Gaia* data release (Gaia Collaboration et al. 2018), or from the Pan-STARRS 1 release (Flewelling et al. 2016) to obtain sufficient numbers of sources for good astrometric solutions. Images are coadded using SWarp (Bertin et al. 2002) and sources are detected in the coadded images using SExtractor (Bertin & Arnouts 1996) in dual-image mode with the $r-$band image set as the detection image. We find the typical $\sim 85\%$ completeness depth of these images to be $r = 24.3$. We separate bright stars and galaxies using the *SG* statistic (Bleem et al. 2015a) and use these stars to calibrate the photometry with stellar locus regression (High et al. 2009); absolute magnitudes are set using the 2MASS point source catalog (Skrutskie et al. 2006).

4.1.3. *Spitzer/IRAC and Magellan/Fourstar*

Based on initial PISCO imaging, we were able to identify a small number of high-redshift cluster candidates worthy of additional follow-up observations. Two systems were imaged as part of a *Spitzer* Cycle 11 program and 5 additional SPT-ECS cluster candidates were part of a Cycle 14 program (ID: 11096,14096; PI:Bleem)[8]. The Cycle 11 (14) candidates were observed with *Spitzer*/IRAC (Fazio et al. 2004) for 360 (180) s on source time integration time in both the 3.6 and 4.5 μm bands. These data were reduced as in Ashby et al. (2009), and are of sufficient depth for cluster confirmation to $z \sim 1.5$.

We have additionally obtained ground-based near-infrared $J-$band imaging for 19 candidates with the Fourstar imager (Persson et al. 2013) installed on the Magellan/Baade telescope. For each candidate, a large number of short exposures were taken using predefined dither macros provided in the instrument control software with the candidate centered on one of the four Fourstar detectors. These images were flatfielded using IRAF routines (Tody 1993), astrometrically registered and relatively calibrated, and coadded using the PHOTPIPE pipeline. Coaddition was performed with `SWarp` and source identification with `SExtractor`. Absolute calibration is tied to the J-band flux from stars in the

[6] Data available: https://des.ncsa.illinois.edu/releases/dr1

[7] RM catalog version 6.4.22

[8] Data available: https://sha.ipac.caltech.edu/applications/Spitzer/SHA/

2MASS point source catalog. While conditions varied between the Fourstar observations these data are typically sufficient to confirm clusters to $z \sim 1.2$ or better.

4.1.4. *Pan-STARRS1*

The SPT fields north of $\delta = -30°$ have been imaged by the Panoramic Survey Telescope and Rapid Response System (Pan-STARRS) in the $grizy_p$ filter bands as part of the Pan-STARRS 3π Steradian Survey (Chambers et al. 2016). In this work we make use of the first data release (Flewelling et al. 2016) available for download from the Mikulski Archive for Space Telescopes.[9] This data release contains images and source catalogs from the "stack" coadded image products. These data are shallower than both the DES survey data and our targeted follow-up imaging, with 5σ point source depths of [23.3, 23.2, 23.1, 22.3, 21.4] magnitudes in the $grizy_p$ bands respectively. Exploring the properties of clusters in the Pan-STARRS footprint that we confirmed in DES, PISCO, and the literature (see below), we find the Pan-STARRS data typically enables robust confirmation of clusters to $z < 0.6 - 0.7$.

4.1.5. *WISE*

As demonstrated in e.g., Gonzalez et al. (2019), observations from the Wide-field Infrared Survey Explorer (WISE; Wright et al. 2010) are an excellent resource for identifying high-redshift clusters. Of particular relevance for this work are the observations in the [W1] and [W2] filter bands at 3.4μm and 4.6μm which we use to confirm cluster candidates by identifying overdensities of high-redshift galaxies at a common 1.6 μm rest frame (see e.g., Muzzin et al. 2013). Here we make use of "unWISE" a new processing of WISE and NEOWISE (Mainzer et al. 2014) data that reaches 3 times the depth of the AllWISE data (Meisner et al. 2017; Schlafly et al. 2019)[10].

4.1.6. *Literature Search*

We additionally search the literature for known clusters in the vicinity of the SZ-selected candidates. Using the SIMBAD[11] database we search for systems within a 5′ radius of the candidate locations. When such a system is found we consider it to be a match if it is at $z < 0.3$; we reduce the matching radius to 2′ for clusters at higher redshifts (except for systems in the *Planck* catalog, see Section 5.3 below). When available, we adopt reported spectroscopic redshifts as the SPT cluster redshifts for previously identified systems. We also make use of reported photometric redshifts for a small number of systems not in DES, Pan-STARRS1, or directly targeted in our follow-up imaging. When possible we use the other external datasets to identify spurious associations with previously reported systems, finding several in this distance-based match.

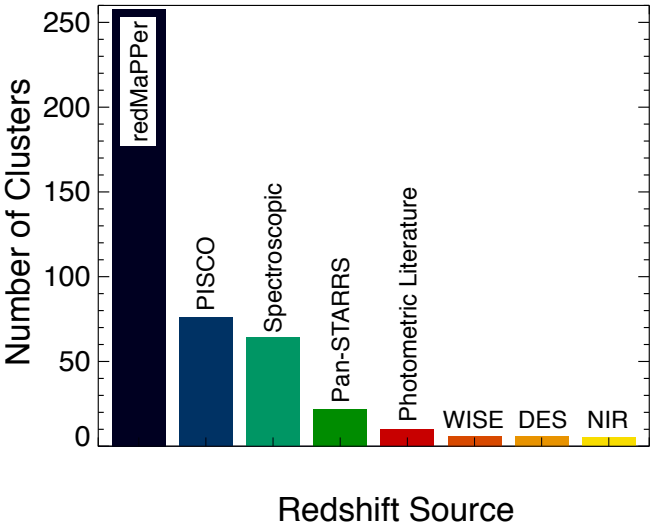

Figure 2. Distribution of the telescope/surveys used to confirm and provide redshifts for the SPT clusters presented in this catalog. While some clusters may have redshifts from multiple sources (for example there is significant overlap between PISCO and RM), we only represent each cluster once in this figure, highlighting the sources of the redshifts reported in Tables 8 and 9. The DES column corresponds to clusters with redshifts from DES data but not from RM (see Section 4.2.2). Generally, data from Pan-STARRS is deep enough to confirm clusters to $z \sim 0.6$, DES and PISCO to $z \sim 0.8 - 1.0$, FourStar to $z \sim 1.2$ and *Spitzer* to $z \sim 1.5$.

4.2. *Cluster Confirmation*

We adopt two different techniques for confirming candidates in clusters: a probabilistic matching to RM clusters in the common overlap region and, for candidates outside the volume probed by RM clusterfinding on DES data, the identification of significant over-densities of red sequence or 1.6 μm rest-frame galaxies at the locations of cluster candidates using the techniques described in B15. We show the distribution of the origins of SPT-ECS cluster redshifts in Figure 2.

4.2.1. *Confirmation with redMaPPer in Scanning Mode*

The RM catalog makes strict cuts on sky coverage and photometric depth to ensure a well-understood optical selection function. In the case of matching to an SZ-selected sample we can somewhat relax these criteria

[9] http://panstarrs.stsci.edu/

[10] Data available: http://unwise.me/imgsearch/

[11] http://simbad.u-strasbg.fr/simbad

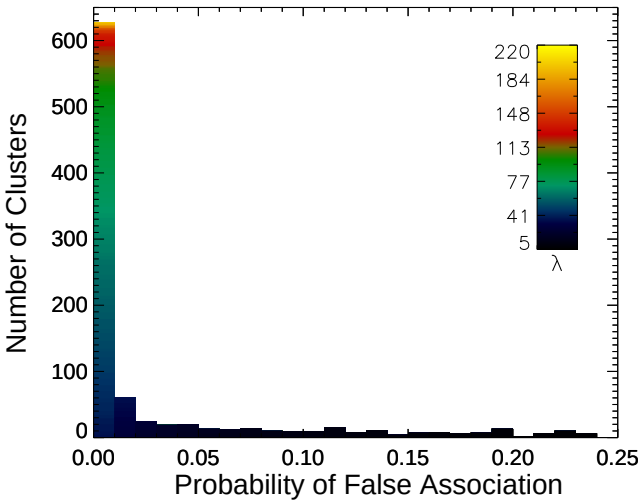

Figure 3. Distribution of probabilities of false association between redMaPPer targeted confirmations and SPT clusters from the SPT-ECS and SPT-SZ surveys. The color scaling represents the optical richnesses of the RM detections centered on SPT locations. For the purposes of this work we reject associations with probabilities of false association greater than 5%.

to also enable targeted searches for red-sequence galaxy counterparts in regions excluded by these cuts. We have run the RM algorithm in "scanning mode" centered on the SPT location where the likelihood of a red-sequence overdensity in apertures of 500 kpc radius is computed as a function of redshift from z=0.1 to 0.95 in steps of $\delta_z = 0.005$. At each redshift the optical richness is computed at both the SZ location and the most likely optical center; for systems with significant red-sequence overdensities the richness and redshift is refined at the highest likelihood redshift using the standard RM radius/richness scaling. Richnesses are recorded for each location where $\lambda \geq 5$. We repeat this scanning procedure for 100 mock SZ samples (at over 100,000 sky locations) to compute the probability over random of finding a cluster of richness λ at an SZ location. We report as "confirmed" clusters for which the probability of random association is less than 5%, which corresponds to $\lambda > 19.3$. As this probability distribution is a continuum (with no clear breaks) this choice is somewhat arbitrary; setting this threshold at 0.05 leads to an expectation of < 2 false associations in the RM-confirmed sample. In Figure 3 we plot the distribution of matched clusters against the probability of random associations for SPT-SZ ($\xi > 4.5$) and SPT-ECS clusters ($\xi > 4$).

For cluster candidates in the common region not confirmed via the RM scanning-mode process we make use of both DES and WISE imaging and photometric catalogs at the cluster locations and, where available, pointed follow-up imaging as described in the next subsection. The confirmation of these clusters follows a similar process to that described below.

4.2.2. *Cluster confirmation from other imaging datasets*

Here we describe the techniques used for confirming cluster candidates not confirmed via the RM algorithm or literature search. We obtained imaging for ~ 100 candidates outside of the volume searched by RM as well as some imaging redundant to the DES imaging (in terms of confirmation) as part of our strong lensing search program that we use here for redshift comparisons. In total, 173 candidates were imaged with Magellan/PISCO (about 2/3 in common with RM, see Figure Figure 4), 19 with Magellan/Fourstar, and 7 with Spitzer (note the NIR imaging overlaps areas with optical imaging). 10 candidates are located in the DES footprint but are either at high redshift or are missing photometry in filters required for RM, and 22 candidates only fall in the Pan-STARRS footprint.

To conduct our targeted search for red-sequence galaxies in these areas, we first calibrate our synthetic model for the colors and magnitudes of red-sequence galaxies, generated with the `GALAXEV` package (Bruzual & Charlot 2003) by assuming a passively evolving stellar population with single formation burst at $z = 3$, to match the relevant survey photometry using samples of known clusters with spectroscopic redshifts. For PISCO, the dataset that we most use to confirm clusters outside of DES, we use 58 SPT-SZ galaxy clusters with spectroscopic redshifts that were imaged as part of our broader SPT characterization program. In Figure 4 we plot in red the measured PISCO redshifts versus those from the training sample as well as additional SPT-ECS clusters with spectroscopic redshifts reported in the literature. The typical redshift precision is $\sigma_z/(1+z) \sim 0.015$ with uncertainties increasing towards higher redshifts. We also plot in black the PISCO redshifts compared to those from the DES RM catalog for 318 systems in SPT-SZ and SPT-ECS and find generally good agreement between the two, though the comparison suggests that the redshifts estimated from PISCO may tend be underestimated at the highest redshifts. More spectroscopic data on high-redshift clusters from ongoing SPT programs will help further validate/improve the PISCO redshift calibration for such systems. Given the excellent redshift precision of the RM algorithm, we adopt RM scanning-mode redshifts by default when clusters are confirmed by both methods. We repeat a similar process with DES photometry, finding $\sigma_z/(1+z) \sim 0.015$, and with 35 spectroscopic clusters (as identified in the

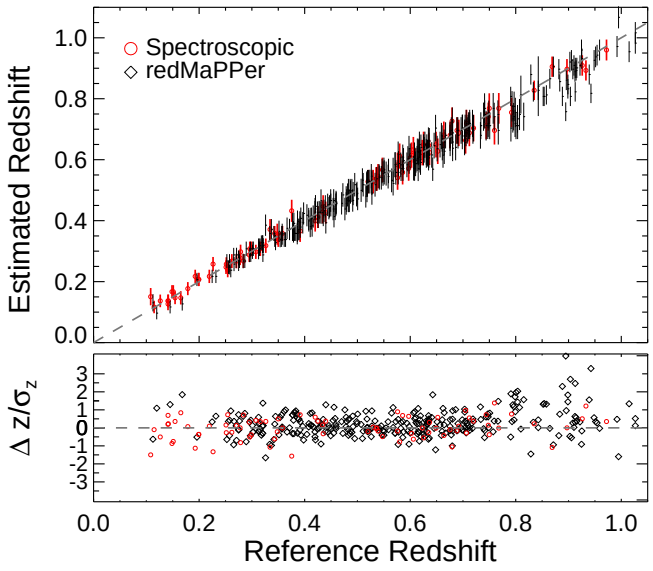

Figure 4. (Top panel) Comparison of estimated red-sequence redshifts from PISCO imaging data to spectroscopically measured redshifts (81 systems; red) and redshifts estimated by the redMaPPer scanning-mode algorithm (318 systems; black). (Bottom panel) The distribution of residuals over the redshift uncertainties; for the RM-PISCO comparison we add the individual uncertainties in quadrature. In general we find excellent agreement between the redshifts measured from PISCO and both the RM and spectroscopic samples below $z \sim 0.75$.

SPT-ECS literature search) at $0.108 < z < 0.72$ in the Pan-STARRS1 footprint, finding $\sigma_z/(1+z) \sim 0.03$ in these shallower data.

We search the optical/NIR imaging for an excess of red-sequence galaxies (or alternatively 1.6 μm rest-frame galaxies in the case of *Spitzer* and WISE confirmations) in the vicinity (2-3′) of the SPT cluster candidates. We call a cluster "confirmed" when significant excesses of these galaxies over background are identified (see e.g., B15 for more details on the confirmation procedure). In Song et al. (2012) we estimated that $< 4\%$ of cluster candidates identified via this procedure would be false associations and, for clusters in common between the PISCO and DES imaging, we can cross check our assigned confirmations against the statistical process described in Section 4.1.1. We note that this is of course a lower limit to the false association rate as the DES data is also of finite redshift reach. In this comparison we find that $\sim 1\%$ (3/318) of candidates with RM cluster matches that were also targeted with PISCO were assigned a different cluster counterpart when using the PISCO data. In two circumstances the PISCO data were insufficiently deep to correctly confirm the higher-redshift ($z \sim 0.9$) clusters while the remaining system was a superposition of two rich clusters ($\lambda = 75$ and $\lambda = 65$) for which the targeted RM algorithm selected the lower redshift system as the richer cluster and the PISCO data the higher.

For confirming higher-redshift systems without targeted *Spitzer* or Magellan/Fourstar data we combine data from "unWISE" with optical source catalogs. Following Gonzalez et al. (2019), we adopt a 1.″5 matching radius to associate WISE sources with optical galaxies and exclude sources with $i < 21.3$ and W1-W2 < 0.2 as these cuts were found to remove low-redshift ($z < 0.8$) galaxies. Similar to the analysis of clusters with *Spitzer* imaging, we search for a local excess of galaxies at 1.6 μm rest frame in the vicinity of the SPT cluster candidates. We validated this search process on clusters from the SPT-SZ sample (B15; Khullar et al. 2019) with spectroscopic redshifts $z > 0.85$, finding that we were able to robustly confirm 20/23 of these systems. From this spectroscopic sample we were able to quantify the redshift uncertainty in our WISE measurements as $\sigma_z/(1+z) \sim 0.1$. Improving this redshift precision via more sophisticated catalog cuts and photometric analysis of the WISE data is work in progress.

4.2.3. *2dFLenS*

The 2dFLenS survey (Blake et al. 2016) targeted luminous red galaxies (LRGs) at $z < 0.9$ with a primary focus on measuring redshift-space distortions and—in combination with KiDS survey data—galaxy-galaxy lensing (Joudaki et al. 2018) and the characterization of redshift distributions via cross-correlation (Johnson et al. 2017). There is significant overlap between the southern field of 2dFLenS and SPT-ECS. A number of visually identified brightest cluster galaxies from SPT clusters were targeted in a spare-fiber program (though all but two were lost owing to weather) and here we identify additional 2dFLenS sources associated with SPT clusters. First, for each confirmed candidate in the SPT sample at $z < 0.9$, we search for spectroscopic LRGs within 2.5′ of the cluster location and find 47 systems with spectroscopic galaxy associations. Repeating the process on the 40 random position catalogs provided by the 2dFLenS team[12] we find an average of 17 such matches per mock catalog, resulting in ∼30 matches over random for the real data sample. We further improve the purity of the matching by restricting matched galaxies to have redshifts within 2σ of the photometric redshift error (or $\delta z < 0.015$ for clusters with spectroscopic redshifts) and find 39 clusters with spectroscopic galaxy counterparts including 2 systems that were targeted as part of the spare fiber program, compared to an aver-

[12] http://2dFLens.swin.edu.au/

age of 2 systems for the random catalogs. We list these systems in the Appendix in Table 7.

5. THE CLUSTER SAMPLE

In this section we describe the new SZ-selected cluster sample. We also compare the properties of these clusters to those of SZ-selected clusters identified by *Planck* in the SPT-ECS region. Using the confirmation criteria presented in Section 4, we confirm 244 of 266 candidates at $\xi \geq 5$. We also leverage the DES and other imaging data to confirm an additional 204 clusters at $4 < \xi < 5$ but note that while the DES imaging is sufficient for cluster confirmation out to $z \sim 0.8 - 1.0$ in the SPT-ECS-DES overlap region, our follow-up of this lower-significance sample is otherwise highly incomplete.

While the confirmation process is still ongoing, we can compare these numbers to our expected numbers of false detections as estimated in Section 3.4. As discussed in B15, expectations from simulations were found to be in good agreement with observations of the more uniformly and deeply imaged SPT-SZ sample. At $\xi \geq 5$ where our optical follow-up imaging is sufficient to confirm clusters to at least $z \sim 0.85$, we find 22 unconfirmed candidates compared to the expected 21 ± 4. This places an empirical lower limit on the purity of 91% for the $\xi > 5$ SZ candidate sample which, when compared to the simulation prediction, suggests that there are relatively few clusters that remain to be confirmed. For the $\xi \geq 4.5$ SZ candidate sample, where the follow-up is generally more heterogeneous/incomplete, we find 180 currently unconfirmed candidates compared to 174 ± 13 expected, resulting in a lower limit to the purity of 64%.

The confirmed cluster candidates have a median redshift of $z = 0.49$ and median mass (calculated as described below in Section 5.1.1) of $M_{500c} \sim 4.4 \times 10^{14} M_{\odot} h^{-1}$. Twenty-one of the systems are at $z > 1$, bringing the total number of $z > 1$ systems from SPT-SZ, SPTpol 100d (Huang et al. 2019), and SPT-ECS to over 75 out of $> 1,000$ confirmed systems. The mass and redshift distribution of the cluster sample as compared to other SZ-selected samples, as well as a histogram of the redshift distribution of the SPT samples, are shown in Figure 5. We note that, given the lack of deep NIR data redder than $z-$band, the RM algorithm can systematically underestimate redshifts at $z > 0.9$ which may be the source of the small gap in the cluster redshift distribution at $z \sim 1.1$.

In Figure 6, we present an estimate of the survey completeness as a function of mass and redshift for our main sample at $\xi > 5$ using the $\xi-$mass relation (see below in Section 5.2). The survey is on average $> 90\%$ complete at all redshifts $z > 0.25$ for masses above $M_{500c} \sim 6.5 \times 10^{14} M_{\odot} h^{-1}$ (in comparison to $M_{500c} \sim 5.5 \times 10^{14} M_{\odot} h^{-1}$ for the SPT-SZ survey at the same significance threshold), with the mass at which the survey is 90% complete shifting by less than $1 \times 10^{14} M_{\odot} h^{-1}$ from the mean between the fields. The mass corresponding to a fixed completeness value falls as a function of redshift, with the survey on average 90% complete at $M_{500c} = 5.4 \times 10^{14} M_{\odot} h^{-1}$ at $z > 1$. In Table 8, we provide a complete listing of the candidates at $\xi \geq 5$ including their positions, detection significances and the filter scales that maximize these significances. For confirmed clusters we also include redshifts, estimated masses, optical richness measures (where available), and we flag notable properties about the systems. In Table 9 we provide a similar listing for the lower-significance confirmed systems.

As mentioned in Section 4.1.6 we also conducted a literature search for previously identified clusters, finding 147 SPT-ECS candidates have been previously reported including a number of systems in the Abell and *Planck* cluster samples (Abell 1958; Abell et al. 1989; Planck Collaboration et al. 2016a) as well small numbers of systems in other samples (e.g., APM, MACS, SWXCS, MaDCoWS, Dalton et al. 1997; Cavagnolo et al. 2008; Mann & Ebeling 2012; Liu et al. 2015b; Gonzalez et al. 2019). By far the largest overlap is with the *Planck* PSZ2 sample; we explore this in more detail in Section 5.3.

5.1. *Comparison to the SPT-SZ Cluster Abundance*

The cluster catalog extracted from SPT-ECS should be statistically consistent with the catalog extracted from the SPT-SZ survey once the different survey properties such as depth are accounted for. To test this, we use a cluster number count (NC) analysis to calibrate the parameters of the ξ–mass scaling relation assuming a fixed cosmology and compare the results with those obtained for SPT-SZ.

5.1.1. *The SZ ξ–Mass Relation*

To connect the observed SZ significance, ξ, to cluster mass we adopt an observable–mass scaling relation of the form

$$\langle \ln \zeta \rangle = \ln\Big[A_{\rm SZ} \left(\frac{M_{500c}}{3 \times 10^{14} M_{\odot} h^{-1}}\right)^{B_{\rm SZ}} \left(\frac{H(z)}{H(0.6)}\right)^{C_{\rm SZ}}\Big], \tag{4}$$

$$P(\ln \zeta | M, z) = \mathcal{N}\left[\langle \ln \zeta \rangle (M, z), \sigma^2_{\ln \zeta}\right] \tag{5}$$

where $A_{\rm SZ}$ is the normalization, $B_{\rm SZ}$ the slope, $C_{\rm SZ}$ the redshift evolution, $\sigma_{\ln \zeta}$ the log-normal scatter on ζ, and $H(z)$ is the Hubble parameter. The variable ζ represents the "unbiased" significance that accounts for the

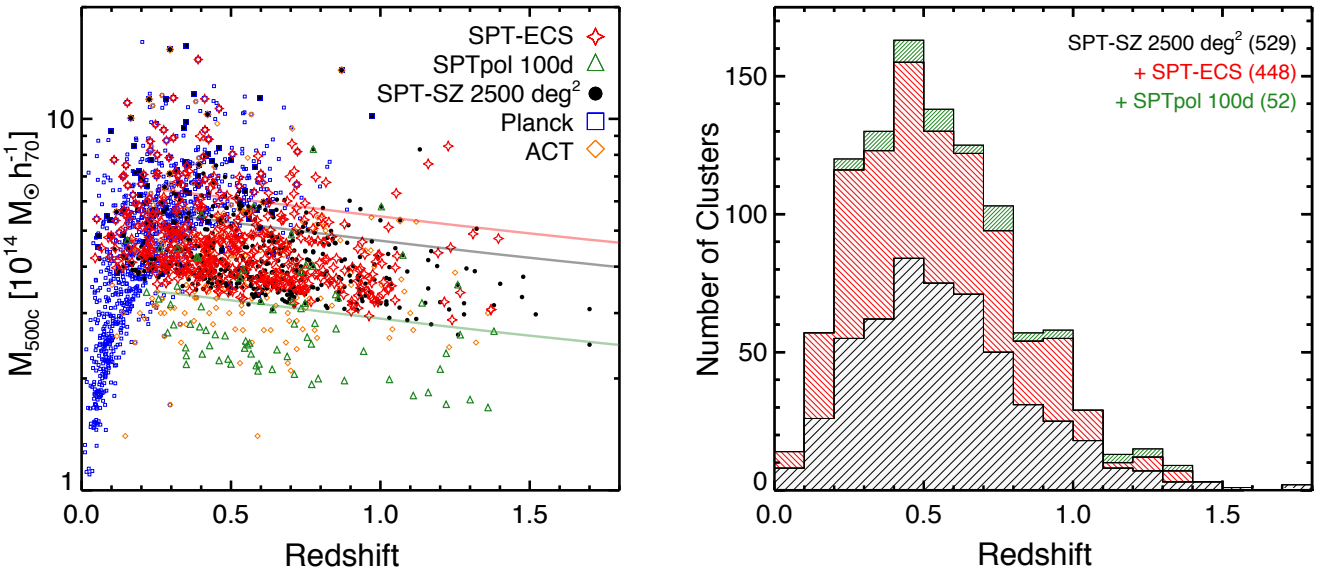

Figure 5. (Left) The mass and redshift distribution of the SPT-ECS cluster sample detected at $\xi \geq 4$. The median redshift of the sample is $z = 0.49$ and the median mass is $M_{500c} \sim 4.4 \times 10^{14} M_\odot h^{-1}$. Overplotted are cluster samples from other SZ surveys including the 100d SPTpol survey (green triangles; Huang et al. 2019), the 2500d SPT-SZ Survey (black circles; Bleem et al. 2015b, with redshifts updated as in Bocquet et al. 2019); the PSZ2 cluster sample from Planck Collaboration et al. (2016a) (blue squares), and the cluster samples from the ACT collaboration (orange diamonds; Hasselfield et al. 2013; Hilton et al. 2018). Clusters found in both SPT and other samples are plotted at the SPT mass and redshift and, for clusters in common between other samples, at the mass and redshift at which the cluster was first reported. We also plot at $z > 0.25$, as solid colored lines, the 90% completeness thresholds for $\xi \geq 5$ for the three SPT surveys (see also Figure 6). (Right) A redshift histogram of the three reported SPT cluster surveys. The number of clusters in each survey—with each cluster only reported once (so that e.g., clusters in both SPTpol 100d and SPT-SZ are only counted once)—are listed to the right of each survey name. The contribution from the SPTpol 100d survey is plotted on top in green right-diagonal hatch, the contribution from the SPT-ECS survey is plotted in red left-diagonal hatch, and the contribution to the total from the SPT-SZ survey is plotted in black right-diagonal hatch. Combined with these other two samples, the SPT-ECS sample brings the number of SZ-detected clusters reported by the SPT collaboration to over 1,000.

maximization of ξ over position and filter scales during cluster detection:

$$P(\xi|\zeta) = \mathcal{N}(\sqrt{\zeta^2 + 3}, 1) \tag{6}$$

for $\zeta > 2$ (Vanderlinde et al. 2010). As in previous SPT publications, we rescale $A_{\rm SZ}$ on a field-by-field basis to account for the variable depth of the survey: $A_{\rm SZ,field} = \gamma_{\rm field} \times A_{\rm SZ}$ (e.g., Reichardt et al. 2013; de Haan et al. 2016). These field renormalization factors, $\gamma_{\rm field}$, are computed using the simulations described in Section 3.4 and are reported in Table 1 on the same reference scale as the analogous factors for the SPT-SZ survey.

The different fields of the SPT-SZ and SPT-ECS surveys have a small amount of overlap at the field boundaries. We correct the field areas such that the total effective survey area corresponds to the unique sky area that is surveyed. These corrections are between 0.03% and 1.9%. SZ detections in the field overlap regions are matched by keeping the candidate with the larger detection significance ξ. Note that this approach is different from the one adopted in de Haan et al. (2016); Bocquet et al. (2019), who double-counted clusters in the field overlap regions in SPT-SZ in their NC analyses. The exact treatment of the field boundaries has negligible impact on our results; for example, the change in our total predicted cluster counts due to not correcting for the field overlap area is much smaller than the recovered uncertainty.

5.1.2. $\gamma_{\rm ECS}$ *Constraints from the Cluster Abundance*

We model the cluster sample as independent Poisson draws from the halo mass function. The likelihood function for the vector of cosmological and scaling relation parameters $\boldsymbol{p}$ is

$$\ln \mathcal{L}(\boldsymbol{p}) = \sum_i \ln \frac{dN(\xi_i, z_i|\boldsymbol{p})}{d\xi dz} - \int_{z_{\rm cut}}^{\infty} dz \int_{\xi_{\rm cut}}^{\infty} d\xi \frac{dN(\xi, z|\boldsymbol{p})}{d\xi dz}. \tag{7}$$

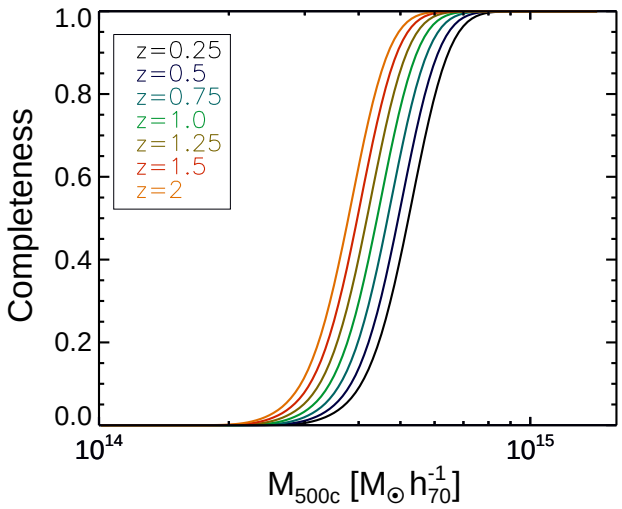

Figure 6. The average (across all fields) completeness as a function of mass and redshift for the SPT-ECS survey at $\xi \geq 5$, the ξ threshold for which we provide the complete candidate list for the full survey. The survey is on average 90% complete for all redshifts at $z > 0.25$ for masses above $M_{500c} \sim 6.5 \times 10^{14} M_{\odot} h^{-1}$. This completeness is derived for a fixed cosmology as discussed in Section 5.1.1 and Bocquet et al. (2019).

The sum runs over all clusters i in our sample, and

$$\frac{dN(\xi, z|\boldsymbol{p})}{d\xi dz} = \iint dM\, d\zeta \left[P(\xi|\zeta) P(\zeta|M, z, \boldsymbol{p}) \frac{dN(M, z|\boldsymbol{p})}{dM dz} \Omega(z, \boldsymbol{p}) \right] \quad (8)$$

where $\Omega(z, \boldsymbol{p})$ is the survey volume and $dN/dMdz$ is the halo mass function given by Tinker et al. (2008). The second line in Eq. 7 corresponds to the total number of clusters in the survey.

We analyze the SPT-ECS NC assuming our fixed ΛCDM cosmology. By construction of our scaling relation model, the amplitude $A_{\rm SZ}$ and the correction factor $\gamma_{\rm ECS}$ (introduced in Section 3.4) are fully degenerate. The constraints on the SZ scaling relation parameters $B_{\rm SZ}$, $C_{\rm SZ}$, and the scatter $\sigma_{\ln\zeta}$ from SPT-SZ and SPT-ECS are consistent at the $\ll 1\sigma$ level. To test the consistency of the relative scaling between the two surveys, we analyze the joint NC from SPT-SZ and SPT-ECS. In this analysis, any residual in the relative calibration between the two surveys is absorbed by $\gamma_{\rm ECS}$. We recover

$$\gamma_{\rm ECS} = 1.124 \pm 0.045. \quad (9)$$

We provide and discuss an alternate calibration of $\gamma_{\rm ECS}$ in section 6.1.

5.2. *Mass Estimation*

The ξ–mass relation defined above in Eqs. 4–6 allows us to compute mass estimates for all sample clusters. We adopt $A_{\rm SZ} = 4.08$, $B_{\rm SZ} = 1.65$, $C_{\rm SZ} = 0.64$, and $\sigma_{\ln\zeta} = 0.20$. These mean scaling relation parameters were determined in Bocquet et al. (2019) for our fixed reference flat ΛCDM cosmology and using the SPT-SZ sample at $\xi > 5$ and $z > 0.25$. As discussed in the previous section, the SZ scaling relation parameters barely shift between a NC analysis using SPT-SZ clusters alone and one using SPT-SZ and SPT-ECS clusters, and we thus use the SPT-SZ only numbers presented in Bocquet et al. (2019) for consistency with their mass estimates.

5.3. *Comparisons to the Planck Cluster Sample*

There is naturally significant overlap between the *Planck* and SPT-ECS cluster samples as both identify massive clusters by the SZ effect. Here we focus our comparison on the reported masses and redshifts, two quantities critical for cosmological analyses. To directly compare the properties of the two samples for clusters in common we first associate the catalog from Planck Collaboration et al. (2016a) with the SPT-ECS catalog using a $4'$ matching radius and find that 82 SPT candidates (81 confirmed clusters) detected at $\xi > 4$ match *Planck* systems within this radius.

Overall we find good agreement between the redshifts for matched clusters, with three outliers for which the estimated redshifts reported in the *Planck* catalog and this work differ by $\delta_z > 0.1$. These three systems each have redshifts in this work from the RM algorithm. Two of the systems (J0046−3911 and J0516−2236) have photometric redshifts reported in the literature while the third system, J0348−2144 (PSZ2 G215.19−49.65, separated from the SPT position by $0.'58$), was associated in the *Planck* catalog with ACO 3168 (RXC J0347.4−2149) for which a spectroscopic redshift of $z = 0.2399$ was derived from 5 cluster members in Chon & Böhringer (2012). This system is significantly offset ($8.'6$, $8.'9$) from the SPT and *Planck* detections, respectively. We instead associate this cluster candidate with a closer ($1.'2$, $1.'7$) and richer ($\lambda = 186$ versus 10) system at $z = 0.347 \pm 0.008$.

Beyond the direct redshift comparisons, we also provide here redshifts for 13 PSZ2 systems from Planck Collaboration et al. (2016a); 11 of these clusters were not confirmed by the Planck collaboration. These systems are listed in Table 3. Two of these clusters have previously reported redshifts in Maturi et al. (2019) and a third we associate with ACO S 1048 (Abell et al. 1989). We find good agreement with the Maturi et al. (2019) redshift estimate for PSZ2 G011.92−63.53 but find $\delta_z > 0.2$ for PSZ2 G011.36−72.93.

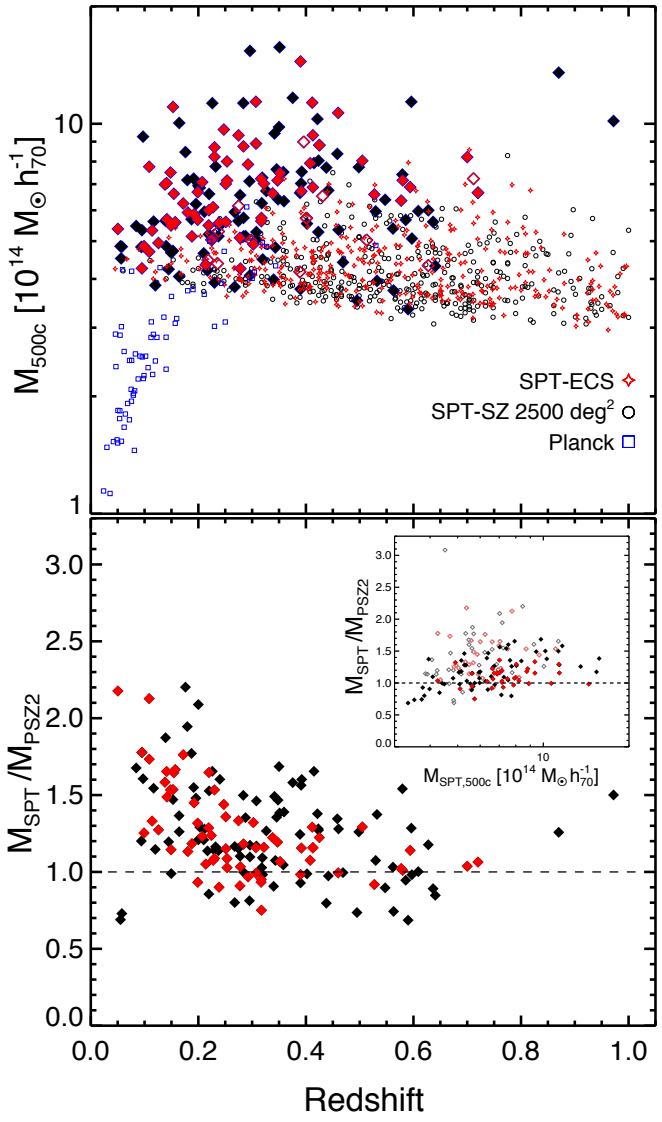

Figure 7. Top panel: Mass versus redshift for SPT and *Planck* clusters in the sky area surveyed by SPT. Small open symbols represent clusters that reside only in one of the catalogs while the filled diamonds represent clusters (plotted at the SPT masses) that are in both SPT-SZ and *Planck* (black, blue outline) and SPT-ECS and *Planck* (red, blue outline). The 13 *Planck* clusters for which we report a redshift in Table 3 are plotted as large hollow diamonds. In this plot we omit *Planck* clusters that fall within regions excluded by the SPT point source veto (see Section 3.2) and restrict the x-axis to focus on redshifts where the samples overlap. Bottom panel: Again using red diamonds for clusters in common between *Planck* and SPT-ECS and black diamonds for those in *Planck* and SPT-SZ, we plot the ratio of reported SPT to *Planck* masses versus redshift and (inset) versus SPT mass. In the inset panel clusters at $z \geq 0.25$ ($z < 0.25$) are plotted as filled (open) symbols.

We can also compare the reported SZ mass estimates for each of these samples. In Figure 7 we show the *Planck* and SPT clusters in the SPT-ECS and SPT-SZ footprints. In the top panel, plotted as small hollow symbols, are clusters that are only found in one of the catalogs, while the filled diamonds represent clusters that are in both SPT and *Planck*. The 13 *Planck* clusters for which we report a redshift from SPT-ECS in Table 3 are plotted as large hollow diamonds. Including clusters from the SPT-SZ region brings the joint SPT-*Planck* sample to a total of 150 clusters with mass estimates for which the reported redshifts differ by $\delta_z < 0.1$[13], and 88 such systems at $z > 0.25$ where SPT masses are expected to be unbiased. In the bottom panel we plot the ratio of SPT to *Planck* mass as a function of redshift and, in the inset, as a function of the SPT mass estimate. Qualitatively we notice a trend with redshift where at $z < 0.25$ the ratio of the SPT to *Planck* masses is significantly higher than at higher redshifts ($1.44^{+0.05}_{-0.14}$ vs. $1.1^{+0.055}_{-0.03}$). We note that mass estimates for SPT clusters at $z < 0.25$ are more uncertain—though not expected to be biased high—given increased noise contributions from both the primary CMB and atmosphere as well as the removal of large scale sky signal by the map filtering.

Comparisons to the *Planck* SZ masses are often reported in terms of a mass bias, 1-b, where $M_{Planck} = (1-b)M_{\rm True}$. For purposes of comparison here we treat the SPT masses as the "true" cluster masses and both compute the median mass bias and check for a mass-dependent trend. The latter is achieved via making use of the Bayesian linear regression routines provided by Kelly (2007), and fitting for the power-law index, α:

$$M_{\rm 500c\ Planck} \propto M^{\alpha}_{\rm 500c\ SPT}. \quad (10)$$

Here we consider only the statistical errors in the SPT and *Planck* masses as we are directly comparing properties of the same clusters.

As discussed in Battaglia et al. (2016), one must take care in such comparisons as they can be impacted at the level of 3-15% in (1-b) by the presence of Eddington bias in the reported *Planck* masses.[14] We follow Battaglia et al. (2016) and recompute the SPT masses not accounting for this bias. Restricting to a subset of 69 clusters where the absolute difference between the *Planck* and SPT signal-to-noise was less than two (so

[13] We implement the redshift cut so that the masses would not be significantly different simply from the use of different redshifts in the mass estimation process.

[14] See e.g., https://wiki.cosmos.esa.int/planckpla2015/index.php/Catalogues#SZ_Catalogue

the bias would be somewhat comparable), we find a median $(1\text{-}b)_{\rm Eddington} = 0.77^{+0.02}_{-0.025}$ and $\alpha = 1.03 \pm 0.14$ for the full sample and $(1\text{-}b)_{\rm Eddington} = 0.80^{+0.09}_{-0.01}$ and $\alpha = 1.3 \pm 0.27$ for 15 such clusters with $0.25 < z < 0.35$ and uncorrected $M_{500c\,\rm SPT} > 5.5 \times 10^{14}$ (where both samples are more complete). To aid comparison with previous studies in the literature we also compute these values for the entire matched sample with *debiased* SPT masses, finding $(1\text{-}b) = 0.83 \pm 0.02$ for the full matched sample and $(1\text{-}\ b) = 0.91^{+0.01}_{-0.05}$ and $\alpha = 0.75 \pm 0.06$ at $z > 0.25$.

Comparisons between (Eddington-biased) *Planck* and (debiased) SPT mass estimates were previously reported by Planck Collaboration et al. (2016a) and Hilton et al. (2018) for the SPT-SZ and PSZ2 samples. Planck Collaboration et al. (2016a) found the SPT-reported masses to be on average 20% higher than the *Planck* masses—in good agreement with the results derived above with the larger SPT-SZ and SPT-ECS sample. Hilton et al. (2018) explored the relation between SPT-SZ, ACT, and PSZ2 masses finding the mean mass ratio of ACT to SPT clusters to be 1.00 ± 0.04 for 18 clusters in common between the samples; the SPT-ECS sample provides no additional overlapping systems between ACT and SPT to further this comparison. Hilton et al. (2018) additionally noted a mass-dependent trend between the *Planck* and SPT/ACT masses, finding for the ACT comparison $\alpha = 0.55 \pm 0.18$, a result $\sim 1\sigma$ lower than our value.

A number of studies have also contrasted the estimated *Planck* masses against masses estimated using other observables, with values of $(1\text{-}b)$ ranging from ~ 0.7 to unity (e.g., von der Linden et al. 2014 , 0.688 ± 0.072; Hoekstra et al. 2015, 0.76 ± 0.05; Smith et al. 2016, 0.95 ± 0.04; Medezinski et al. 2018, 0.80 ± 0.14). Our recovered values fall within this range. Other works report values for the power-law index, α (e.g., Schellenberger & Reiprich 2017, 0.76 ± 0.08; Mantz et al. 2016, 0.73 ± 0.02) consistent with our measurement when using debiased SPT masses.

We also examine the SPT-ECS footprint for clusters detected by *Planck* but not by SPT. Based on the selection function shown in Figure 6, we expect the SPT-ECS sample to contain essentially all confirmed *Planck* clusters at $z \geq 0.25$ in the common sky area. Including the new confirmations discussed above, there are 117 confirmed *Planck* clusters that fall within the SPT-ECS footprint, and 82 of these are associated with SPT cluster candidates at $\xi > 4$. Of the remaining 35 clusters in *Planck* but not confirmed by SPT, 32 are at redshift $z < 0.25$—where the SPT filtering both reduces the completeness of the catalog and the fidelity of the mass estimates—and 5 of these 32 confirmed clusters also excluded because they are in regions excluded by the SPT point source veto. For the 3 *Planck* clusters at $z > 0.25$ but not confirmed by SPT, we find two of these systems match candidates just below the SPT-selection threshold with PSZ2 G244.74−28.59 (*Planck* S/N=5.9, $z = 0.33$) at $\xi = 3.97$ and PSZ2 G251.13-78.15 (S/N=4.6, $z = 0.3$) at $\xi = 3.2$. There is also radio source nearby to PSZ2 G244.74−28.59, which—based on the methodology of Section 3.5—could reduce the ξ value by 0.08 to 0.7 for a source spectral index of -1 to -0.5. The final unmatched cluster, PSZ2 G282.14+38.29 (S/N=4.9, $z = 0.33$ with validation from Pan-STARRS) is flagged as having a nearby point source detected at 857 GHz and is measured at $\xi = -0.3$ in our sample. We do not detect a large excess of red-sequence galaxies in Pan-STARRS at this cluster location. While the SZ flux from one source (PSZ2 G244.74−28.59) may be diminished by the presence of a nearby radio source (which should also influence the *Planck* detection) and we do not independently confirm G282.14+38.29, we find the SPT selection to be consistent with expectations as relates to the PSZ2 sample with 39/42 of the reported *Planck* clusters at $z \geq 0.25$ and not in a point-source vetoed region also in the SPT-ECS sample. Further exploration of the differences between the estimated masses for the *Planck* and SPT samples will require detailed modeling of the selection functions of the two surveys in their jointly accessible mass and redshift ranges and is beyond the scope of this work.

5.4. *The SPT-ECS Strong Lensing Subsample*

The strong gravitational lensing regime, often identified via the presence of highly magnified and multiply imaged background galaxies lensed by foreground gravitational potentials, provides a unique probe of the cores of massive structures. Galaxy clusters have long been recognized as areas in which to productively search for strong gravitational lenses (see review by Meneghetti et al. 2013 and more recent works by Kneib & Natarajan 2011; Bayliss et al. 2011; Lotz et al. 2017; Diehl et al. 2017; Sharon et al. 2019 amongst many others). We examine the SPT-ECS sample for signatures of strong lensing in the Magellan/PISCO and DES imaging data as well as in archival and dedicated observations from the *Hubble Space Telescope*, the latter from a snapshot program (PID 15307, PI: Gladders) designed to characterize the central regions of massive clusters from SPT-SZ and SPT-ECS.

We find that 44 of the SPT-ECS systems exhibit unambiguous signs of strong lensing; we flag all of these systems in Tables 8 and 9. Some of these systems have been previously identified as strong lenses—see Smail

Table 3. New confirmations of *Planck* clusters.

PSZ2 Name	z	Separation ($'$)
PSZ2 G011.36-72.93	0.63±0.04	2.4
PSZ2 G011.92-63.53[a]	0.24±0.02	1.1
PSZ2 G025.07-78.64	0.225±0.033	0.3
PSZ2 G029.55-60.16	0.218	2.8
PSZ2 G210.02-56.38	0.236±0.004	0.7
PSZ2 G216.76-41.84[b]	0.39±0.01	1.1
PSZ2 G221.06-44.05	0.396	0.8
PSZ2 G227.61-84.72	0.432±0.009	0.7
PSZ2 G231.74-70.59	0.275±0.005	1.7
PSZ2 G240.71-74.03	0.40±0.01	0.8
PSZ2 G271.53+36.41	0.51±0.04	0.8
PSZ2 G282.11+38.61	0.30±0.02	1.6
PSZ2 G295.27+32.25	0.71±0.04	1.0

NOTE—Redshifts and angular separations (in arcminutes) from SPT cluster positions for PSZ2 Planck Collaboration et al. (2016a) candidates reported without redshifts that are associated with SPT-ECS clusters. We find good agreement with the redshift reported for PSZ2 G011.92−63.53 by Maturi et al. (2019) but find $\delta_z > 0.2$ for PSZ2 G011.36−72.93. We also note that we associate PSZ2 G029.55−60.16 with ACO S 1048 (Abell et al. 1989).

[a] Associated by Planck Collaboration et al. (2016a) with ACO 3296, but no redshift provided

[b] Associated by Planck Collaboration et al. (2016a) with ACO S 443, but no redshift provided

et al. (1991); Sand et al. (2005); Covone et al. (2006); Zitrin et al. (2011); Hamilton-Morris et al. (2012); Gruen et al. (2014); Ebeling et al. (2017, 2018); Newman et al. (2018); Repp & Ebeling (2018); Jacobs et al. (2019); Petrillo et al. (2019); Coe et al. (2019)—and in the online data for Tables 8 and 9 we also link individual previously known strong lenses to these works. In total over 110 systems from SPT-SZ and SPT-ECS have been identified as strong gravitational lenses; a robust statistical characterization of the PISCO and *HST* data will be the subject of future work. In Figure 8 we display high-quality PISCO data for three of the SPT-ECS strong lenses as well as data from our *HST* program for the third.

6. THE SZ PROPERTIES OF THE JOINT SPT-REDMAPPER CLUSTER SAMPLE

Having constructed the SPT-ECS cluster sample we now leverage the overlap between the DES and SPT surveys to jointly characterize the SZ and richness properties of massive clusters in the Year 3 DES redMaPPer optically selected catalog (see Section 4.1.1). We focus on two properties here: the richness-mass relation of these systems (a key ingredient in cosmological analyses of optical clusters that has been previously probed in numerous works e.g., Farahi et al. 2016; Simet et al. 2017; Geach & Peacock 2017; Murata et al. 2018; McClintock et al. 2019; Raghunathan et al. 2019) and the offsets between the SZ-based cluster centers and the optical centers as defined by the most probable central galaxy as determined by the RM algorithm. This distribution is useful for both cosmological studies (e.g., as an important input in weak-lensing mass calibration of clusters, Johnston et al. 2007; George et al. 2012; Dietrich et al. 2019) and astrophysical studies, as it probes the dynamical states of clusters (Sanderson et al. 2009; Mann & Ebeling 2012; Rossetti et al. 2016). It can also serve as a test of cluster-centering algorithms.

Following a similar criterion to Saro et al. (2015) we cross match the optically selected RM sample with SZ clusters by:

- Rank-ordering each cluster list: for the SPT clusters by decreasing ξ, and for the RM clusters by decreasing λ
- Matching each SZ system to the richest RM cluster within $\delta_z = 0.1$ and projected separation between the SZ and RM center < 1.5 Mpc at the cluster redshift and then
- Removing each matched RM cluster from the possible matching pool and continuing the process until the last SZ cluster has been checked for a match.

Note that we do *not* compute a probability of random association here for each SZ cluster in this list as we have already statistically identified a high-probability association between a cluster detected by the RM algorithm run in "scanning" mode (Section 4.2.1) and the SZ detection. The matching criterion we've chosen in this selection allows us to more fully capture the properties of the RM algorithm when it is run in its standard, blind-search mode; in particular clusters that scatter low in richness in the blind search are not cut from this analysis. This procedure is also repeated for the full SPT-SZ sample (updating the Saro et al. 2015 results which centered on the DES Science Verification Region). We confirm 13 new clusters at $\xi > 4.5$ via this method, the majority of which are above the redshift limits reported in B15 (though we found some of these limits were overestimated in cases of poor seeing). The new clusters are reported in Table 10 and we note that

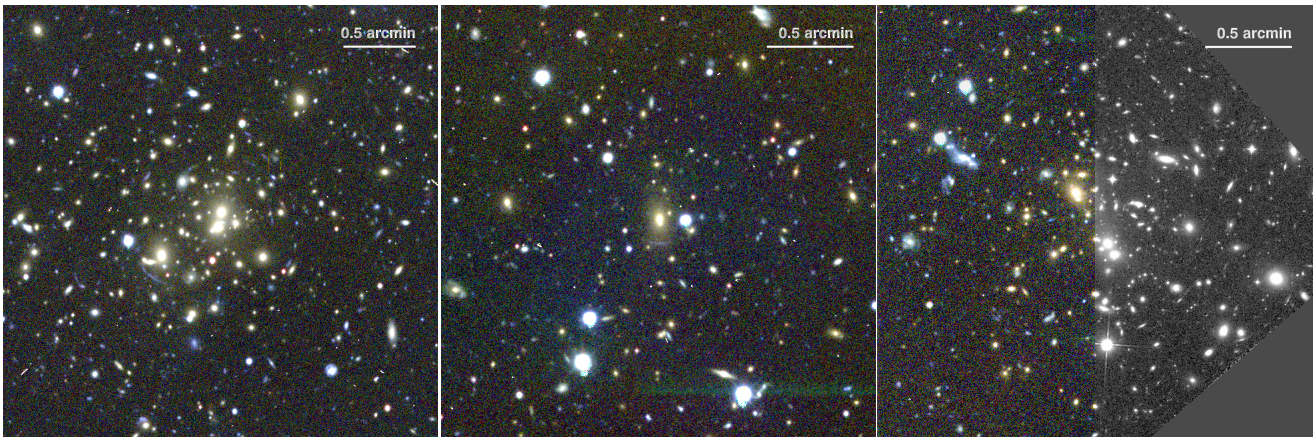

Figure 8. Three strong lensing clusters from the SPT-ECS survey. (Left) SPT-CL J0512−3848 at $z = 0.33$, (Middle) SPT-CL J1223−3014 at $z = 0.48$, (Right) SPT-CL J0049−2440 at $z = 0.53$ (first reported as Vidal 14; de Propris et al. 1999). In each panel we show ~ 300 s exposure imaging from PISCO in the *gri*-bands. This data was taken in good ($< 0.7''$) seeing that enables the strong lensing identification. In the right panel we also show F110W data from our ongoing *HST* snapshot program.

the sample of $\xi < 4.5$ SPT-SZ systems will be discussed in detail in M. Klein et al. (in preparation).

Including SZ cluster candidates detected at $\xi > 4.5$ in the SPT-SZ survey (Bleem et al. 2015b) we find 652 clusters in the ensemble SPT-RM cluster sample. Limiting the redshift range to $z > 0.25$ reduces the sample to 584 systems, and to the volume-limited catalog results in a sample of 249 (410) clusters at $\xi \geq 5(4)$; the richness versus ξ (normalized for the field scaling factors, see 5.1.1) are shown in Figure 9.

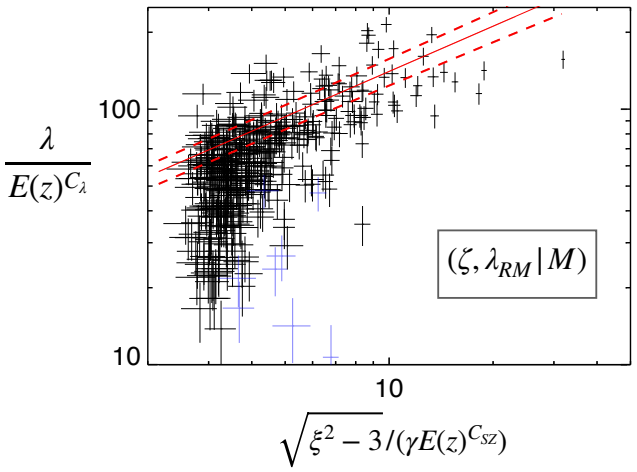

Figure 9. Richness versus normalized ξ values for the ensemble SPT-RM volume-limited cluster sample; light blue points are clusters for which $> 30\%$ of the DES data was masked in the vicinity of the SPT cluster. The ξ values are normalized by the field scaling factors discussed in Section 5.1.1. Overplotted in red is the best-fit $\lambda - \xi$ relation as calculated in Section 6.1.

6.1. *The Richness–Mass Relation of SPT-RM Clusters*

We use the optical richness (λ) measurements of SPT clusters matched to the Y3 RM catalog to calibrate the richness–mass relation, taking the SPT selection into account. Assuming our fiducial fixed cosmology, we simultaneously constrain the SZ scaling relation parameters through the number counts of the SPT cluster sample (as discussed in Section 5.1.2) and the parameters of the richness scaling relation. This analysis follows Saro et al. (2015) with the exception that we now also account for the effects of correlated scatter among ζ and richness.

6.1.1. *Richness–Mass Relation: Likelihood Function*

Along with the ζ–mass relation defined above in Eq. 4, we define the richness–mass relation

$$\langle \ln \lambda \rangle = \ln A_\lambda + B_\lambda \ln \left(\frac{M_{500c}}{3 \times 10^{14} M_\odot h^{-1}} \right) + C_\lambda \ln \left(\frac{E(z)}{E(z=0.6)} \right). \quad (11)$$

A covariance matrix describes the correlated intrinsic scatter between the two observables ζ and λ

$$\Sigma_{\zeta-\lambda} = \begin{pmatrix} \sigma^2_{\ln\zeta} & \rho_{\mathrm{SZ}-\lambda}\sigma_{\ln\zeta}\sigma_{\ln\lambda} \\ \rho_{\mathrm{SZ}-\lambda}\sigma_{\ln\zeta}\sigma_{\ln\lambda} & \sigma^2_{\ln\lambda} + \lambda^{-1} \end{pmatrix}. \quad (12)$$

The contribution λ^{-1} to the intrinsic scatter in richness represents the Poisson noise in the number of member galaxies observed at a fixed cluster mass. We note that we expect positive correlation in the scatter between ζ

and λ as both are projected quantities (see e.g., Angulo et al. 2012).

The joint scaling relation then reads

$$P\Big(\begin{bmatrix}\ln\zeta\\ \ln\lambda\end{bmatrix}|M,z\Big)=\mathcal{N}\Big(\begin{bmatrix}\langle\ln\zeta\rangle(M,z)\\ \langle\ln\lambda\rangle(M,z)\end{bmatrix},\Sigma_{\zeta-\lambda}\Big). \quad (13)$$

Following Bocquet et al. (2019), the likelihood function for our number counts and richness calibration analysis is

$$\begin{aligned}\ln\mathcal{L}(\boldsymbol{p}) = &\sum_i \ln\frac{dN(\xi_i,z_i|\boldsymbol{p})}{d\xi dz}\\ &-\int_{z_{\rm cut}}^{\infty}dz\int_{\xi_{\rm cut}}^{\infty}d\xi\frac{dN(\xi,z|\boldsymbol{p})}{d\xi dz}\\ &+\sum_j \ln P_j(\text{match})P(\lambda^{>5}_{\text{obs},j}|\xi_j,z_j,\boldsymbol{p})\end{aligned} \quad (14)$$

up to a constant, where the first sum runs over all clusters i in the SPT sample above $\xi>5$ and $z>0.25$ and the second sum runs over all SPT clusters j for which a RM richness measurement is available. Note that the first two lines represent the number-count likelihood defined earlier in Equation 7. The term $P(\text{match}) = 1-P(\text{random})$ describes the excess probability of matching a RM cluster to an SPT cluster over random associations $P(\text{random})$. The other term in the last line is computed as

$$\begin{aligned}P(\lambda_{\rm obs}|\xi,z,\boldsymbol{p}) = &\iiint dM\,d\zeta\,d\lambda\;[\\ &P(\lambda_{\rm obs}|\lambda)P(\xi|\zeta)\\ &P(\zeta,\lambda|M,z,\boldsymbol{p})P(M|z,\boldsymbol{p})\;]\,.\end{aligned} \quad (15)$$

Finally, we account for the richness cut $\lambda_{\rm obs}>5$ in the volume-limited redMaPPer catalog and evaluate

$$P(\lambda^{>5}_{\rm obs}|\xi,z,\boldsymbol{p}) = \frac{\Theta(\lambda_{\rm obs}>5)P(\lambda_{\rm obs}|\xi,z,\boldsymbol{p})}{\int_5^\infty d\lambda_{\rm obs}\Theta(\lambda_{\rm obs}>5)P(\lambda_{\rm obs}|\xi,z,\boldsymbol{p})} \quad (16)$$

with the step function Θ.

6.1.2. *Richness–Mass Relation: Results*

With this machinery in place we are now ready to explore the mass-richness relation of the SPT-RM sample. Assuming our fiducial cosmology, we evaluate the likelihood presented in Eq. 14 of the SPT cluster number counts (which constrains the SZ scaling relation parameters), and the likelihood of the RM richnesses (which constrains the RM richness scaling relation parameters). We only use the SPT-SZ sample for the SPT number counts (to enable an independent constraint on $\gamma_{\rm ECS}$, described below) but we use redMaPPer richnesses for the full SPT-SZ+SPT-ECS sample.

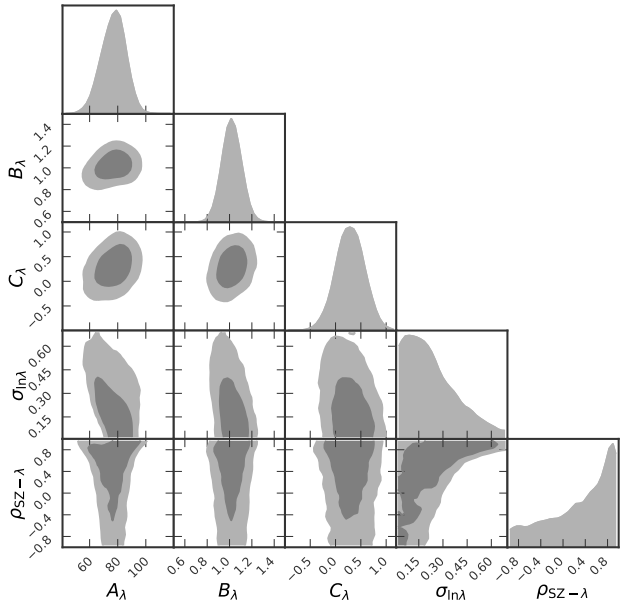

Figure 10. Parameters of the richness–mass relation defined in Eq. 11 and the correlation coefficient, $\rho_{\text{SZ}-\lambda}$, between the SZ signal (ζ) and richness.

Table 4. Parameters of the Richness-Mass Relation.

Parameter	Constraint
A_λ	76.9 ± 8.2
B_λ	1.020 ± 0.080
C_λ	0.29 ± 0.27
$\sigma_{\ln\lambda}$	0.23 ± 0.16
ρ	>-0.78 (95% CL)

NOTE—The richness–mass relation is defined in Eq 11. We also quote the constraint on the correlation coefficient between the scatter in the SZ signal and richness $\rho_{\text{SZ}-\lambda}$. The constraints are obtained using redMaPPer matches to the $\xi>4.5, z>0.25$ SPT sample.

We present the constraints on the richness–mass relation in Figure 10 and in Table 4. Compared to previous constraints using 19 clusters from SPT-SZ at $\xi>4.5$ in the DES Science Verification region (Saro et al. 2015), we find a normalization that is $\sim1.2\sigma$ higher, with the slope and redshift evolution consistent.

We also compare against the DES weak lensing analysis of the Year 1 RM sample reported in McClintock et al. (2019), which was also analyzed at our fiducial cosmology. Note that the DES weak lensing analysis con-

strains $P(M_{200m}|\lambda)$—with masses defined with respect to the *mean* density of the Universe—whereas our analysis constrains $P(\lambda|M_{500c})$. We convert M_{500c} to M_{200m} assuming a Navarro, Frenk and White (NFW; Navarro et al. 1996) profile and the concentration–mass relation from Child et al. (2018).[15] We invert our relation as

$$P(M_{200m}|\lambda) = \int dM_{200m} P(\lambda|M_{200m}) P(M_{200m}) \quad (17)$$

with the halo mass function prior $P(M_{200m})$.

In Figure 11, we show the mass–lambda relation from our work and examples from the literature. At our scaling relation pivot redshift ($z = 0.6$, see Equation 11), the scaling relation normalizations are consistent at $\lambda \approx 60$ or $M_{200m} \approx 5 \times 10^{14} M_\odot$. However, there are some visible differences in the slope. We approximate[16] the slope F_λ in our $P(M_{200m}|\lambda)$ relation as

$$F_\lambda \equiv 1/B_\lambda = 0.981 \pm 0.077. \quad (18)$$

We find our slope is ∼30% shallower than the slope from the DES Y1 analysis ($F_\lambda = 1.356 \pm 0.052$; McClintock et al. 2019), with a 4σ offset between the two constraints. To reproduce the slope of the McClintock et al. (2019) relation we would require a significant shift in our assumed cosmology along the Ω_m and σ_8 degeneracy direction (see e.g., Costanzi et al. 2018); however a full cosmological interpretation is beyond the scope of this work, and would depend on fully accounting for selection effects in the RM sample under study as well as on degeneracies and covariances in a wider multi-dimensional parameter space.

A weak-lensing analysis using data from the Sloan Digital Sky Survey (SDSS) finds an amplitude and slope that are consistent with McClintock et al. (2019) at better than 1σ (Simet et al. 2017). Another weak-lensing study using SDSS data finds a much shallower slope centered at $\lambda \propto M^{0.64}$ using lensing alone; this slope becomes consistent with unity—and thus our measurement—when combining lensing and cluster abundance (Murata et al. 2018). Qualitatively similar results are presented in an analysis of the richness–mass relation using first-year HSC data (Murata et al. 2019). A weak-lensing calibration of an X-ray selected cluster sample yields constraints on the richness–mass relation that are centered on the results from McClintock et al. (2019), but with large uncertainties (Mantz et al. 2016).

[15] We use the Colossus package https://bitbucket.org/bdiemer/colossus

[16] Strictly speaking, we compare the slopes of the λ–mass and the mass–λ relations. We checked that the conversion of our relation to mass–λ mostly shifts the amplitude of the relation while leaving the slope almost unchanged.

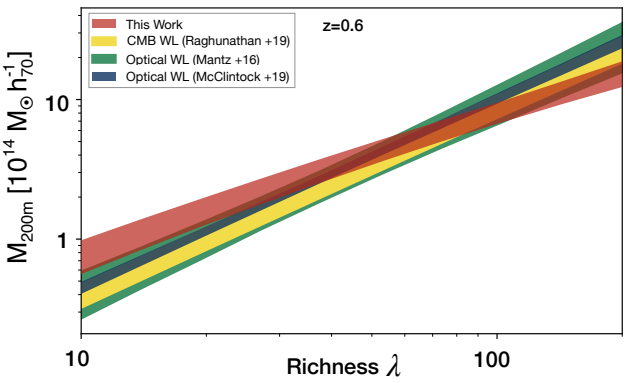

Figure 11. The mass–λ relation evaluated at our pivot redshift $z = 0.6$ determined from SPT cluster number counts assuming our fiducial ΛCDM cosmology. We convert our $\lambda - M_{500c}$ relation to $M_{200m} - \lambda$ for ease of comparison with the literature. The relations calibrated from DES Y1 shear or CMB lensing (the latter driven by an informative prior) favor steeper slopes, but there is good agreement at their pivot richness $\lambda_0 = 40$ (McClintock et al. 2019; Raghunathan et al. 2019). The calibration from an X-ray selected sample with optical weak-lensing provides a richness–mass relation that is very similar to the DES Y1 shear result (Mantz et al. 2016).

Moving beyond optical weak lensing, two calibrations of the mass–λ relation using lensing of the CMB (Baxter et al. 2018; Raghunathan et al. 2019) recover amplitudes of the mass–λ relation that are compatible with both the calibration from DES Y1 shear measurements and this work. Note however, that the slope parameters were not constrained by the CMB lensing measurements, where informative priors were applied. The richness-mass relation has also been calibrated using the clustering of clusters (Baxter et al. 2016) and the measurement of pairwise velocity dispersions (Farahi et al. 2016); both methods show consistency at the 2σ level. Finally, a study of the phase-space of galaxy dynamics provides a calibration of the richness–mass relation with a slope that is consistent with unity at $< 1\sigma$ (Capasso et al. 2019). However, their relation exhibits strong redshift evolution, which leads to an offset in the relations at our pivot redshift $z = 0.6$.

6.1.3. *Richness–Mass Relation: Constraint on γ_{ECS}*

By using only the SPT-SZ data in the number counts we can also use this test to independently evaluate our estimated value for γ_{ECS} presented in Section 5.1.2. We obtain a calibration of the correction factor γ_{ECS} between SPT-SZ and SPT-ECS

$$\gamma_{ECS} = 1.054 \pm 0.075. \quad (19)$$

This determination of $\gamma_{\rm ECS}$ is different from the result presented above in section 5.1.2. In both cases, $A_{\rm SZ}$ is constrained to yield number counts from SPT-SZ that match our fixed fiducial cosmology. In section 5.1.2, $\gamma_{\rm ECS}$ was calibrated by also demanding that the SPT-ECS number counts match that cosmology—any relative offset in the amplitude of the ζ–mass relation between SPT-SZ and SPT-ECS is thus absorbed by $\gamma_{\rm ECS}$. In the calibration presented here, the redMaPPer richnesses serve as the relative anchor between the SPT-SZ and SPT-ECS surveys. The two determinations of $\gamma_{\rm ECS}$ agree at the 0.8σ level. We conclude that our empirical modeling of the full SPT-SZ+SPT-ECS sample with an overall amplitude offset is adequate and when reporting cluster masses we adopt the mean recovered constraint from the more precise NC analysis result as our default.

6.2. *redMaPPer-SZ center offset distribution*

We next explore the distribution of separations between the redMaPPer and SPT-determined cluster centers. Based on visual inspection of > 100 matched X-ray and RM clusters in SDSS, Rozo & Rykoff (2014) found that the gas centers and central galaxies should be well aligned (within 50 kpc) 80% of the time, with it being rare to find a separation of > 300 kpc between the two (results consistent with previous findings by e.g., Lin & Mohr 2004). In the SDSS sample, the RM algorithm selected the visually identified central galaxy in $86 \pm 3\%$ of systems and had a long uniform tail to 800 kpc for the remainder of systems. These gas-central galaxy separations were further quantified for RM clusters by Saro et al. (2015) with 19 SPT-RM clusters in DES Science Verification data and Zhang et al. (2019) for 144 (67) systems in SDSS (DES); the latter analysis using archival *Chandra* X-ray data as analyzed in Hollowood et al. (2018). With differing model parameterizations these works found $\sim 63-84\%$ of all clusters to be well-centered.

Following these previous works, we adopt two different models for this offset distribution for the SPT-RM sample, one modeling offsets relative to the cluster mass scale (via R_{500c}) and the other relative to a cluster extent that scales as a function of RM galaxy richness. Both of these models assume that the offset distribution can be modeled as a central core of well-aligned clusters with small separation combined with a subdominant population of clusters with large offsets. Physically this corresponds to the cluster population being composed of a mixture of relaxed and merging clusters with some additional scatter introduced via possible misidentification of central galaxies by the RM algorithm.

The dynamical state of the cluster population is also traced by the morphology of the cluster gas, which can be measured by X-ray observations (note the filtering applied to the SPT maps makes it difficult to extract a robust gas morphological measurement from the SZ data). The X-ray morphology has been measured via the $A_{\rm phot}$ statistic for 50 of the SPT-RM clusters that are also part of a *Chandra* X-ray Visionary Project (XVP; PI: Benson, Nurgaliev et al. 2017); 38 of the systems in the Zhang et al. (2019) DES Y1 analysis mentioned above are part of the SPT-XVP. The $A_{\rm phot}$ statistic is a quantification of the amount of azimuthal asymmetry present in the X-ray photon count distribution and has been shown to be a robust morphological measure even when used on X-ray data with a relatively low number of counts (~ 2000 counts/cluster) such as the SPT-XVP observations (Nurgaliev et al. 2013). We plot as an inset in Figure 12 the SZ-optical-offset distribution of these 50 clusters. The outlier in this inset plot is SPT-CL J2331−5051($A_{\rm phot} = 0.14$) which may be captured pre-merger with SPT-CL J2332−5053. The RM algorithm has selected what appears to be the central galaxy of the latter cluster and found a smaller structure of $\lambda = 8$ at the location of SPT-CL J2331−5051 which is the more massive system inferred from both the SZ and X-ray observations (see further discussion of this system in Andersson et al. 2011 and Huang et al. 2019). The $A_{\rm phot}$ distribution is a continuum, but adopting the somewhat arbitrary choice of McDonald et al. (2017) with $A_{\rm phot} < 0.1$ classified as "relaxed" (17 systems) and $A_{\rm phot} > 0.5$ as "disturbed" (10 systems) we find the median offset of the relaxed (disturbed) systems to be $0.067^{+0.005}_{-0.02} R_{500c}$ ($0.23^{+0.01}_{-0.04} R_{500c}$), with the relaxed systems having a closer alignment between the SZ center and the RM most probable central galaxy, as expected.

6.2.1. *Offset Distribution relative to R_{500c}*

We first consider the offset distribution relative to the cluster scale R_{500c}. For this analysis we split the cluster population into two parts: a high-significance subset with $\xi \geq 5$ (249 clusters, median $\lambda = 81$) which is the threshold used for SPT cosmological analyses (see e.g., Bocquet et al. 2019), and a lower-significance sample at $4 < \xi < 5$ (161 systems, median $\lambda = 55$). In Figure 12 we plot the distribution of separations between the SZ centroids and RM central galaxies for these two subsamples.

To characterize this distribution our model follows that of Saro et al. (2015). We have added a third Gaussian term to account for the long tail to large separations. As noted above such a tail was also previously seen in analyses of SDSS clusters (and given its small

sample size, the absence of a significant tail in Saro et al. 2015 is unsurprising). Examination of clusters with the largest separations revealed systems where the RM algorithm identified a bright galaxy near what was the lesser of two SZ peaks in merging clusters (see e.g., Figure 13 and the discussion of SPT-CL J2331−5051 above), rich systems split into multiple detections (i.e., "mispercolation", see discussion in Hollowood et al. 2018), systems with significant masking of the optical data near the SPT position, and—for a few of the lower-significance clusters—systems with higher (but still less than 5%) chance of random association between the SZ candidate and RM cluster.

We write the probability distribution as a function of the fractional separation, $x = r_{\rm offset}/R_{500c}$ as:

$$P(x) = 2\pi x\Big(\frac{\rho_0}{2\pi\sigma_0^2}e^{\frac{-x^2}{2\sigma_0^2}} + \frac{\rho_1}{2\pi\sigma_1^2}e^{\frac{-x^2}{2\sigma_1^2}} + \frac{(1-\rho_0-\rho_1)}{2\pi\sigma_2^2}e^{\frac{-x^2}{2\sigma_2^2}}\Big) \quad (20)$$

convolved with the SPT positional uncertainty. The SPT positional uncertainty is given by the cluster detection significance, ξ, and detection scale, θ_c

$$\sigma_{SPT} = \frac{\sqrt{\theta_{\rm beam}^2 + (\kappa_{\rm SPT}\theta_c)^2}}{\xi} \quad (21)$$

convolved with a general astrometric uncertainty of 4-6″ (see Section 2.2 and W. Everett et al., (2019, in preparation)). where $\theta_{\rm beam} = 1.3'$ is a combination of the 95+150 GHz beams and $\kappa_{\rm SPT}$ is a parameter of order unity (Story et al. 2011; Song et al. 2012).

We use the `emcee` package in Python (Foreman-Mackey et al. 2013) to conduct a Markov Chain Monte Carlo (MCMC) maximum likelihood analysis adopting priors of

$$\begin{aligned} 0 \leq &\rho \leq 1.0 \\ 0 \leq &\rho_0 - \rho_1 \leq 1 \\ 0 \leq &\sigma_0 \leq 0.3 \\ \sigma_0 < &\sigma_1 < 2 \\ \sigma_1 < &\sigma_2 < 3 \\ 0.5 \leq &\kappa_{\rm SPT} \leq 2. \end{aligned}$$

Results for this parameterization for both samples are shown in Figure 12 and reported in Table 5. We note that the lower-significance sample does not have the power to constrain $\kappa_{\rm SPT}$ and so we fix it to the best-fit value from the $\xi \geq 5$ sample.

For the high-significance, $\xi \geq 5$ sample we find that the fraction of clusters in the well-centered component in this version of RM is consistent with Saro et al. (2015) ($\rho_0 = 67^{+6}_{-8}\%$ vs. $63^{+15}_{-25}\%$) with the uncertainty reduced a factor of 2 in this work. The width of this component is slightly smaller ($\sigma_0 = 0.02 \pm 0.01$ vs. 0.07 ± 0.02) and the width of the second component is also smaller ($\sigma_1 = 0.15 \pm 0.03$ versus 0.25 ± 0.07), though we note that some of this spread is absorbed in the third Gaussian term that captures the offsets to high R_{500c}.

Table 5. Miscentering Model 1 Fits

Parameter	$\xi \geq 5$	$4 < \xi < 5$
ρ_0	$0.675^{+0.07}_{-0.08}$	$0.54^{+0.13}_{-0.20}$
σ_0	$0.02^{+0.01}_{-0.01}$	$0.065^{+0.03}_{-0.035}$
ρ_1	$0.25^{+0.08}_{-0.06}$	$0.29^{+0.14}_{-0.16}$
σ_1	$0.15^{+0.03}_{-0.03}$	$0.24^{+0.14}_{-0.11}$
σ_2	$0.70^{+0.125}_{-0.09}$	$0.48^{+0.15}_{-0.07}$
$\kappa_{\rm SPT}$	1.0 ± 0.2	–

Note—Best-fit miscentering parameters for the SPT-RM Volume Limited Sample as characterized in Equation 20.

Turning to the lower significance sample, we find it overall less well-centered than the higher significance sample, but with the parameters also less well constrained. Future studies using SZ clusters from the 500d SPTpol survey or from SPT-3G will significantly increase the number of lower-mass clusters in our SZ-matched sample and will allow us to more robustly explore miscentering trends as a function of mass.

6.2.2. *Offset Distribution relative to R_λ*

As a second model of the SZ-central galaxy offset distribution we explore a miscentering model tied to the RM cluster radius, R_λ, where

$$R_\lambda = (\frac{\lambda}{100})^{0.2} h^{-1} \ \ {\rm Mpc}. \quad (23)$$

R_λ is determined by the RM cluster finding algorithm and corresponds to the maximum separation between the RM central galaxy and cluster members that contribute to the optical richness measurement. Here we focus on the better constrained SPT clusters at $\xi > 5$ and we plot this distribution in Figure 14. As can be seen, there are a significant number of systems (14 of 249, 6%) that have offsets greater than R_λ. Examination of these clusters shows, unsurprisingly, that they display similar characteristics to the outliers in the previous subsection (and many are in common). Additionally it is worth noting that issues that reduce the richness estimate will more adversely affect a fractional offset when the cluster

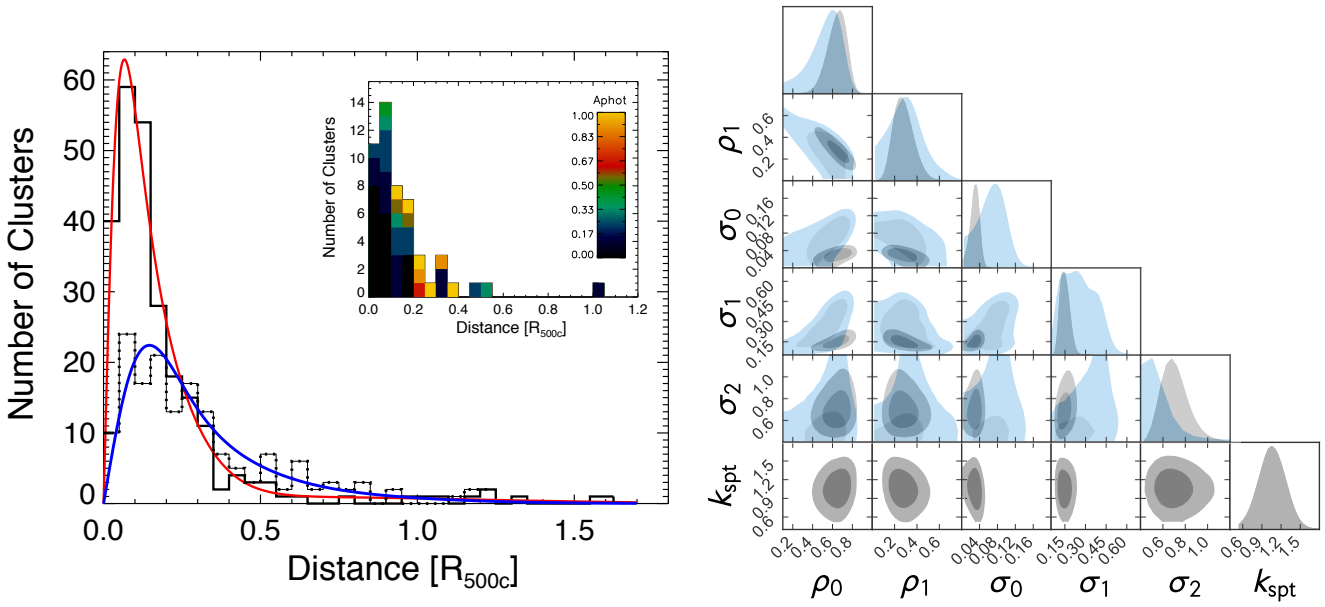

Figure 12. (Left) The distribution of offsets between SPT centroids and RM most probable centers as a fraction of R_{500c} for SPT systems in the RM volume-limited sample. The sample at $\xi \geq 5$ is plotted in solid black and at $4 < \xi < 5$ with a dotted line. Overplotted in red (blue) is the best fit to the model given by Equation 20 for the high (low) significance sample. Inset is the offset-distribution of the 50 SPT-RM clusters for which the X-ray morphology statistic $A_{\rm phot}$ has been measured. As expected the more relaxed systems (with smaller $A_{\rm phot}$ values) on average have less spatial separation between the central galaxy and gas center. (Right) Constraints on the parameters of the offset probability distribution model. Best-fit values are given in Table 5. As the lower-significance sample does not have the power to constrain $\kappa_{\rm SPT}$ we fix its value to the best-fit value from the higher-significance sample for this analysis.

scale is set by the richness measure (e.g., R_λ) as opposed to being set by the SZ mass estimate.

Following McClintock et al. (2019) and Zhang et al. (2019), we model the probability distribution for the separation between SZ centroids and RM central galaxies as the combination of an exponential distribution that reflects the well-centered systems and a Gamma distribution $\Gamma(2,\tau)$ that characterizes those clusters with larger separations:

$$P(x) = \rho \frac{1}{\sigma_\lambda} e^{-\frac{x}{\sigma_\lambda}} + (1-\rho)\frac{x}{\tau^2} e^{-\frac{x}{\tau}} \qquad (24)$$

where now $x = r_{\rm offset}/R_\lambda$, σ_λ characterizes the exponential distribution, τ is the scale parameter of the Gamma distribution function and, as in the previous model, we also incorporate the SPT positional uncertainties when conducting the fit.

The two-dimensional convolutions required for properly incorporating the SPT positional uncertainty in this model are computationally expensive to repeat many times in an MCMC analysis. Numerical computations of the probability distribution can instead be replaced by relatively inexpensive, yet highly precise emulators. For this purpose, we use Gaussian Processes (GP, Rasmussen & Williams 2006), a method that has facilitated robust forward modeling of various astrophysical functions (e.g., Heitmann et al. 2006, Habib et al. 2007 and other applications). We detail the construction and validation of our emulator of the miscentering distribution model in Appendix A.

For this analysis we adopt the priors:

$$0.3 \leq \rho \leq 1.0$$
$$0.001 \leq \sigma_\lambda \leq 0.25$$
$$0.05 \leq \tau \leq 1.0$$

We plot these results in Figure 14 and report the parameter constraints in Table 6. In Figure 14 we also over plot the best-fit model curves from Zhang et al. (2019) convolved with the SPT positional uncertainty.

While Zhang et al. (2019) explored the separation between X-ray peaks and central galaxies, the analysis here quantifies the central galaxy offset from the gas center averaged over a larger scale via the SPT matched filter. This should generally have a small effect; studies with X-ray centering proxies (see e..g, Mann & Ebeling 2012) have found an additional 20-60 kpc ($\sim 0.02 - 0.06 R_\lambda$)

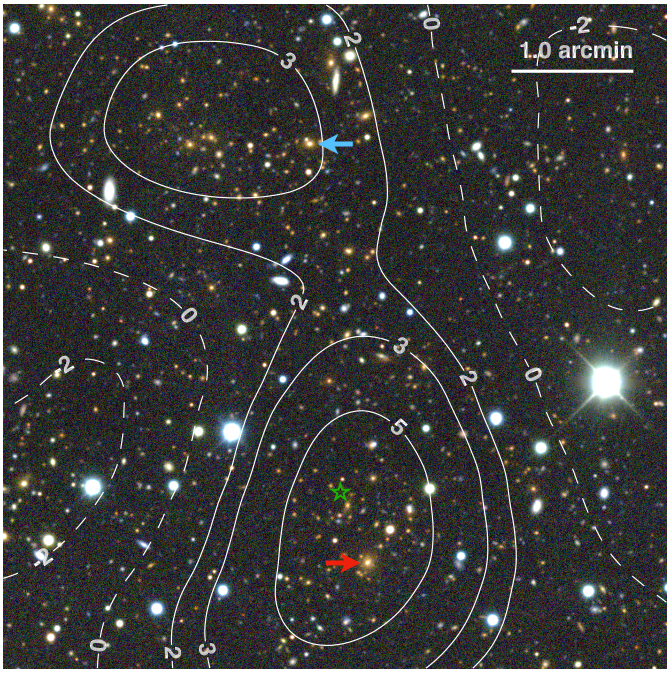

Figure 13. SPT-CL J0543−4250, an illustration of the small fraction of systems where the separation between RM most probable center (identified by blue arrow, $\lambda = 136, z = 0.609 \pm 0.008$) and the SZ center is greater than the RM cluster scale R_λ. The RM algorithm does identify a smaller group at the same redshift (red arrow, $\lambda = 14$), significantly closer to the SPT location (green star). Shown is DES *g*-,*r*-,*i*-band imaging overlaid with SPT-SZ matched filter detection contours.

scatter in the BCG and X-ray centroid separation (to which our measurement is most analogous) as compared to the X-ray peak to BCG separation though there can be notable outliers in the case of merging clusters. With this caveat in mind, we find that our results at $\xi > 5$, with $\rho = 0.87^{+0.02}_{-0.03}$ of the clusters within the "well-centered" component of the distribution agree with previous RM results on DES ($\rho = 0.84^{+0.11}_{-0.07}$) and are higher than those found in SDSS ($\rho = 0.68^{+0.03}_{-0.05}$). However, our recovered value of τ is notably higher than previous results ($\tau = 0.69^{+0.12}_{-0.09}$, versus $0.16^{+0.11}_{-0.04}$) as it is significantly affected by clusters in the long tail. In comparison Zhang et al. (2019) only found 1 of 67 systems (1.5%) with gas-BCG separations at $R > R_\lambda$ compared to the 14 (6%) found here. If we reanalyze the cluster sample excluding systems with offsets $R > R_\lambda$, we find ρ and σ_λ significantly less well constrained ($\rho = 0.74^{+0.22}_{-0.30}$, $\sigma_\lambda = 0.105^{+0.045}_{-0.07}$) and τ shifted to lower values consistent with previous work ($\tau = 0.13^{+0.075}_{-0.045}$). It will be important in future weak lensing analyses to quantify this tail while incorporating all the cluster selection effects relevant to the analysis at hand as Zhang et al. (2019) found that shifts in τ at the 0.04 level can lead to systematic shifts in the weak lensing derived mass calibrations at the level of $\delta \log M_{200} = 0.015$.

Table 6.
Miscentering Model 2 Fits

Parameter	$\xi \geq 5$
ρ	$0.87^{+0.02}_{-0.03}$
σ	$0.12^{+0.015}_{-0.01}$
τ	$0.69^{+0.12}_{-0.09}$

Note—Best-fit miscentering parameters for the SPT-RM Volume Limited Sample as characterized in Equation 24.

7. CONCLUSIONS

In this work, we describe the SPTpol Extended Cluster Survey, a new 2770 deg^2 survey conducted at 95 and 150 GHz using the SPTpol receiver. Using a matched spatial-spectral filter with a SZ detection significance threshold of $\xi \geq 5$, we have identified 266 cluster candidates. Of these, we have confirmed and estimated redshifts for 244 clusters using a combination of external optical imaging data, primarily from the DES survey, and targeted observations with the Magellan/PISCO imager. With more incomplete followup, we also confirm an additional 204 systems at $4 < \xi < 5$. Approximately two-thirds of the confirmed clusters are first reported in this work.

We estimate cluster masses using a ξ-mass scaling relation, inferred from fitting the observed SZ-cluster density at $\xi > 5$ and redshift $z > 0.25$ to a fixed spatially flat ΛCDM cosmology. The SPT-ECS cluster sample has a median redshift of $z = 0.49$ with 20 clusters at $z > 1$, a median mass of $M_{500c} \sim 4.4 \times 10^{14} M_\odot h^{-1}$, and we unambiguously identify strong gravitational lensing in 44 systems. Selected data products for this catalog will be hosted at http://pole.uchicago.edu/public/data/sptsz-clusters.

We use 1.4 GHz observations from NVSS to estimate the amount of radio contamination in the SPT-ECS sample. We estimate a median radio contamination of 0.05 in units of the SZ detection significance, which is ∼1% of the SZ signal at the $\xi = 5$ detection threshold. We find that only ∼5% of these candidates would have a predicted radio contamination of >10% compared to the SZ signal level. When extending this test to consider only confirmed clusters at $\xi \gtrsim 4$, we find < 4% of these clusters would have a predicted radio contam-

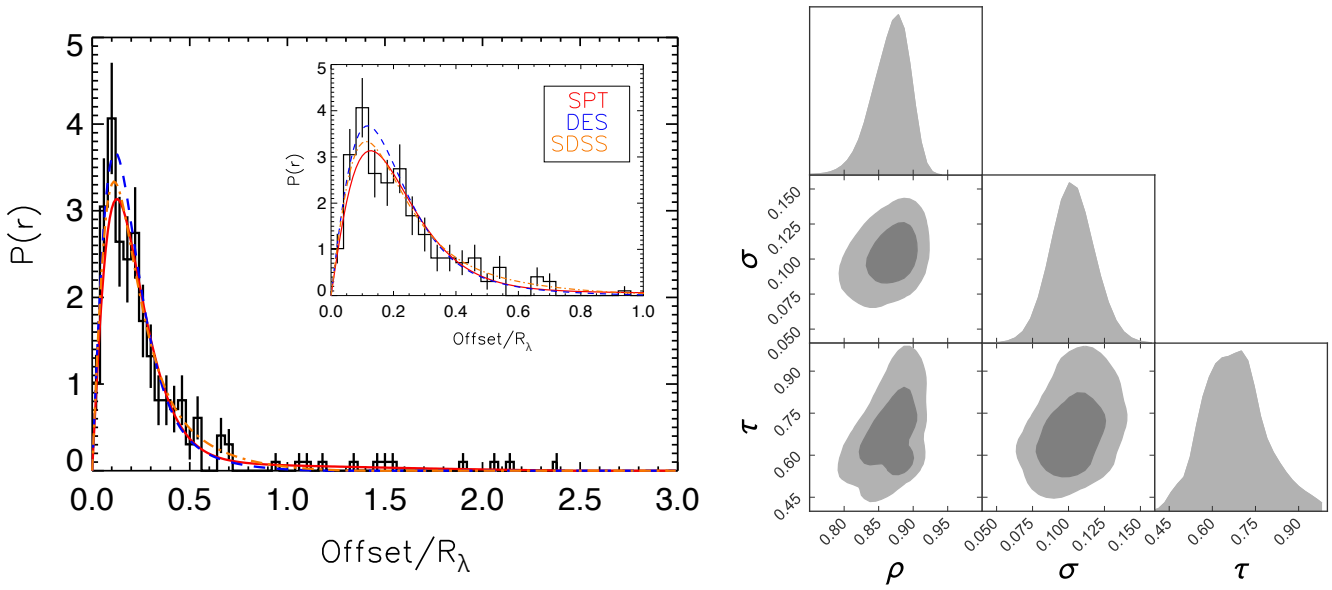

Figure 14. (Left) The distribution of separations between SPT centers and RM most probable central galaxies as a fraction of the RM cluster radius R_λ for systems at $\lambda > 20$, the richness threshold for DES cosmological analyses. Overplotted in red is the best fit to the SPT data and in orange (blue) are the best-fit models from Zhang et al. (2019) convolved with the SPT positional uncertainty. This latter analysis characterized the offsets between X-ray peaks and RM central galaxies for 144(67) systems in SDSS (DES). The large SPT-RM sample shows a higher fraction with large offsets than previous works. (Right) The best-fit model constraints. These results are overplotted in red in the left panel. We note that the derived value of τ is very sensitive to clusters with large separation.

ination of >10% compared to the SZ signal level. As this test was performed using an SZ-selected sample, it places a lower limit to the radio contamination of the SZ signal of massive clusters, as clusters with extremely bright radio sources could be missed by our SZ selection altogether. However, as discussed in Sections 3.5 and 3.6, such occurrences are expected to be rare at the redshifts of most interest for the SPT sample ($z > 0.25$).

We next associate SZ-selected cluster candidates from a combination of the SPT-ECS and SPT-SZ surveys with clusters from both the *Planck* PSZ2 sample and the DES Year 3 redMaPPer cluster catalog. We find general agreement with previous studies assessing the consistency of *Planck*- and SPT-derived masses, and that, as expected, the SPT catalogs contain the majority of PSZ2 clusters at $z > 0.25$ in the SPT footprint.

Considering the SPT and DES RM catalogs, we find 652 clusters that match with a false association probability $< 5\%$ at $\xi > 4.5$. When restricting this comparison to the redMaPPer volume-limited catalog at $z > 0.25$, we identify 410 systems. Using this sample, we characterize the offset distribution between the SZ center and central galaxy. We find general agreement with the constraints from previous studies (Saro et al. 2015; Zhang et al. 2019) but note our large sample size allows us to identify a significant tail of clusters to large separations not present in these previous works. We also use the SZ-mass estimates to constrain the optical richness-mass relation assuming a fixed standard cosmology. We find that our relation intersects with the previous weak lensing studies of McClintock et al. (2019); Raghunathan et al. (2019) at a richness of $\lambda = 60$, but that our SPT derived relation prefers a 28% shallower slope with the difference significant at the 4.0σ level. To reproduce the slope of the weak lensing analysis we would require a significant shift in our assumed cosmology, but we leave any quantitative conclusions to a future analysis. Regardless, our work highlights the value of consistency checks between scaling relations inferred from multi-wavelength observations, which should lead to constraints with better understood systematic uncertainties.

Combined with clusters detected from the SPT-SZ (B15) and SPTpol 100d surveys (Huang et al. 2019), this work increases the number of SZ-detected clusters reported by the South Pole Telescope to more than 1,000. Future SZ-selected cluster catalogs from the SPT will push to higher redshift and lower mass. From SPTpol, this includes the catalog from the completed 500 deg^2 survey, which is a factor of 5-10 deeper than SPT-ECS (Henning et al. 2018). The ongoing 1500 deg^2 SPT-3G survey (Benson et al. 2014) is expected to be even deeper, with a mass-selection threshold of

$\sim 10^{14} M_{\odot} h^{-1}$, which will enable the detection of $\gtrsim 4000$ clusters. This work will complement the wide-area cluster surveys to be conducted at X-ray (*eROSITA*, Predehl et al. 2010; Merloni et al. 2012) and optical/IR wavelengths (e.g., LSST, LSST Science Collaboration et al. 2009, *Euclid*, Euclid Collaboration et al. 2019, *WFIRST*, Spergel et al. 2015), as well as SZ surveys by AdvACT (Henderson et al. 2016) and Simons Observatory (Simons Observatory Collaboration et al. 2019), with all of the SZ surveys ultimately setting the stage for the next-generation CMB-S4 survey (Abazajian et al. 2016; CMB-S4 Collaboration et al. 2019).

ACKNOWLEDGEMENTS

Facilities: Blanco (DECAM), Hubble Space Telescope (WFC3), Magellan:Baade (FourStar), Magellan:Clay (PISCO, LDSS3C), NSF/US Department of Energy 10m South Pole Telescope (SPTpol), Spitzer (IRAC), AAT(2dF+AAOmega)

This work was performed in the context of the South Pole Telescope scientific program. SPT is supported by the National Science Foundation through grant PLR-1248097. Partial support is also provided by the NSF Physics Frontier Center grant PHY-0114422 to the Kavli Institute of Cosmological Physics at the University of Chicago, the Kavli Foundation and the Gordon and Betty Moore Foundation grant GBMF 947 to the University of Chicago. This work is also supported by the U.S. Department of Energy. PISCO observations are supported by NSF AST-1814719.

Work at Argonne National Lab is supported by UChicago Argonne LLC,Operator of Argonne National Laboratory (Argonne). Argonne, a U.S. Department of Energy Office of Science Laboratory, is operated under contract no. DE-AC02-06CH11357. We also acknowledge support from the Argonne Center for Nanoscale Materials. MG and LB acknowledge partial support from HST-GO-15307.001. BB is supported by the FermiResearch Alliance LLC under contract no. De-AC02-07CH11359 with the U.S. Department of Energy. The CU Boulder group acknowledges support from NSF AST-0956135. The McGill authors acknowledge funding from the Natural Sciences and Engineering Research Council of Canada, Canadian Institute for Advanced Research, and the Fonds de Recherche du Québec Nature et technologies. The UCLA authors acknowledge support from NSF AST-1716965 and CSSI-1835865. The Stanford/SLAC group acknowledges support from the U.S. Department of Energy under contract number DE-AC02-76SF00515. AS is supported by the ERC-StG 'ClustersXCosmo' grant agreement 716762, and by the FARE-MIUR grant 'ClustersXEuclid' R165SBKTMA. CH acknowledges support from the Max Planck Society and the Alexander von Humboldt Foundation, in the framework of the Max Planck-Humboldt Research Award endowed by the Federal Ministry of Education and Research, in addition to support from the European Research Council under grant number 647112. SJ acknowledges support from the Beecroft Trust and ERC 693024. TS acknowledges support from the German Federal Ministry of Economics and Technology (BMWi) provided through DLR under projects 50 OR 1610 and 50 OR 1803, as well as support from the Deutsche Forschungsgemeinschaft, DFG, under project SCHR 1400/3-1. The Melbourne authors acknowledge support from the Australian Research Council's Discovery Projects scheme (DP150103208).

The 2dFLenS survey is based on data acquired through the Australian Astronomical Observatory, under program A/2014B/008. This work is based in part on observations made with the Spitzer Space Telescope, which is operated by the Jet Propulsion Laboratory, California Institute of Technology under a contract with NASA.

Funding for the DES Projects has been provided by the U.S. Department of Energy, the U.S. National Science Foundation, the Ministry of Science and Education of Spain, the Science and Technology Facilities Council of the United Kingdom, the Higher Education Funding Council for England, the National Center for Supercomputing Applications at the University of Illinois at Urbana-Champaign, the Kavli Institute of Cosmological Physics at the University of Chicago, the Center for Cosmology and Astro-Particle Physics at the Ohio State University, the Mitchell Institute for Fundamental Physics and Astronomy at Texas A&M University, Financiadora de Estudos e Projetos, Fundação Carlos Chagas Filho de Amparo à Pesquisa do Estado do Rio de Janeiro, Conselho Nacional de Desenvolvimento Científico e Tecnológico and the Ministério da Ciência, Tecnologia e Inovação, the Deutsche Forschungsgemeinschaft and the Collaborating Institutions in the Dark Energy Survey.

The Collaborating Institutions are Argonne National Laboratory, the University of California at Santa Cruz, the University of Cambridge, Centro de Investigaciones Energéticas, Medioambientales y Tecnológicas-Madrid, the University of Chicago, University College London, the DES-Brazil Consortium, the University of Edinburgh, the Eidgenössische Technische Hochschule (ETH) Zürich, Fermi National Accelerator Laboratory, the University of Illinois at Urbana-Champaign, the Institut de Ciències de l'Espai (IEEC/CSIC), the Institut de Física d'Altes Energies, Lawrence Berkeley Na-

tional Laboratory, the Ludwig-Maximilians Universität München and the associated Excellence Cluster Universe, the University of Michigan, the National Optical Astronomy Observatory, the University of Nottingham, The Ohio State University, the University of Pennsylvania, the University of Portsmouth, SLAC National Accelerator Laboratory, Stanford University, the University of Sussex, Texas A&M University, and the OzDES Membership Consortium.

Based in part on observations at Cerro Tololo Inter-American Observatory, National Optical Astronomy Observatory, which is operated by the Association of Universities for Research in Astronomy (AURA) under a cooperative agreement with the National Science Foundation.

The DES data management system is supported by the National Science Foundation under Grant Numbers AST-1138766 and AST-1536171. The DES participants from Spanish institutions are partially supported by MINECO under grants AYA2015-71825, ESP2015-66861, FPA2015-68048, SEV-2016-0588, SEV-2016-0597, and MDM-2015-0509, some of which include ERDF funds from the European Union. IFAE is partially funded by the CERCA program of the Generalitat de Catalunya. Research leading to these results has received funding from the European Research Council under the European Union's Seventh Framework Program (FP7/2007-2013) including ERC grant agreements 240672, 291329, and 306478. We acknowledge support from the Brazilian Instituto Nacional de Ciência e Tecnologia (INCT) e-Universe (CNPq grant 465376/2014-2).

This manuscript has been authored by Fermi Research Alliance, LLC under Contract No. DE-AC02-07CH11359 with the U.S. Department of Energy, Office of Science, Office of High Energy Physics. The United States Government retains and the publisher, by accepting the article for publication, acknowledges that the United States Government retains a non-exclusive, paid-up, irrevocable, world-wide license to publish or reproduce the published form of this manuscript, or allow others to do so, for United States Government purposes.

The Pan-STARRS1 Surveys (PS1) and the PS1 public science archive have been made possible through contributions by the Institute for Astronomy, the University of Hawaii, the Pan-STARRS Project Office, the Max-Planck Society and its participating institutes, the Max Planck Institute for Astronomy, Heidelberg and the Max Planck Institute for Extraterrestrial Physics, Garching, The Johns Hopkins University, Durham University, the University of Edinburgh, the Queen's University Belfast, the Harvard-Smithsonian Center for Astrophysics, the Las Cumbres Observatory Global Telescope Network Incorporated, the National Central University of Taiwan, the Space Telescope Science Institute, the National Aeronautics and Space Administration under Grant No. NNX08AR22G issued through the Planetary Science Division of the NASA Science Mission Directorate, the National Science Foundation Grant No. AST-1238877, the University of Maryland, Eotvos Lorand University (ELTE), the Los Alamos National Laboratory, and the Gordon and Betty Moore Foundation.

REFERENCES

Abazajian, K. N., Adshead, P., Ahmed, Z., et al. 2016, ArXiv e-prints. https://arxiv.org/abs/1610.02743

Abbott, T. M. C., Abdalla, F. B., Allam, S., et al. 2018, The Astrophysical Journal Supplement Series, 239, 18, doi: 10.3847/1538-4365/aae9f0

Abell, G. O. 1958, ApJS, 3, 211, doi: 10.1086/190036

Abell, G. O., Corwin, Jr., H. G., & Olowin, R. P. 1989, ApJS, 70, 1, doi: 10.1086/191333

Adami, C., Giles, P., Koulouridis, E., et al. 2018, A&A, 620, A5, doi: 10.1051/0004-6361/201731606

Alberts, S., Pope, A., Brodwin, M., et al. 2016, The Astrophysical Journal, 825, 72, doi: 10.3847/0004-637X/825/1/72

Allen, S. W., Evrard, A. E., & Mantz, A. B. 2011, ARA&A, 49, 409, doi: 10.1146/annurev-astro-081710-102514

Andersson, K., Benson, B. A., Ade, P. A. R., et al. 2011, ApJ, 738, 48, doi: 10.1088/0004-637X/738/1/48

Angulo, R. E., Springel, V., White, S. D. M., et al. 2012, MNRAS, 426, 2046, doi: 10.1111/j.1365-2966.2012.21830.x

Ashby, M. L. N., Stern, D., Brodwin, M., et al. 2009, ApJ,, 701, 428, doi: 10.1088/0004-637X/701/1/428

Austermann, J. E., Aird, K. A., Beall, J. A., et al. 2012, in Society of Photo-Optical Instrumentation Engineers (SPIE) Conference Series, Vol. 8452, Society of Photo-Optical Instrumentation Engineers (SPIE) Conference Series, doi: 10.1117/12.927286

Bai, L., Marcillac, D., Rieke, G. H., et al. 2007, ApJ, 664, 181, doi: 10.1086/518766

Barrena, R., Streblyanska, A., Ferragamo, A., et al. 2018, A&A, 616

Battaglia, N., Bond, J. R., Pfrommer, C., & Sievers, J. L. 2012, ApJ, 758, 75, doi: 10.1088/0004-637X/758/2/75

Battaglia, N., Leauthaud, A., Miyatake, H., et al. 2016, JCAP, 2016, 013, doi: 10.1088/1475-7516/2016/08/013

Baxter, E., Clampitt, J., Giannantonio, T., et al. 2016, MNRAS, 461, 4099, doi: 10.1093/mnras/stw1584

Baxter, E. J., Raghunathan, S., Crawford, T. M., et al. 2018, MNRAS, 476, 2674, doi: 10.1093/mnras/sty305

Bayliss, M. B., Hennawi, J. F., Gladders, M. D., et al. 2011, The Astrophysical Journal Supplement Series, 193, 8, doi: 10.1088/0067-0049/193/1/8

Bender, A. N., Kennedy, J., Ade, P. A. R., et al. 2016, MNRAS, 460, 3432, doi: 10.1093/mnras/stw1158

Benson, B. A., Ade, P. A. R., Ahmed, Z., et al. 2014, in Society of Photo-Optical Instrumentation Engineers (SPIE) Conference Series, Vol. 9153, Society of Photo-Optical Instrumentation Engineers (SPIE) Conference Series. https://arxiv.org/abs/1407.2973

Bertin, E., & Arnouts, S. 1996, A&AS, 117, 393

Bertin, E., Mellier, Y., Radovich, M., et al. 2002, in Astronomical Society of the Pacific Conference Series, Vol. 281, Astronomical Data Analysis Software and Systems XI, ed. D. A. Bohlender, D. Durand, & T. H. Handley, 228–+

Biesiadzinski, T., McMahon, J. J., Miller, C. J., Nord, B., & Shaw, L. 2012, ArXiv e-prints. https://arxiv.org/abs/1201.1282

Blake, C., Amon, A., Childress, M., et al. 2016, MNRAS, 462, 4240, doi: 10.1093/mnras/stw1990

Bleem, L. E., Stalder, B., Brodwin, M., et al. 2015a, ApJS, 216, 20, doi: 10.1088/0067-0049/216/1/20

Bleem, L. E., Stalder, B., de Haan, T., et al. 2015b, ApJS, 216, 27, doi: 10.1088/0067-0049/216/2/27

Bocquet, S., Dietrich, J. P., Schrabback, T., et al. 2019, ApJ, 878, 55, doi: 10.3847/1538-4357/ab1f10

Böhringer, H., Schuecker, P., Guzzo, L., et al. 2004, A&A, 425, 367, doi: 10.1051/0004-6361:20034484

Brodwin, M., Stanford, S. A., Gonzalez, A. H., et al. 2013, ApJ, 779, 138, doi: 10.1088/0004-637X/779/2/138

Bruzual, G., & Charlot, S. 2003, MNRAS, 344, 1000, doi: 10.1046/j.1365-8711.2003.06897.x

Burenin, R. A., Bikmaev, I. F., Khamitov, I. M., et al. 2018, Astronomy Letters, 44, 297, doi: 10.1134/S1063773718050018

Burgess, A. M., & Hunstead, R. W. 2006, AJ, 131, 114, doi: 10.1086/498679

Calabretta, M. R., & Greisen, E. W. 2002, A&A, 395, 1077, doi: 10.1051/0004-6361:20021327

Capasso, R., Mohr, J. J., Saro, A., et al. 2019, MNRAS, 486, 1594, doi: 10.1093/mnras/stz931

Carlstrom, J. E., Holder, G. P., & Reese, E. D. 2002, ARA&A, 40, 643

Carlstrom, J. E., Ade, P. A. R., Aird, K. A., et al. 2011, PASP, 123, 568, doi: 10.1086/659879

Cavagnolo, K., Donahue, M., Voit, G., & Sun, M. 2008, The Astrophysical Journal, 682, 821

Cavaliere, A., & Fusco-Femiano, R. 1976, A&A, 49, 137

Chambers, K. C., Magnier, E. A., Metcalfe, N., et al. 2016, arXiv e-prints, arXiv:1612.05560. https://arxiv.org/abs/1612.05560

Child, H. L., Habib, S., Heitmann, K., et al. 2018, ApJ, 859, 55, doi: 10.3847/1538-4357/aabf95

Chluba, J., Nagai, D., Sazonov, S., & Nelson, K. 2012, MNRAS, 426, 510, doi: 10.1111/j.1365-2966.2012.21741.x

Chon, G., & Böhringer, H. 2012, A&A, 538, A35, doi: 10.1051/0004-6361/201117996

CMB-S4 Collaboration, Abazajian, K., Addison, G., et al. 2019, arXiv e-prints, arXiv:1907.04473. https://arxiv.org/abs/1907.04473

Coble, K., Ade, P. A. R., Bock, J. J., et al. 2003, ArXiv Astrophysics e-prints

Coe, D., Salmon, B., Bradac, M., et al. 2019, arXiv e-prints, arXiv:1903.02002. https://arxiv.org/abs/1903.02002

Condon, J. J., Cotton, W. D., Greisen, E. W., et al. 1998, AJ, 115, 1693, doi: 10.1086/300337

Costanzi, M., Rozo, E., Simet, M., et al. 2018, arXiv e-prints, arXiv:1810.09456. https://arxiv.org/abs/1810.09456

Covone, G., Kneib, J.-P., Soucail, G., et al. 2006, A&A, 456, 409, doi: 10.1051/0004-6361:20053384

Crites, A. T., Henning, J. W., Ade, P. A. R., et al. 2015, ApJ, 805, 36, doi: 10.1088/0004-637X/805/1/36

Czakon, N. G., Sayers, J., Mantz, A., et al. 2015, ApJ, 806, 18, doi: 10.1088/0004-637X/806/1/18

Dalton, G. B., Maddox, S. J., Sutherland, W. J., & Efstathiou, G. 1997, MNRAS, 289, 263

Dark Energy Survey Collaboration, Abbott, T. M. C., Abdalla, F. B., et al. 2018, ArXiv e-prints. https://arxiv.org/abs/1801.03181

De Bernardis, F., Stevens, J. R., Hasselfield, M., et al. 2016, in Proc. SPIE, Vol. 9910, Observatory Operations: Strategies, Processes, and Systems VI, 991014, doi: 10.1117/12.2232824

de Haan, T., Benson, B. A., Bleem, L. E., et al. 2016, ApJ, 832, 95, doi: 10.3847/0004-637X/832/1/95

de Jong, J. T. A., Verdoes Kleijn, G. A., Kuijken, K. H., & Valentijn, E. A. 2013, Experimental Astronomy, 35, 25, doi: 10.1007/s10686-012-9306-1

de Propris, R., Stanford, S. A., Eisenhardt, P. R., Dickinson, M., & Elston, R. 1999, AJ, 118, 719, doi: 10.1086/300978

De Zotti, G., Ricci, R., Mesa, D., et al. 2005, A&A, 431, 893, doi: 10.1051/0004-6361:20042108

Diehl, H. T., Buckley-Geer, E. J., Lindgren, K. A., et al. 2017, The Astrophysical Journal Supplement Series, 232, 15, doi: 10.3847/1538-4365/aa8667

Dietrich, J. P., Bocquet, S., Schrabback, T., et al. 2019, MNRAS, 483, 2871, doi: 10.1093/mnras/sty3088

Dreyer, J. L. E. 1888, Memoirs of the Royal Astronomical Society, 49, 1

Eales, S., Dunne, L., Clements, D., et al. 2010, /pasp, 122, 499

Ebeling, H., Edge, A. C., Mantz, A., et al. 2010, MNRAS, 407, 83, doi: 10.1111/j.1365-2966.2010.16920.x

Ebeling, H., Qi, J., & Richard, J. 2017, MNRAS, 471, 3305, doi: 10.1093/mnras/stx1636

Ebeling, H., Stockmann, M., Richard, J., et al. 2018, ApJL, 852, L7, doi: 10.3847/2041-8213/aa9fee

Edge, A., Sutherland, W., Kuijken, K., et al. 2013, The Messenger, 154, 32

Eisenhardt, P. R. M., Brodwin, M., Gonzalez, A. H., et al. 2008, ApJ, 684, 905, doi: 10.1086/590105

Erler, J., Basu, K., Chluba, J., & Bertoldi, F. 2018, MNRAS, 476, 3360, doi: 10.1093/mnras/sty327

Euclid Collaboration, Adam, R., Vannier, M., et al. 2019, Astronomy and Astrophysics, 627, A23, doi: 10.1051/0004-6361/201935088

Farahi, A., Evrard, A. E., Rozo, E., Rykoff, E. S., & Wechsler, R. H. 2016, MNRAS, 460, 3900, doi: 10.1093/mnras/stw1143

Fazio, G. G., Hora, J. L., Allen, L. E., et al. 2004, ApJS, 154, 10, doi: 10.1086/422843

Fixsen, D. J. 2009, ApJ, 707, 916, doi: 10.1088/0004-637X/707/2/916

Flaugher, B., Diehl, H. T., Honscheid, K., et al. 2015, AJ, 150, 150, doi: 10.1088/0004-6256/150/5/150

Flender, S., Bleem, L., Finkel, H., et al. 2016, ApJ, 823, 98, doi: 10.3847/0004-637X/823/2/98

Flewelling, H. A., Magnier, E. A., Chambers, K. C., et al. 2016, arXiv e-prints, arXiv:1612.05243. https://arxiv.org/abs/1612.05243

Foreman-Mackey, D., Hogg, D. W., Lang, D., & Goodman, J. 2013, PASP, 125, 306, doi: 10.1086/670067

Gaia Collaboration, Brown, A. G. A., Vallenari, A., et al. 2018, ArXiv e-prints. https://arxiv.org/abs/1804.09365

Garg, A., Stubbs, C. W., Challis, P., et al. 2007, AJ, 133, 403, doi: 10.1086/510118

Geach, J. E., & Peacock, J. A. 2017, Nature Astronomy, 1, 795, doi: 10.1038/s41550-017-0259-1

George, E. M., Ade, P., Aird, K. A., et al. 2012, in Society of Photo-Optical Instrumentation Engineers (SPIE) Conference Series, Vol. 8452, Society of Photo-Optical Instrumentation Engineers (SPIE) Conference Series, doi: 10.1117/12.925586

George, E. M., Reichardt, C. L., Aird, K. A., et al. 2015, ApJ, 799, 177, doi: 10.1088/0004-637X/799/2/177

Gioia, I. M., Maccacaro, T., Schild, R. E., et al. 1990, ApJS, 72, 567, doi: 10.1086/191426

Gonzalez, A. H., Gettings, D. P., Brodwin, M., et al. 2019, The Astrophysical Journal Supplement Series, 240, 33, doi: 10.3847/1538-4365/aafad2

Gralla, M. B., Gladders, M. D., Yee, H. K. C., & Barrientos, L. F. 2011, ApJ, 734, 103, doi: 10.1088/0004-637X/734/2/103

Gralla, M. B., Crichton, D., Marriage, T. A., et al. 2014, MNRAS, 445, 460, doi: 10.1093/mnras/stu1592

Gralla, M. B., Marriage, T. A., Addison, G., et al. 2019, arXiv e-prints

Gruen, D., Seitz, S., Brimioulle, F., et al. 2014, MNRAS, 442, 1507, doi: 10.1093/mnras/stu949

Gupta, N., Saro, A., Mohr, J. J., et al. 2017, MNRAS, doi: 10.1093/mnras/stx095

Habib, S., Heitmann, K., Higdon, D., Nakhleh, C., & Williams, B. 2007, PhRvD, 76, 083503, doi: 10.1103/PhysRevD.76.083503

Habib, S., Pope, A., Finkel, H., et al. 2016, NewA, 42, 49, doi: 10.1016/j.newast.2015.06.003

Hamilton-Morris, V., Smith, G. P., Edge, A. C., et al. 2012, ApJL, 748, L23, doi: 10.1088/2041-8205/748/2/L23

Hasselfield, M., Hilton, M., Marriage, T. A., et al. 2013, JCAP, 7, 8, doi: 10.1088/1475-7516/2013/07/008

Heitmann, K., Higdon, D., Nakhleh, C., & Habib, S. 2006, ApJL, 646, L1, doi: 10.1086/506448

Heitmann, K., Bingham, D., Lawrence, E., et al. 2016, ApJ, 820, 108, doi: 10.3847/0004-637X/820/2/108

Heitmann, K., Finkel, H., Pope, A., et al. 2019, arXiv e-prints, arXiv:1904.11970. https://arxiv.org/abs/1904.11970

Henderson, S. W., Allison, R., Austermann, J., et al. 2016, Journal of Low Temperature Physics, 184, 772, doi: 10.1007/s10909-016-1575-z

Henning, J. W., Sayre, J. T., Reichardt, C. L., et al. 2018, ApJ, 852, 97, doi: 10.3847/1538-4357/aa9ff4

High, F. W., Stubbs, C. W., Rest, A., Stalder, B., & Challis, P. 2009, AJ, 138, 110, doi: 10.1088/0004-6256/138/1/110

Hilton, M., Hasselfield, M., Sifón, C., et al. 2018, ApJS, 235, 20, doi: 10.3847/1538-4365/aaa6cb

Hoekstra, H., Herbonnet, R., Muzzin, A., et al. 2015, MNRAS, 449, 685, doi: 10.1093/mnras/stv275
Hollowood, D. L., Jeltema, T., Chen, X., et al. 2018, arXiv e-prints, arXiv:1808.06637. https://arxiv.org/abs/1808.06637
Hou, Z., Aylor, K., Benson, B. A., et al. 2018, ApJ, 853, 3, doi: 10.3847/1538-4357/aaa3ef
Huang, N., Bleem, L. E., Stalder, B., et al. 2019, arXiv e-prints, arXiv:1907.09621. https://arxiv.org/abs/1907.09621
Itoh, N., & Nozawa, S. 2004, A&A, 417, 827, doi: 10.1051/0004-6361:20034236
Jacobs, C., Collett, T., Glazebrook, K., et al. 2019, ApJS, 243, 17, doi: 10.3847/1538-4365/ab26b6
Jimeno, P., Diego, J. M., Broadhurst, T., De Martino, I., & Lazkoz, R. 2018, MNRAS, 478, 638, doi: 10.1093/mnras/sty987
Johnson, A., Blake, C., Amon, A., et al. 2017, MNRAS, 465, 4118, doi: 10.1093/mnras/stw3033
Johnston, D. E., Sheldon, E. S., Wechsler, R. H., et al. 2007, ArXiv e-prints. https://arxiv.org/abs/0709.1159
Joudaki, S., Blake, C., Johnson, A., et al. 2018, MNRAS, 474, 4894, doi: 10.1093/mnras/stx2820
Keisler, R., Reichardt, C. L., Aird, K. A., et al. 2011, ApJ, 743, 28, doi: 10.1088/0004-637X/743/1/28
Kelly, B. C. 2007, ApJ, 665, 1489, doi: 10.1086/519947
Khullar, G., Bleem, L. E., Bayliss, M. B., et al. 2019, ApJ, 870, 7, doi: 10.3847/1538-4357/aaeed0
Klein, M., Grandis, S., Mohr, J. J., et al. 2019, MNRAS, 488, 739, doi: 10.1093/mnras/stz1463
Kneib, J.-P., & Natarajan, P. 2011, Astronomy and Astrophysics Review, 19, 47, doi: 10.1007/s00159-011-0047-3
Koester, B. P., McKay, T. A., Annis, J., et al. 2007, ApJ, 660, 221, doi: 10.1086/512092
Kravtsov, A. V., & Borgani, S. 2012, ARA&A, 50, 353, doi: 10.1146/annurev-astro-081811-125502
Lin, Y., Partridge, B., Pober, J. C., et al. 2009, ApJ, 694, 992, doi: 10.1088/0004-637X/694/2/992
Lin, Y.-T., & Mohr, J. J. 2004, ApJ, 617, 879, doi: 10.1086/425412
Liu, J., Hennig, C., Desai, S., et al. 2015a, MNRAS, 449, 3370, doi: 10.1093/mnras/stv458
Liu, T., Tozzi, P., Tundo, E., et al. 2015b, ApJS, 216, 28, doi: 10.1088/0067-0049/216/2/28
Lotz, J. M., Koekemoer, A., Coe, D., et al. 2017, ApJ, 837, 97, doi: 10.3847/1538-4357/837/1/97
LSST Science Collaboration, Abell, P. A., Allison, J., et al. 2009, arXiv e-prints, arXiv:0912.0201. https://arxiv.org/abs/0912.0201
Mainzer, A., Bauer, J., Cutri, R. M., et al. 2014, ApJ, 792, 30, doi: 10.1088/0004-637X/792/1/30
Mann, A. W., & Ebeling, H. 2012, MNRAS, 420, 2120, doi: 10.1111/j.1365-2966.2011.20170.x
Mantz, A., Allen, S. W., Rapetti, D., & Ebeling, H. 2010, MNRAS, 406, 1759, doi: 10.1111/j.1365-2966.2010.16992.x
Mantz, A. B., von der Linden, A., Allen, S. W., et al. 2015, MNRAS, 446, 2205, doi: 10.1093/mnras/stu2096
Mantz, A. B., Allen, S. W., Morris, R. G., et al. 2016, MNRAS, 463, 3582, doi: 10.1093/mnras/stw2250
Maturi, M., Bellagamba, F., Radovich, M., et al. 2019, MNRAS, 485, 498, doi: 10.1093/mnras/stz294
McClintock, T., Varga, T. N., Gruen, D., et al. 2019, MNRAS, 482, 1352, doi: 10.1093/mnras/sty2711
McDonald, M., Allen, S. W., Bayliss, M., et al. 2017, ApJ, 843, 28, doi: 10.3847/1538-4357/aa7740
Medezinski, E., Battaglia, N., Umetsu, K., et al. 2018, PASJ, 70, S28, doi: 10.1093/pasj/psx128
Mehrtens, N., Romer, A. K., Hilton, M., et al. 2012, MNRAS, 423, 1024, doi: 10.1111/j.1365-2966.2012.20931.x
Meisner, A. M., Lang, D., & Schlegel, D. J. 2017, AJ, 154, 161, doi: 10.3847/1538-3881/aa894e
Melin, J.-B., Bartlett, J. G., Cai, Z.-Y., et al. 2018, A&A, 617, A75, doi: 10.1051/0004-6361/201732292
Melin, J.-B., Bartlett, J. G., & Delabrouille, J. 2006, A&A, 459, 341, doi: 10.1051/0004-6361:20065034
Meneghetti, M., Bartelmann, M., Dahle, H., & Limousin, M. 2013, SSRv, 177, 31, doi: 10.1007/s11214-013-9981-x
Merloni, A., Predehl, P., Becker, W., et al. 2012, arXiv e-prints, arXiv:1209.3114. https://arxiv.org/abs/1209.3114
Miknaitis, G., Pignata, G., Rest, A., et al. 2007, ApJ, 666, 674, doi: 10.1086/519986
Mocanu, L. M., Crawford, T. M., Vieira, J. D., et al. 2013, ApJ, 779, 61, doi: 10.1088/0004-637X/779/1/61
Motl, P. M., Hallman, E. J., Burns, J. O., & Norman, M. L. 2005, ApJL, 623, L63, doi: 10.1086/430144
Murata, R., Nishimichi, T., Takada, M., et al. 2018, ApJ, 854, 120, doi: 10.3847/1538-4357/aaaab8
Murata, R., Oguri, M., Nishimichi, T., et al. 2019, arXiv e-prints, arXiv:1904.07524. https://arxiv.org/abs/1904.07524
Murphy, T., Sadler, E. M., Ekers, R. D., et al. 2010, MNRAS, 402, 2403, doi: 10.1111/j.1365-2966.2009.15961.x
Muzzin, A., Wilson, G., Demarco, R., et al. 2013, ApJ, 767, 39, doi: 10.1088/0004-637X/767/1/39

Navarro, J. F., Frenk, C. S., & White, S. D. M. 1996, ApJ, 462, 563, doi: 10.1086/177173

Newman, A. B., Belli, S., Ellis, R. S., & Patel, S. G. 2018, ApJ, 862, 125, doi: 10.3847/1538-4357/aacd4d

Nozawa, S., Itoh, N., Kawana, Y., & Kohyama, Y. 2000, ApJ, 536, 31, doi: 10.1086/308938

Nurgaliev, D., McDonald, M., Benson, B. A., et al. 2013, ApJ, 779, 112, doi: 10.1088/0004-637X/779/2/112

—. 2017, ApJ, 841, 5, doi: 10.3847/1538-4357/aa6db4

Oguri, M., Lin, Y.-T., Lin, S.-C., et al. 2018, PASJ, 70, S20, doi: 10.1093/pasj/psx042

Oke, J. B. 1974, ApJS, 27, 21, doi: 10.1086/190287

Persson, S. E., Murphy, D. C., Smee, S., et al. 2013, PASP, 125, 654, doi: 10.1086/671164

Petrillo, C. E., Tortora, C., Vernardos, G., et al. 2019, MNRAS, 484, 3879, doi: 10.1093/mnras/stz189

Piffaretti, R., Arnaud, M., Pratt, G. W., Pointecouteau, E., & Melin, J.-B. 2011, A&A, 534, A109, doi: 10.1051/0004-6361/201015377

Planck Collaboration, Aghanim, N., Arnaud, M., et al. 2011, A&A, 536, A12, doi: 10.1051/0004-6361/201116489

—. 2012, A&A, 543, A102, doi: 10.1051/0004-6361/201118731

Planck Collaboration, Ade, P. A. R., Aghanim, N., et al. 2013, A&A, 550, A130, doi: 10.1051/0004-6361/201219519

Planck Collaboration, Adam, R., Ade, P. A. R., et al. 2015, ArXiv e-prints. https://arxiv.org/abs/1502.01582

Planck Collaboration, Ade, P. A. R., Aghanim, N., et al. 2016a, A&A, 594, A27, doi: 10.1051/0004-6361/201525823

—. 2016b, A&A, 594, A24, doi: 10.1051/0004-6361/201525833

Planck Collaboration, Adam, R., Ade, P. A. R., et al. 2016c, A&A, 594, A8, doi: 10.1051/0004-6361/201525820

Planck Collaboration, Akrami, Y., Argüeso, F., et al. 2018, A&A, 619, A94, doi: 10.1051/0004-6361/201832888

Predehl, P., Andritschke, R., Böhringer, H., et al. 2010, in Society of Photo-Optical Instrumentation Engineers (SPIE) Conference Series, Vol. 7732, Society of Photo-Optical Instrumentation Engineers (SPIE) Conference Series, doi: 10.1117/12.856577

Raghunathan, S., Patil, S., Baxter, E., et al. 2019, ApJ, 872, 170, doi: 10.3847/1538-4357/ab01ca

Rasmussen, C. E., & Williams, C. 2006, Gaussian Processes for Machine Learning (MIT Press). http://www.gaussianprocess.org/gpml/

Reichardt, C. L., Stalder, B., Bleem, L. E., et al. 2013, ApJ, 763, 127, doi: 10.1088/0004-637X/763/2/127

Repp, A., & Ebeling, H. 2018, MNRAS, 479, 844, doi: 10.1093/mnras/sty1489

Rest, A., Stubbs, C., Becker, A. C., et al. 2005, ApJ, 634, 1103, doi: 10.1086/497060

Rossetti, M., Gastaldello, F., Ferioli, G., et al. 2016, MNRAS, 457, 4515, doi: 10.1093/mnras/stw265

Rozo, E., Bartlett, J. G., Evrard, A. E., & Rykoff, E. S. 2014, MNRAS, 438, 78, doi: 10.1093/mnras/stt2161

Rozo, E., & Rykoff, E. S. 2014, ApJ, 783, 80, doi: 10.1088/0004-637X/783/2/80

Rozo, E., Rykoff, E. S., Bartlett, J. G., & Melin, J.-B. 2015, MNRAS, 450, 592, doi: 10.1093/mnras/stv605

Rykoff, E. S., Rozo, E., Busha, M. T., et al. 2014, ApJ, 785, 104, doi: 10.1088/0004-637X/785/2/104

Rykoff, E. S., Rozo, E., Hollowood, D., et al. 2016, The Astrophysical Journal Supplement Series, 224, 1, doi: 10.3847/0067-0049/224/1/1

Sand, D. J., Treu, T., Ellis, R. S., & Smith, G. P. 2005, ApJ, 627, 32, doi: 10.1086/430298

Sanderson, A. J. R., Edge, A. C., & Smith, G. P. 2009, MNRAS, 398, 1698, doi: 10.1111/j.1365-2966.2009.15214.x

Saro, A., Bocquet, S., Rozo, E., et al. 2015, MNRAS, 454, 2305, doi: 10.1093/mnras/stv2141

Saro, A., Bocquet, S., Mohr, J., et al. 2017, MNRAS, 468, 3347, doi: 10.1093/mnras/stx594

Schaffer, K. K., Crawford, T. M., Aird, K. A., et al. 2011, ApJ, 743, 90, doi: 10.1088/0004-637X/743/1/90

Schellenberger, G., & Reiprich, T. H. 2017, MNRAS, 469, 3738, doi: 10.1093/mnras/stx1022

Schlafly, E. F., Meisner, A. M., & Green, G. M. 2019, The Astrophysical Journal Supplement Series, 240, 30, doi: 10.3847/1538-4365/aafbea

Schlegel, D. J., Finkbeiner, D. P., & Davis, M. 1998, ApJ, 500, 525

Schwartz, D. A., Bradt, H. V., Remillard, R. A., & Tuohy, I. R. 1991, ApJ, 376, 424, doi: 10.1086/170291

Sehgal, N., Addison, G., Battaglia, N., et al. 2013, ApJ, 767, 38, doi: 10.1088/0004-637X/767/1/38

Sharon, K., Bayliss, M. B., Dahle, H., et al. 2019, arXiv e-prints, arXiv:1904.05940. https://arxiv.org/abs/1904.05940

Simet, M., McClintock, T., Mandelbaum, R., et al. 2017, MNRAS, 466, 3103, doi: 10.1093/mnras/stw3250

Simons Observatory Collaboration, Ade, P., Aguirre, J., et al. 2019, Journal of Cosmology and Astro-Particle Physics, 2019, 056, doi: 10.1088/1475-7516/2019/02/056

Skrutskie, M. F., Cutri, R. M., Stiening, R., et al. 2006, AJ, 131, 1163, doi: 10.1086/498708

Smail, I., Ellis, R. S., Fitchett, M. J., et al. 1991, MNRAS, 252, 19, doi: 10.1093/mnras/252.1.19

Smith, G. P., Mazzotta, P., Okabe, N., et al. 2016, MNRAS, 456, L74, doi: 10.1093/mnrasl/slv175

Soergel, B., Giannantonio, T., Efstathiou, G., Puchwein, E., & Sijacki, D. 2017, MNRAS, 468, 577, doi: 10.1093/mnras/stx492

Song, J., Zenteno, A., Stalder, B., et al. 2012, ApJ, 761, 22, doi: 10.1088/0004-637X/761/1/22

Spergel, D., Gehrels, N., Baltay, C., et al. 2015, arXiv e-prints, arXiv:1503.03757. https://arxiv.org/abs/1503.03757

Stalder, B., Stark, A. A., Amato, S. M., et al. 2014, in Proc. SPIE, Vol. 9147, Ground-based and Airborne Instrumentation for Astronomy V, 91473Y, doi: 10.1117/12.2054933

Staniszewski, Z., Ade, P. A. R., Aird, K. A., et al. 2009, ApJ, 701, 32, doi: 10.1088/0004-637X/701/1/32

Story, K., Aird, K. A., Andersson, K., et al. 2011, ApJL, 735, L36+, doi: 10.1088/2041-8205/735/2/L36

Sunyaev, R., & Zel'dovich, Y. 1980, ARAA, 18, 537, doi: 10.1146/annurev.aa.18.090180.002541

Sunyaev, R. A., & Zel'dovich, Y. B. 1972, Comments on Astrophysics and Space Physics, 4, 173

Tinker, J., Kravtsov, A. V., Klypin, A., et al. 2008, ApJ, 688, 709, doi: 10.1086/591439

Tody, D. 1993, in Astronomical Society of the Pacific Conference Series, Vol. 52, Astronomical Data Analysis Software and Systems II, ed. R. J. Hanisch, R. J. V. Brissenden, & J. Barnes, 173

Vanderlinde, K., Crawford, T. M., de Haan, T., et al. 2010, ApJ, 722, 1180, doi: 10.1088/0004-637X/722/2/1180

Vikhlinin, A., Kravtsov, A. V., Burenin, R. A., et al. 2009, ApJ, 692, 1060, doi: 10.1088/0004-637X/692/2/1060

Voit, G. M. 2005, Reviews of Modern Physics, 77, 207, doi: 10.1103/RevModPhys.77.207

von der Linden, A., Mantz, A., Allen, S. W., et al. 2014, MNRAS, 443, 1973, doi: 10.1093/mnras/stu1423

Weinberg, D. H., Mortonson, M. J., Eisenstein, D. J., et al. 2013, PhR, 530, 87, doi: 10.1016/j.physrep.2013.05.001

Wen, Z. L., Han, J. L., & Liu, F. S. 2012, ApJS, 199, 34, doi: 10.1088/0067-0049/199/2/34

Wen, Z. L., Han, J. L., & Yang, F. 2018, MNRAS, 475, 343, doi: 10.1093/mnras/stx3189

Wright, E. L. 1979, ApJ, 232, 348. http://adsabs.harvard.edu/cgi-bin/nph-bib_query?bibcode=1979ApJ...232..348W&db_key=AST

Wright, E. L., Eisenhardt, P. R. M., Mainzer, A. K., et al. 2010, AJ, 140, 1868, doi: 10.1088/0004-6256/140/6/1868

Zhang, Y., Jeltema, T., Hollowood, D. L., et al. 2019, MNRAS, doi: 10.1093/mnras/stz1361

Zitrin, A., Broadhurst, T., Barkana, R., Rephaeli, Y., & Benítez, N. 2011, MNRAS, 410, 1939, doi: 10.1111/j.1365-2966.2010.17574.x

APPENDIX

A. OFFSET DISTRIBUTION EMULATOR CONSTRUCTION

In this section we describe the construction of our emulator of the SZ - RM central galaxy offset distribution discussed in Section 6.2.2. This distribution is modeled as the SPT positional uncertainty (see Eq'n 21) convolved with:

$$P(x) = \rho \frac{1}{\sigma_\lambda} e^{-\frac{x}{\sigma_\lambda}} + (1-\rho)\frac{x}{\tau^2} e^{-\frac{x}{\tau}} \tag{A1}$$

where $x = r_{\rm offset}/R_\lambda$, σ_λ characterizes the exponential distribution, and τ is the scale parameter of the Gamma distribution function. The training probability distributions $p(x,\theta)$ are generated at $N = 1024$ points on a latin hypercube sampling (LHS) design of the 3 centering model parameters as well as the SPT positional uncertainty scaled by the RM size (converted to radians) $\theta = \{\rho, \sigma_\lambda, \tau, \sigma_{SPT}/\theta_\lambda\}$. As shown in Cosmic Emulators (Heitmann et al. 2016), the space-filling properties of LHS are well-suited for GP interpolation on a relatively small number of training points. The range of our centering model parameters are identical to the flat priors in our likelihood analysis and the SPT positional uncertainty trained over the range $0.0 \leq \sigma_{SPT}/\theta_\lambda \leq 1.0$.

Our emulation strategy also follows that of the Cosmic Emulators. That is, we first perform a singular value decomposition of probability $p(x,\theta)$ values in 100 bins (spanning separations from 0 to R_λ). Weights of 16 truncated orthogonal bases are then modeled as independent functions of input parameters $\{\rho, \sigma_\lambda, \tau, \sigma_{SPT}/R_\lambda\}$ using GP as a local interpolating scheme. The key ingredient of *learning* in GP modeling is the configuration of the covariance function and determination of the associated hyperparameters, which we find using Bayesian optimization. We also check the robustness of the emulator accuracy with different choices of covariance functions.

The fully trained emulator is validated on the parameter values within the limits of the latin hypercube, but not at the specific points where the emulator is fitted. The evaluation time for the trained emulator is less than 0.001 seconds per computation, delivering a speed-up of 1000 over numerical calculation of $p(x,\theta)$. This is crucial for quick explorations of the posterior distribution of parameters, where our GP emulator is implemented in the MCMC likelihood calculation.

B. ASSOCIATIONS WITH LRGS FROM THE 2DFLENS SURVEY

SPT clusters, redshift estimates, and associated LRG spectroscopic redshifts for clusters associated with LRGs in the 2dFLenS Survey (see Section 4.2.3). SPT-CL J0302−3306 and SPT-CL J0319−2853 were targeted in a spare fiber program. The full 2dFLenS redshift catalog is available at http://2dflens.swin.edu.au/.

Table 7. Associations with 2dFLenS LRGs

SPT ID	z	2dFLenS z(s)	Offset (arcmin)
SPT−CL J0000−2805	0.23 ± 0.03	0.283	0.64
SPT−CL J0014−3022	0.307	0.308, 0.317	1.04, 1.68
SPT−CL J0036−3144	0.41 ± 0.01	0.413	0.18
SPT−CL J0042−2831	0.109	0.110, 0.109	1.16, 2.46
SPT−CL J0100−3246	0.53 ± 0.01	0.532	1.76
SPT−CL J0114−2820	0.43 ± 0.01	0.441, 0.447	1.03, 1.22
SPT−CL J0115−2917	0.41 ± 0.01	0.397	1.27
SPT−CL J0121−3355	0.57 ± 0.01	0.579	1.28
SPT−CL J0152−2853	0.413	0.416, 0.406	0.25, 0.85
SPT−CL J0158−2910	0.57 ± 0.01	0.576	2.11
SPT−CL J0159−3010	0.69 ± 0.01	0.699, 0.703	1.21, 1.57
SPT−CL J0159−3331	0.40 ± 0.01	0.411, 0.406	0.42, 2.31
SPT−CL J0202−2812	0.12 ± 0.01	0.111	2.32
SPT−CL J0202−3027	0.48 ± 0.01	0.489, 0.493	0.27, 1.52
SPT−CL J0206−2921	0.28 ± 0.01	0.273	1.60
SPT−CL J0215−2948	0.25 ± 0.01	0.256	2.36
SPT−CL J0217−3200	0.35 ± 0.01	0.341	0.26
SPT−CL J0218−3142	0.27 ± 0.01	0.275, 0.269, 0.267	0.19, 0.74, 1.68
SPT−CL J0224−3223	0.54 ± 0.01	0.545, 0.545	1.36, 1.86
SPT−CL J0241−2839	0.238	0.226, 0.237	0.89, 2.45
SPT−CL J0242−3123	0.50 ± 0.01	0.491	1.01
SPT−CL J0302−3209	0.32 ± 0.01	0.327, 0.325	0.18, 1.67
SPT−CL J0302−3306	0.73 ± 0.01	0.752	0.66
SPT−CL J0303−2736	0.27 ± 0.01	0.261	0.73
SPT−CL J0305−3229	0.53 ± 0.01	0.529	0.33
SPT−CL J0307−2840	0.253	0.250	0.45
SPT−CL J0309−3209	0.54 ± 0.01	0.526	2.35
SPT−CL J0319−2853	0.36 ± 0.01	0.355	0.04
SPT−CL J0319−3345	0.41 ± 0.01	0.411	0.46
SPT−CL J2159−2846	0.43 ± 0.04	0.423, 0.431	0.89, 2.19
SPT−CL J2220−3509	0.154	0.152	1.55
SPT−CL J2234−3033	0.251	0.246	0.73
SPT−CL J2234−3159	0.57 ± 0.04	0.557	0.46
SPT−CL J2251−3324	0.24 ± 0.02	0.230, 0.231	0.43, 1.00
SPT−CL J2253−3344	0.224	0.228	0.07
SPT−CL J2258−3447	0.317	0.307, 0.308	0.64, 0.97
SPT−CL J2321−2725	0.67 ± 0.04	0.658	0.92
SPT−CL J2335−3256	0.51 ± 0.04	0.490, 0.511	1.91, 2.16
SPT−CL J2336−3205	0.63 ± 0.04	0.619, 0.613, 0.623	0.27, 1.52, 2.43

Note—For each cluster we report the cluster name, spectroscopic (3 digits) or photometric (2 digits with uncertainty) redshift, the spectroscopic redshifts of the 2dFLenS LRGS, and the spatial separation of these LRGs from the SPT cluster location.

C. THE CLUSTER CATALOGS

In this section we provide three different tables: the complete cluster candidate list at $\xi > 5$ from SPT-ECS, the confirmed sample from SPT-ECS at $4 < \xi < 5$, and, finally, newly-confirmed clusters at $\xi > 4.5$ from the 2500d SPT-SZ survey (Bleem et al. 2015b). The SPT-SZ clusters were confirmed using our RM association process described in Section 4.2.1. The data from these tables, including references for the sources of spectroscopic redshifts, photometric redshifts(when taken from the literature), and strong lensing information (where previously known), as well as additional notes on individual clusters are available online at http://pole.uchicago.edu/public/data/sptsz-clusters.

Table 8. Galaxy cluster candidates above $\xi = 5$ in the SPTpol Extended Cluster Survey.

SPT ID	R.A.	Decl.	Best		Redshift	M_{500c}	λ	Image Source	Notes
	(J2000)	(J2000)	ξ	θ_c		$(10^{14} h_{70}^{-1} M_\odot)$			
SPT-CL J0000−2518	0.0723	−25.3039	5.07	1.50	-	-	-	1	-
SPT-CL J0005−3751	1.4383	−37.8544	6.34	0.75	0.483±0.007	$5.42^{+0.89}_{-0.89}$	86±5	3	SL
SPT-CL J0005−3443	1.4877	−34.7193	5.51	2.00	0.114	$5.32^{+0.90}_{-1.00}$	105±5	8	-
SPT-CL J0012−3537	3.0433	−35.6226	5.26	2.25	0.69±0.02	$4.38^{+0.80}_{-0.89}$	73±5	3	-
SPT-CL J0012−3346	3.1112	−33.7782	6.70	1.00	0.68±0.01	$5.37^{+0.82}_{-0.85}$	101±6	3	-
SPT-CL J0014−3022	3.5727	−30.3831	18.29	1.50	0.307	$11.39^{+1.15}_{-1.38}$	-	8	SL
SPT-CL J0014−2024	3.6932	−20.4087	5.64	1.00	0.317	$5.62^{+0.98}_{-0.98}$	-	8	-
SPT-CL J0020−2543	5.1731	−25.7276	7.14	1.50	0.141	$7.04^{+0.97}_{-1.08}$	101±18	8	-
SPT-CL J0028−2649	7.0111	−26.8205	7.03	0.50	0.75±0.01	$5.93^{+0.84}_{-0.95}$	77±5	3	-
SPT-CL J0035−2015	8.8608	−20.2635	8.40	1.25	0.352	$7.48^{+0.95}_{-1.08}$	-	8	-
SPT-CL J0042−2831	10.5269	−28.5221	8.12	1.75	0.109	$7.76^{+0.96}_{-1.10}$	71±3	8	-
SPT-CL J0042−3809	10.6133	−38.1513	6.62	1.25	0.220	$6.01^{+0.87}_{-0.98}$	75±3	8	-
SPT-CL J0043−2037	10.8452	−20.6226	8.87	1.75	0.292	$7.86^{+0.96}_{-1.10}$	202±35	8	SL
SPT-CL J0046−3911	11.6056	−39.1997	9.17	0.75	0.594±0.007	$6.88^{+0.78}_{-0.94}$	98±4	3	-
SPT-CL J0049−2440	12.2935	−24.6812	7.44	0.50	0.527±0.006	$6.59^{+0.86}_{-0.98}$	111±6	3	SL
SPT-CL J0055−3739	13.8270	−37.6617	5.06	1.50	-	-	-	3	-
SPT-CL J0059−3137	14.8774	−31.6319	5.20	0.75	-	-	-	4	-
SPT-CL J0101−3109	15.2898	−31.1514	5.19	0.25	-	-	-	3	-
SPT-CL J0101−3840	15.4195	−38.6686	6.01	0.50	0.258±0.005	$5.50^{+0.95}_{-0.94}$	54±3	3	-
SPT-CL J0105−2439	16.3904	−24.6541	10.12	2.00	0.229±0.004	$8.70^{+1.02}_{-1.19}$	123±9	3	-
SPT-CL J0105−3004	16.4319	−30.0679	5.01	1.50	-	-	-	3	-
SPT-CL J0114−2820	18.6753	−28.3418	7.07	0.50	0.431±0.010	$6.52^{+0.88}_{-1.00}$	121±4	3	-
SPT-CL J0118−2658	19.5376	−26.9708	6.05	1.50	0.228	$6.11^{+0.94}_{-1.05}$	100±6	8	-
SPT-CL J0140−3410	25.0255	−34.1756	6.77	0.50	0.40±0.01	$5.84^{+0.84}_{-0.95}$	56±3	3	-
SPT-CL J0151−2859	27.9042	−28.9969	7.28	0.25	0.392±0.010	$6.72^{+0.89}_{-1.04}$	140±5	3	-
SPT-CL J0152−2853	28.1411	−28.8902	7.58	0.50	0.413	$6.87^{+0.91}_{-1.02}$	125±4	8	-
SPT-CL J0152−3524	28.2416	−35.4099	6.16	1.00	0.94±0.02	$4.66^{+0.72}_{-0.83}$	64±5	3	-
SPT-CL J0159−3413	29.7554	−34.2247	13.83	1.50	0.413	$9.34^{+0.96}_{-1.17}$	136±5	8	SL
SPT-CL J0159−3331	29.8398	−33.5270	8.19	1.00	0.40±0.01	$5.73^{+0.70}_{-0.85}$	90±15	3	-
SPT-CL J0200−2454	30.0694	−24.9146	10.29	1.00	0.72±0.01	$6.66^{+0.77}_{-0.90}$	142±5	3	-
SPT-CL J0200−3106	30.1966	−31.1155	6.92	0.75	0.99±0.03	$4.29^{+0.64}_{-0.70}$	71±6	3	-
SPT-CL J0201−2325	30.4709	−23.4225	5.12	0.25	-	-	-	3	-
SPT-CL J0202−3027	30.5419	−30.4638	6.46	0.75	0.484±0.007	$4.71^{+0.70}_{-0.80}$	92±4	3	-
SPT-CL J0203−2017	30.7887	−20.2867	9.24	0.25	0.440±0.009	$6.69^{+0.81}_{-0.92}$	126±4	3	SL
SPT-CL J0204−2904	31.1517	−29.0689	5.17	0.50	-	-	-	3	-

Table 8 *continued*

Table 8 *(continued)*

SPT ID	R.A.	Decl.	Best		Redshift	M_{500c}	λ	Image Source	Notes
	(J2000)	(J2000)	ξ	θ_c		$(10^{14} h_{70}^{-1} M_\odot)$			
SPT-CL J0205−2834	31.3411	−28.5798	7.61	0.75	0.88±0.05	$5.21^{+0.70}_{-0.79}$	-	3	-
SPT-CL J0206−3424	31.5142	−34.4132	5.85	0.25	0.63±0.01	$4.16^{+0.72}_{-0.73}$	56±4	3	-
SPT-CL J0214−2724	33.5159	−27.4038	5.25	0.25	0.81±0.01	$3.91^{+0.77}_{-0.80}$	48±4	3	-
SPT-CL J0216−2609	34.1486	−26.1605	6.43	0.25	0.79±0.01	$4.70^{+0.72}_{-0.80}$	58±5	3	SL
SPT-CL J0217−2749	34.3729	−27.8274	6.26	0.75	1.00±0.03	$4.31^{+0.67}_{-0.77}$	35±6	3	-
SPT-CL J0217−3200	34.3841	−32.0063	5.14	0.50	0.354±0.009	$4.05^{+0.72}_{-0.83}$	49±3	3	-
SPT-CL J0218−3142	34.5786	−31.7054	8.66	0.75	0.275±0.005	$6.15^{+0.71}_{-0.88}$	125±4	3	-
SPT-CL J0219−3208	34.9423	−32.1435	5.28	0.25	0.607±0.009	$3.85^{+0.70}_{-0.79}$	83±12	3	-
SPT-CL J0220−2825	35.0214	−28.4171	5.14	0.75	-	-	-	3	-
SPT-CL J0224−3921	36.0033	−39.3594	7.05	0.50	0.491±0.008	$5.02^{+0.72}_{-0.79}$	39±3	3	-
SPT-CL J0236−3901	39.0172	−39.0308	5.38	0.25	0.94±0.02	$3.53^{+0.67}_{-0.70}$	48±6	3	-
SPT-CL J0237−2807	39.3258	−28.1169	5.94	0.75	0.500±0.007	$4.77^{+0.82}_{-0.81}$	92±4	3	-
SPT-CL J0237−3743	39.4114	−37.7223	5.09	0.25	0.511±0.007	$3.83^{+0.70}_{-0.81}$	79±3	3	-
SPT-CL J0238−2615	39.5807	−26.2625	5.15	2.00	0.446±0.009	$4.32^{+0.77}_{-0.88}$	62±4	3	-
SPT-CL J0238−3416	39.6816	−34.2726	5.60	1.25	0.65±0.04	$3.98^{+0.68}_{-0.78}$	-	3	-
SPT-CL J0241−3916	40.3032	−39.2756	8.84	0.25	1.03±0.08	$5.11^{+0.63}_{-0.72}$	56±6	3	-
SPT-CL J0241−2839	40.3524	−28.6595	6.61	1.75	0.238	$5.57^{+0.80}_{-0.91}$	113±5	8	-
SPT-CL J0241−2805	40.4507	−28.0951	7.35	0.25	0.34±0.02	$5.89^{+0.79}_{-0.89}$	109±19	2	-
SPT-CL J0244−3011	41.1693	−30.1941	5.33	0.25	1.37±0.03	$3.07^{+0.56}_{-0.65}$	20±3	7	-
SPT-CL J0245−2709	41.3751	−27.1626	9.35	0.50	0.71±0.01	$6.29^{+0.73}_{-0.86}$	102±4	3	-
SPT-CL J0246−2033	41.6151	−20.5555	7.05	1.50	0.317±0.007	$5.73^{+0.79}_{-0.92}$	120±10	3	-
SPT-CL J0249−3915	42.2662	−39.2643	6.99	0.50	0.66±0.01	$4.78^{+0.66}_{-0.76}$	63±4	3	-
SPT-CL J0252−2100	43.1103	−21.0106	7.85	0.75	0.71±0.02	$5.56^{+0.71}_{-0.83}$	94±32	3	SL
SPT-CL J0253−3818	43.3106	−38.3104	5.53	0.75	0.44±0.01	$4.18^{+0.77}_{-0.77}$	84±43	3	-
SPT-CL J0253−3247	43.3298	−32.7905	5.91	0.25	0.97±0.03	$3.82^{+0.61}_{-0.71}$	53±5	3	-
SPT-CL J0254−2413	43.5486	−24.2230	5.21	0.25	0.93±0.02	$3.76^{+0.66}_{-0.79}$	42±5	3	-
SPT-CL J0256−3455	44.1025	−34.9176	7.22	1.00	0.610±0.009	$4.95^{+0.68}_{-0.78}$	100±6	3	-
SPT-CL J0257−2325	44.2888	−23.4325	12.71	1.00	0.505	$8.04^{+0.88}_{-1.01}$	102±5	8	SL
SPT-CL J0257−2209	44.4233	−22.1509	9.50	1.00	0.322	$7.03^{+0.83}_{-0.96}$	42±5	8	SL
SPT-CL J0257−3449	44.4453	−34.8309	7.42	1.25	0.63±0.01	$5.01^{+0.67}_{-0.77}$	89±5	3	RC
SPT-CL J0258−3453	44.5258	−34.8943	5.49	0.75	0.354±0.009	$4.28^{+0.73}_{-0.84}$	52±3	3	RC
SPT-CL J0258−2004	44.7166	−20.0735	5.10	1.25	0.72±0.01	$3.91^{+0.73}_{-0.84}$	116±5	3	-
SPT-CL J0300−3617	45.1502	−36.2972	9.53	0.50	0.487±0.007	$6.22^{+0.72}_{-0.85}$	63±3	3	-
SPT-CL J0302−2240	45.5259	−22.6819	5.67	0.75	0.525±0.007	$4.58^{+0.77}_{-0.85}$	55±4	3	-
SPT-CL J0302−2805	45.5290	−28.0952	5.98	1.00	0.29±0.02	$5.09^{+0.82}_{-0.88}$	-	3	-
SPT-CL J0302−3306	45.5525	−33.1073	5.38	0.75	0.752	$3.73^{+0.72}_{-0.76}$	85±12	8	-
SPT-CL J0304−3656	46.0186	−36.9454	7.23	1.00	0.219	$5.49^{+0.74}_{-0.86}$	111±5	8	-
SPT-CL J0304−3803	46.0984	−38.0645	5.76	0.50	-	-	-	5	-
SPT-CL J0305−3229	46.4881	−32.4962	5.67	1.00	0.530±0.007	$4.17^{+0.75}_{-0.77}$	69±5	3	-
SPT-CL J0307−2840	46.7531	−28.6695	9.48	1.25	0.253	$7.15^{+0.82}_{-0.95}$	102±4	8	-
SPT-CL J0307−3424	46.8324	−34.4032	5.41	1.50	0.75±0.01	$3.76^{+0.66}_{-0.76}$	104±5	3	-
SPT-CL J0309−3209	47.2857	−32.1534	6.56	0.75	0.535±0.006	$4.71^{+0.69}_{-0.79}$	76±4	3	-
SPT-CL J0312−3510	48.0907	−35.1698	5.46	0.25	0.76±0.01	$3.79^{+0.66}_{-0.75}$	79±5	3	-
SPT-CL J0315−2718	48.7513	−27.3065	8.38	0.75	0.628±0.010	$5.96^{+0.77}_{-0.86}$	106±5	3	SL
SPT-CL J0319−2355	49.8156	−23.9263	5.69	0.50	0.588±0.007	$4.50^{+0.76}_{-0.84}$	113±5	3	-

Table 8 *continued*

Table 8 *(continued)*

SPT ID	R.A.	Decl.	Best		Redshift	M_{500c}	λ	Image Source	Notes
	(J2000)	(J2000)	ξ	θ_c		$(10^{14}h_{70}^{-1}M_\odot)$			
SPT-CL J0319−2244	49.9199	−22.7334	7.83	1.25	0.458±0.008	$5.94^{+0.78}_{-0.89}$	109±5	3	-
SPT-CL J0319−3345	49.9281	−33.7507	5.97	1.00	0.41±0.01	$4.52^{+0.73}_{-0.81}$	61±4	3	-
SPT-CL J0319−2853	49.9623	−28.8995	5.34	1.50	0.355	$4.55^{+0.82}_{-0.85}$	105±16	8	-
SPT-CL J0323−2916	50.7690	−29.2687	5.10	1.00	0.295±0.006	$4.47^{+0.77}_{-0.92}$	101±13	3	-
SPT-CL J0328−2140	52.0544	−21.6677	8.98	0.25	0.577±0.007	$6.35^{+0.76}_{-0.88}$	77±7	3	-
SPT-CL J0329−2330	52.3189	−23.5021	18.86	0.25	1.227	$8.44^{+0.87}_{-1.01}$	61±10	8	-
SPT-CL J0330−2500	52.5730	−25.0085	5.53	0.25	0.93±0.02	$3.96^{+0.68}_{-0.77}$	106±10	3	-
SPT-CL J0330−2016	52.6254	−20.2713	5.29	0.25	-	-	-	3	-
SPT-CL J0330−2458	52.7060	−24.9771	5.36	0.25	0.95±0.02	$3.83^{+0.69}_{-0.78}$	45±5	3	-
SPT-CL J0331−3529	52.7548	−35.4995	5.55	1.00	0.85±0.01	$3.72^{+0.65}_{-0.73}$	60±5	3	-
SPT-CL J0331−2100	52.7737	−21.0064	5.88	0.50	0.188	$5.14^{+0.88}_{-0.88}$	56±4	8	RC
SPT-CL J0332−2524	53.0402	−25.4021	5.69	0.25	0.81±0.01	$4.18^{+0.74}_{-0.84}$	58±4	3	-
SPT-CL J0333−3707	53.3519	−37.1246	5.07	0.50	1.05±0.04	$3.25^{+0.55}_{-0.70}$	-	3	-
SPT-CL J0336−2033	54.0520	−20.5661	6.73	1.50	0.84±0.01	$4.81^{+0.67}_{-0.79}$	110±6	3	-
SPT-CL J0336−3929	54.2193	−39.4990	8.92	1.25	0.40±0.01	$6.08^{+0.71}_{-0.86}$	102±4	3	-
SPT-CL J0337−2330	54.4750	−23.5004	5.48	1.00	0.80±0.01	$4.10^{+0.75}_{-0.77}$	87±5	3	-
SPT-CL J0339−3345	54.9031	−33.7651	5.31	0.25	0.85±0.01	$3.60^{+0.63}_{-0.73}$	44±4	3	-
SPT-CL J0340−2201	55.2131	−22.0268	6.39	0.50	0.92±0.02	$4.48^{+0.71}_{-0.79}$	76±5	3	-
SPT-CL J0343−3917	55.8514	−39.2844	8.84	0.75	0.804±0.010	$5.42^{+0.64}_{-0.76}$	92±5	3	-
SPT-CL J0346−2537	56.5982	−25.6211	5.48	0.75	0.577±0.007	$4.38^{+0.75}_{-0.86}$	94±4	3	-
SPT-CL J0347−3333	56.8845	−33.5637	5.42	0.75	0.451±0.010	$4.10^{+0.74}_{-0.81}$	51±7	3	-
SPT-CL J0347−2332	56.9568	−23.5362	7.57	1.50	0.39±0.03	$5.92^{+0.79}_{-0.88}$	-	3	-
SPT-CL J0348−2144	57.0020	−21.7447	9.86	1.25	0.347±0.008	$7.16^{+0.79}_{-0.96}$	191±6	3	SL
SPT-CL J0349−2717	57.4449	−27.2982	5.85	0.25	0.85±0.01	$4.21^{+0.77}_{-0.78}$	91±6	3	-
SPT-CL J0351−3937	57.7887	−39.6275	5.32	1.25	0.278±0.006	$4.25^{+0.73}_{-0.83}$	72±5	3	-
SPT-CL J0352−2644	58.1743	−26.7358	6.36	0.25	0.808±0.010	$4.65^{+0.66}_{-0.78}$	139±7	3	SL
SPT-CL J0352−3858	58.2116	−38.9769	5.88	1.50	0.229±0.004	$4.67^{+0.80}_{-0.80}$	78±4	3	-
SPT-CL J0354−3745	58.6506	−37.7516	10.58	0.75	0.251	$7.01^{+0.78}_{-0.94}$	94±3	8	SL
SPT-CL J0355−3634	58.8799	−36.5694	6.73	1.25	0.320	$5.08^{+0.73}_{-0.83}$	88±4	8	-
SPT-CL J0355−3939	58.9280	−39.6649	6.13	0.75	0.91±0.02	$3.99^{+0.63}_{-0.72}$	44±4	3	-
SPT-CL J0355−3741	58.9931	−37.6981	5.48	0.75	0.473	$4.11^{+0.73}_{-0.81}$	71±3	8	-
SPT-CL J0356−3416	59.0731	−34.2762	5.37	0.50	0.324±0.007	$4.22^{+0.74}_{-0.83}$	89±3	3	RC
SPT-CL J0356−3431	59.1972	−34.5188	7.08	1.00	0.356±0.009	$5.22^{+0.73}_{-0.84}$	92±3	3	-
SPT-CL J0358−2415	59.6966	−24.2562	9.06	1.00	0.63±0.01	$6.31^{+0.74}_{-0.87}$	97±17	3	-
SPT-CL J0358−2955	59.7201	−29.9299	16.33	0.50	0.425	$8.81^{+0.88}_{-1.08}$	123±4	8	SL
SPT-CL J0400−2926	60.1641	−29.4406	10.85	0.75	0.78±0.01	$6.97^{+0.76}_{-0.91}$	96±5	3	-
SPT-CL J0402−2359	60.5637	−23.9919	5.98	0.50	0.95±0.02	$4.31^{+0.76}_{-0.75}$	35±5	3	-
SPT-CL J0404−2422	61.1561	−24.3692	7.06	0.75	0.270±0.005	$5.96^{+0.82}_{-0.93}$	97±6	3	-
SPT-CL J0404−3526	61.1591	−35.4423	7.08	1.00	0.572±0.007	$5.45^{+0.75}_{-0.85}$	107±12	3	-
SPT-CL J0407−2657	61.8968	−26.9621	5.85	1.25	0.216±0.004	$5.23^{+0.92}_{-0.91}$	58±3	3	-
SPT-CL J0411−2158	62.7775	−21.9766	6.15	1.00	0.64±0.01	$4.84^{+0.80}_{-0.86}$	81±4	3	-
SPT-CL J0416−2404	64.0401	−24.0673	13.84	0.75	0.396	$8.98^{+0.94}_{-1.12}$	165±5	8	-
SPT-CL J0425−2230	66.2965	−22.5029	6.21	2.00	0.76±0.01	$4.71^{+0.80}_{-0.76}$	102±6	3	-
SPT-CL J0425−3742	66.3836	−37.7153	8.82	1.00	0.321±0.007	$6.78^{+0.78}_{-0.94}$	96±3	3	-
SPT-CL J0429−3051	67.4519	−30.8626	5.40	0.50	0.225±0.004	$4.80^{+0.90}_{-0.91}$	91±4	3	-

Table 8 *continued*

Table 8 *(continued)*

SPT ID	R.A.	Decl.	Best		Redshift	M_{500c}	λ	Image Source	Notes
	(J2000)	(J2000)	ξ	θ_c		$(10^{14} h_{70}^{-1} M_\odot)$			
SPT-CL J0431−3442	67.8795	−34.7154	5.69	1.25	0.460±0.008	$4.73^{+0.80}_{-0.88}$	81±5	3	-
SPT-CL J0438−2538	69.6413	−25.6402	5.26	0.50	-	-	-	3	-
SPT-CL J0445−2301	71.4982	−23.0318	5.05	1.50	-	-	-	3	-
SPT-CL J0446−3703	71.7021	−37.0623	10.64	0.50	0.600±0.007	$7.12^{+0.79}_{-0.94}$	204±6	3	-
SPT-CL J0454−3736	73.5926	−37.6043	5.89	0.50	0.509±0.006	$4.78^{+0.82}_{-0.83}$	84±4	3	-
SPT-CL J0454−2016	73.6881	−20.2831	13.58	0.50	0.72±0.01	$8.16^{+0.82}_{-1.02}$	111±5	3	-
SPT-CL J0454−2948	73.6968	−29.8155	5.08	0.75	0.69±0.02	$4.06^{+0.73}_{-0.87}$	51±4	3	-
SPT-CL J0455−3417	73.9372	−34.2883	5.24	0.75	0.613±0.009	$4.21^{+0.74}_{-0.86}$	111±5	3	RC
SPT-CL J0455−2225	73.9549	−22.4246	5.04	0.25	-	-	-	3	-
SPT-CL J0500−2038	75.1613	−20.6406	6.78	0.75	0.77±0.01	$5.07^{+0.74}_{-0.82}$	103±6	3	-
SPT-CL J0502−2902	75.7274	−29.0359	9.54	0.75	0.605±0.008	$6.74^{+0.79}_{-0.93}$	93±5	3	-
SPT-CL J0504−2759	76.1869	−27.9965	12.30	0.50	0.590±0.007	$7.95^{+0.82}_{-1.01}$	106±5	3	SL
SPT-CL J0505−3219	76.2724	−32.3311	5.65	0.75	0.145±0.005	$5.11^{+0.89}_{-0.89}$	48±3	3	-
SPT-CL J0509−2833	77.4969	−28.5610	7.21	0.25	0.75±0.01	$5.35^{+0.73}_{-0.82}$	84±5	3	-
SPT-CL J0512−3604	78.1462	−36.0668	5.31	0.75	0.518±0.006	$4.39^{+0.77}_{-0.88}$	96±5	3	-
SPT-CL J0512−3848	78.2361	−38.8003	7.54	1.50	0.326±0.007	$6.07^{+0.87}_{-0.88}$	119±4	3	SL
SPT-CL J0516−2236	79.2375	−22.6166	5.58	0.50	0.302±0.006	$4.91^{+0.88}_{-0.91}$	85±4	3	-
SPT-CL J0519−2701	79.8861	−27.0322	5.04	0.25	-	-	-	3	-
SPT-CL J0521−3917	80.3379	−39.2998	5.42	0.25	0.43±0.01	$4.54^{+0.81}_{-0.90}$	72±4	3	-
SPT-CL J0521−2754	80.3560	−27.9083	5.47	1.50	0.317	$4.82^{+0.88}_{-0.88}$	100±47	8	SL
SPT-CL J0525−3035	81.4763	−30.5836	6.56	1.25	0.199	$5.67^{+0.81}_{-0.93}$	98±6	8	-
SPT-CL J0528−2942	82.0675	−29.7154	6.27	2.00	0.157	$5.59^{+0.90}_{-0.90}$	68±3	8	-
SPT-CL J0528−3927	82.2161	−39.4593	13.02	2.25	0.284	$8.75^{+0.94}_{-1.11}$	111±7	8	-
SPT-CL J0530−2227	82.6498	−22.4556	7.26	1.50	0.172±0.004	$6.25^{+0.83}_{-0.96}$	90±4	3	-
SPT-CL J0531−2641	82.8726	−26.6961	5.77	0.25	-	-	-	3	-
SPT-CL J0532−3701	83.2270	−37.0278	14.37	1.00	0.275	$9.34^{+0.96}_{-1.17}$	202±6	8	SL
SPT-CL J0540−3918	85.0103	−39.3054	5.92	0.25	0.479±0.008	$4.84^{+0.84}_{-0.86}$	49±6	3	-
SPT-CL J0540−2127	85.2061	−21.4638	5.53	1.25	0.528±0.007	$4.60^{+0.82}_{-0.87}$	69±5	3	SL
SPT-CL J0542−3559	85.7370	−35.9978	11.63	0.75	0.41±0.01	$7.92^{+0.85}_{-1.03}$	141±5	3	-
SPT-CL J0543−2941	85.7510	−29.6981	6.52	0.25	1.19±0.15	$4.36^{+0.65}_{-0.73}$	-	6	-
SPT-CL J0543−3620	85.8697	−36.3377	5.36	0.25	0.84±0.01	$3.98^{+0.73}_{-0.83}$	77±5	3	-
SPT-CL J0544−3949	86.2443	−39.8261	8.15	0.50	0.518±0.007	$6.11^{+0.77}_{-0.89}$	73±4	3	-
SPT-CL J0545−3237	86.3813	−32.6201	5.20	1.50	0.42±0.01	$4.45^{+0.77}_{-0.90}$	64±9	3	-
SPT-CL J0547−3152	86.9093	−31.8760	9.69	1.25	0.148	$7.50^{+0.85}_{-1.02}$	120±4	8	-
SPT-CL J0552−2103	88.2252	−21.0665	5.14	2.75	0.099	$4.85^{+0.84}_{-0.97}$	61±24	8	-
SPT-CL J0553−3342	88.3512	−33.7123	20.93	1.25	0.41±0.03	$11.33^{+1.16}_{-1.37}$	-	3	SL
SPT-CL J0556−3539	89.0649	−35.6529	5.07	0.25	-	-	-	3	-
SPT-CL J0600−2007	90.0470	−20.1207	18.81	1.25	0.46±0.03	$10.66^{+1.09}_{-1.29}$	-	7	SL
SPT-CL J1000−3016	150.0065	−30.2751	7.28	1.00	0.21±0.02	$7.09^{+0.94}_{-1.08}$	-	2	SL
SPT-CL J1000−2037	150.1476	−20.6199	5.13	2.25	0.57±0.04	$4.88^{+0.87}_{-1.01}$	-	2	-
SPT-CL J1023−2715	155.9547	−27.2581	8.89	0.75	0.253	$8.01^{+0.96}_{-1.13}$	-	8	-
SPT-CL J1039−2502	159.9309	−25.0351	6.17	0.50	0.83±0.03	$5.27^{+0.88}_{-0.89}$	-	2	-
SPT-CL J1042−2847	160.5667	−28.7909	6.63	0.50	0.72±0.04	$5.76^{+0.91}_{-0.91}$	-	2	SL
SPT-CL J1101−2244	165.3057	−22.7357	5.38	2.25	0.142	$5.69^{+0.98}_{-1.11}$	-	8	-
SPT-CL J1105−1954	166.3670	−19.9056	5.25	0.75	0.51±0.04	$5.03^{+0.98}_{-0.99}$	-	2	-

Table 8 *continued*

Table 8 *(continued)*

SPT ID	R.A.	Decl.	Best		Redshift	M_{500c}	λ	Image Source	Notes
	(J2000)	(J2000)	ξ	θ_c		$(10^{14} h_{70}^{-1} M_\odot)$			
SPT-CL J1115−2550	168.9862	−25.8431	5.61	0.50	0.52±0.04	$5.34^{+0.94}_{-0.96}$	-	2	-
SPT-CL J1131−1955	172.9821	−19.9249	10.63	1.50	0.307	$8.89^{+0.95}_{-1.18}$	-	8	SL
SPT-CL J1144−2835	176.0421	−28.5847	5.14	0.50	0.575	$4.86^{+0.94}_{-1.00}$	-	8	SL
SPT-CL J1150−2805	177.7109	−28.0868	24.00	1.75	0.39±0.05	$14.45^{+1.47}_{-1.69}$	-	7	SL
SPT-CL J1153−2137	178.3836	−21.6231	5.65	1.00	0.46±0.04	$5.48^{+0.91}_{-1.02}$	-	2	-
SPT-CL J1154−2609	178.5660	−26.1533	6.92	0.25	0.34±0.02	$6.63^{+0.88}_{-1.03}$	-	2	-
SPT-CL J1157−2143	179.3901	−21.7228	5.05	0.25	-	-	-	2	-
SPT-CL J1159−2258	179.9615	−22.9816	5.81	0.25	0.70±0.04	$4.42^{+0.77}_{-0.80}$	-	2	-
SPT-CL J1200−2002	180.0551	−20.0438	7.28	0.50	0.67±0.04	$5.34^{+0.73}_{-0.82}$	-	2	-
SPT-CL J1203−2131	180.8185	−21.5298	8.48	1.50	0.199	$6.68^{+0.82}_{-0.96}$	-	8	-
SPT-CL J1210−2218	182.7116	−22.3102	5.82	0.75	0.26±0.02	$5.02^{+0.81}_{-0.89}$	-	2	RC
SPT-CL J1213−3013	183.3033	−30.2223	5.15	3.00	-	-	-	-	-
SPT-CL J1221−3010	185.3879	−30.1713	11.63	0.75	0.71±0.04	$7.23^{+0.76}_{-0.93}$	-	2	-
SPT-CL J1223−3014	185.8559	−30.2448	6.40	0.25	0.47±0.04	$5.10^{+0.77}_{-0.86}$	-	2	SL
SPT-CL J1227−2227	186.7883	−22.4508	6.24	2.25	0.27±0.02	$5.28^{+0.79}_{-0.90}$	-	2	-
SPT-CL J1229−2021	187.2582	−20.3666	5.28	1.75	0.41±0.04	$4.40^{+0.80}_{-0.90}$	-	2	-
SPT-CL J1231−2548	187.7982	−25.8126	6.42	0.75	0.47±0.04	$5.12^{+0.76}_{-0.86}$	-	2	-
SPT-CL J1238−2854	189.5931	−28.9009	6.92	0.25	0.72±0.04	$5.06^{+0.74}_{-0.80}$	-	2	-
SPT-CL J1239−2149	189.8134	−21.8246	5.19	1.50	-	-	-	1	-
SPT-CL J1240−2255	190.2485	−22.9296	5.01	0.50	0.78±0.08	$3.81^{+0.66}_{-0.81}$	-	2	-
SPT-CL J1245−2259	191.4352	−22.9969	5.11	1.00	1.04±0.04	$3.55^{+0.63}_{-0.77}$	-	4	-
SPT-CL J1246−2548	191.5274	−25.8011	5.79	1.50	0.32±0.02	$4.91^{+0.81}_{-0.89}$	-	2	-
SPT-CL J1250−3010	192.5661	−30.1676	5.93	0.50	0.43±0.04	$4.83^{+0.83}_{-0.84}$	-	2	-
SPT-CL J1252−2220	193.1064	−22.3364	5.28	0.25	1.27±0.16	$3.41^{+0.64}_{-0.72}$	-	6	-
SPT-CL J1253−2610	193.4332	−26.1742	5.31	1.00	0.49±0.04	$4.32^{+0.84}_{-0.85}$	-	2	-
SPT-CL J1256−2851	194.0740	−28.8594	5.93	0.75	0.36±0.04	$4.95^{+0.85}_{-0.87}$	-	2	RC
SPT-CL J1257−2926	194.3183	−29.4489	10.20	0.75	0.53±0.04	$6.97^{+0.77}_{-0.92}$	-	2	-
SPT-CL J1259−1953	194.8408	−19.8995	5.85	0.75	1.05±0.05	$3.98^{+0.71}_{-0.72}$	-	7	-
SPT-CL J1302−2405	195.6523	−24.0878	7.64	0.25	0.67±0.04	$5.50^{+0.73}_{-0.84}$	-	2	-
SPT-CL J1304−2349	196.0548	−23.8244	5.31	3.00	0.34±0.02	$4.55^{+0.79}_{-0.90}$	-	2	-
SPT-CL J1307−2052	196.8833	−20.8797	6.22	0.50	0.53±0.04	$4.91^{+0.81}_{-0.82}$	-	2	-
SPT-CL J1309−2417	197.4801	−24.2999	8.06	0.50	0.78±0.05	$5.59^{+0.68}_{-0.82}$	-	2	-
SPT-CL J1314−2515	198.6165	−25.2599	15.39	1.75	0.247	$9.66^{+0.97}_{-1.18}$	-	8	-
SPT-CL J1315−2117	198.7920	−21.2982	6.31	1.50	0.61±0.04	$4.84^{+0.78}_{-0.84}$	-	2	-
SPT-CL J1315−2806	198.8110	−28.1091	8.23	0.50	1.39±0.07	$4.76^{+0.61}_{-0.70}$	-	5	RC
SPT-CL J1323−2442	200.8031	−24.7112	5.46	1.75	0.30±0.02	$4.69^{+0.84}_{-0.86}$	-	2	-
SPT-CL J1325−2014	201.2721	−20.2336	6.99	1.25	0.192	$5.86^{+0.85}_{-0.92}$	-	8	-
SPT-CL J1333−2318	203.4162	−23.3011	5.50	1.00	0.126	$4.95^{+0.88}_{-0.90}$	-	8	-
SPT-CL J1335−2046	203.7929	−20.7708	6.47	1.25	0.51±0.04	$5.10^{+0.82}_{-0.80}$	-	2	-
SPT-CL J1336−2820	204.2287	−28.3485	5.17	0.25	-	-	-	4	-
SPT-CL J1342−2442	205.5035	−24.7051	6.44	0.75	0.81±0.03	$4.65^{+0.74}_{-0.78}$	-	2	SL
SPT-CL J1342−2757	205.5959	−27.9616	5.46	0.75	0.65±0.04	$4.26^{+0.75}_{-0.84}$	-	2	-
SPT-CL J1347−2052	206.9497	−20.8706	5.21	0.75	0.97±0.03	$3.72^{+0.64}_{-0.77}$	-	2	-
SPT-CL J1354−2011	208.5239	−20.1907	6.02	0.50	0.34±0.02	$5.02^{+0.78}_{-0.89}$	-	2	-
SPT-CL J2205−2955	331.2537	−29.9328	7.83	0.50	1.31±0.06	$4.90^{+0.65}_{-0.73}$	-	7	-

Table 8 *continued*

Table 8 *(continued)*

SPT ID	R.A.	Decl.	Best		Redshift	M_{500c}	λ	Image Source	Notes
	(J2000)	(J2000)	ξ	θ_c		$(10^{14} h_{70}^{-1} M_\odot)$			
SPT-CL J2211−2155	332.8326	−21.9176	5.42	1.00	0.44±0.04	$4.67^{+0.84}_{-0.89}$	-	2	-
SPT-CL J2215−3537	333.7665	−35.6208	13.73	0.25	1.160	$7.57^{+0.79}_{-0.92}$	-	8	-
SPT-CL J2215−3245	333.9082	−32.7654	5.66	0.25	0.69±0.05	$4.62^{+0.84}_{-0.84}$	-	2	-
SPT-CL J2217−3543	334.4461	−35.7273	5.86	1.25	0.149	$5.48^{+0.95}_{-0.95}$	-	8	-
SPT-CL J2218−3854	334.6690	−38.9018	8.03	0.50	0.138	$6.99^{+0.88}_{-1.01}$	-	8	RC
SPT-CL J2220−3509	335.1348	−35.1656	7.47	1.00	0.154	$6.61^{+0.86}_{-1.01}$	-	8	-
SPT-CL J2223−3302	335.7893	−33.0343	6.25	1.00	0.58±0.04	$5.19^{+0.80}_{-0.89}$	-	2	-
SPT-CL J2229−3631	337.3954	−36.5319	6.27	0.75	0.40±0.04	$5.45^{+0.84}_{-0.94}$	-	2	-
SPT-CL J2234−3159	338.5172	−31.9953	6.94	1.50	0.57±0.04	$5.65^{+0.82}_{-0.90}$	-	2	-
SPT-CL J2234−3744	338.6097	−37.7413	16.63	1.50	0.153	$11.05^{+1.16}_{-1.38}$	-	8	RC
SPT-CL J2234−3033	338.7173	−30.5596	6.15	1.00	0.251	$5.60^{+0.86}_{-0.98}$	-	8	-
SPT-CL J2239−3040	339.8571	−30.6719	5.47	0.25	-	-	-	4	RC
SPT-CL J2239−3231	339.9785	−32.5241	5.67	1.00	0.45±0.04	$4.95^{+0.88}_{-0.90}$	-	2	-
SPT-CL J2244−3704	341.0383	−37.0734	9.02	1.50	0.44±0.04	$7.00^{+0.82}_{-0.98}$	-	2	-
SPT-CL J2245−2113	341.4794	−21.2253	8.21	0.50	0.69±0.04	$6.01^{+0.78}_{-0.87}$	-	2	-
SPT-CL J2246−3210	341.7110	−32.1759	5.12	1.00	0.50±0.04	$4.47^{+0.81}_{-0.94}$	-	2	-
SPT-CL J2247−3300	341.9385	−33.0012	6.66	0.50	1.24±0.16	$4.51^{+0.71}_{-0.74}$	-	6	-
SPT-CL J2251−2247	342.8584	−22.7872	5.63	0.25	1.01±0.10	$4.08^{+0.71}_{-0.81}$	-	2	-
SPT-CL J2251−3324	342.9560	−33.4011	5.74	1.00	0.24±0.02	$5.29^{+0.93}_{-0.95}$	-	2	-
SPT-CL J2252−2134	343.2276	−21.5669	5.90	0.50	0.16±0.02	$5.41^{+0.87}_{-0.96}$	-	2	-
SPT-CL J2253−3344	343.3848	−33.7343	5.37	1.75	0.224	$5.04^{+0.87}_{-0.99}$	-	8	-
SPT-CL J2256−2241	344.0013	−22.6841	7.00	0.75	0.62±0.04	$5.47^{+0.74}_{-0.86}$	-	2	-
SPT-CL J2258−2256	344.5716	−22.9374	5.82	1.00	0.55±0.04	$4.80^{+0.85}_{-0.84}$	-	2	-
SPT-CL J2258−3447	344.6946	−34.7939	9.01	2.00	0.317	$7.23^{+0.82}_{-1.01}$	-	8	SL
SPT-CL J2259−3951	344.8158	−39.8591	6.56	0.75	0.531±0.008	$5.46^{+0.83}_{-0.89}$	94±18	3	-
SPT-CL J2259−2505	344.8759	−25.0996	5.50	0.50	0.43±0.04	$4.72^{+0.82}_{-0.95}$	-	2	RC
SPT-CL J2305−2248	346.3004	−22.8099	14.36	1.00	0.70±0.04	$8.57^{+0.87}_{-1.06}$	-	2	SL
SPT-CL J2306−2215	346.7137	−22.2605	7.07	0.50	0.81±0.06	$5.22^{+0.77}_{-0.77}$	-	2	-
SPT-CL J2315−2127	348.8280	−21.4570	5.69	0.50	0.54±0.04	$4.73^{+0.85}_{-0.85}$	-	2	-
SPT-CL J2315−3747	348.9303	−37.7859	6.45	1.50	0.181	$5.92^{+0.87}_{-0.95}$	-	8	-
SPT-CL J2317−3648	349.4318	−36.8104	9.88	0.25	0.82±0.03	$6.75^{+0.75}_{-0.90}$	-	2	-
SPT-CL J2317−3239	349.4550	−32.6656	9.77	0.50	1.05±0.04	$6.30^{+0.71}_{-0.84}$	-	4	-
SPT-CL J2318−3513	349.6641	−35.2317	5.52	0.25	0.98±0.07	$4.12^{+0.74}_{-0.83}$	-	5	-
SPT-CL J2319−2245	349.9832	−22.7563	6.66	0.25	0.59±0.04	$5.33^{+0.75}_{-0.87}$	-	2	-
SPT-CL J2321−2725	350.3827	−27.4330	5.59	0.25	0.67±0.04	$4.47^{+0.76}_{-0.88}$	-	2	-
SPT-CL J2322−3805	350.5623	−38.0905	9.12	0.50	0.36±0.03	$7.22^{+0.83}_{-1.00}$	-	2	-
SPT-CL J2332−2944	353.1542	−29.7472	5.01	0.25	-	-	-	1	-
SPT-CL J2334−2413	353.6683	−24.2289	6.19	0.25	0.73±0.05	$4.78^{+0.77}_{-0.85}$	-	2	-
SPT-CL J2335−3256	353.8497	−32.9479	5.44	1.25	0.51±0.04	$4.71^{+0.87}_{-0.88}$	-	2	-
SPT-CL J2335−2950	353.9182	−29.8343	10.32	0.50	0.70±0.04	$6.99^{+0.77}_{-0.93}$	-	2	-
SPT-CL J2336−3210	354.0138	−32.1807	5.65	1.00	0.66±0.04	$4.64^{+0.85}_{-0.86}$	-	2	SL
SPT-CL J2336−3205	354.0784	−32.0999	5.12	0.75	0.63±0.04	$4.33^{+0.78}_{-0.90}$	-	2	SL
SPT-CL J2337−3822	354.4074	−38.3686	5.11	0.75	0.73±0.05	$4.20^{+0.74}_{-0.88}$	-	2	-
SPT-CL J2339−3555	354.8519	−35.9316	5.84	1.25	0.61±0.04	$4.85^{+0.83}_{-0.85}$	-	2	SL
SPT-CL J2344−3153	356.1431	−31.8869	5.95	0.25	0.77±0.05	$4.67^{+0.83}_{-0.84}$	-	2	-

Table 8 *continued*

Table 8 *(continued)*

SPT ID	R.A.	Decl.	Best		Redshift	M_{500c}	λ	Image Source	Notes
	(J2000)	(J2000)	ξ	θ_c		$(10^{14}h_{70}^{-1}M_\odot)$			
SPT-CL J2346−3820	356.5686	−38.3363	5.87	1.00	1.06±0.14	$4.28^{+0.72}_{-0.81}$	-	6	-
SPT-CL J2346−3316	356.6482	−33.2818	5.65	0.75	0.67±0.04	$4.63^{+0.85}_{-0.87}$	-	2	-
SPT-CL J2347−3634	356.8119	−36.5781	7.79	0.75	0.46±0.05	$6.30^{+0.81}_{-0.95}$	-	7	-
SPT-CL J2351−2604	357.9161	−26.0783	11.08	1.25	0.230	$8.22^{+0.89}_{-1.07}$	-	8	SL
SPT-CL J2351−2547	357.9707	−25.7877	5.47	1.25	0.61±0.04	$4.49^{+0.81}_{-0.85}$	-	2	-
SPT-CL J2357−3446	359.2509	−34.7682	5.55	2.25	0.050	$5.37^{+0.97}_{-0.96}$	-	8	RC

NOTE—Here we report for each cluster candidate detected at $\xi > 5$ the candidate name, position, detection significance (ξ), the β-model core radius (in arcminutes) corresponding to this significance (see Section 3), and the source of followup imaging. When a candidate is confirmed as a cluster we also report its redshift and mass, richness from RM in "scanning mode"' (where available, see Section 4.2.1), and flag if the system has been identified as a strong gravitational lens (SL) or if the estimated radio contamination to the SZ signal exceeds 10% (RC; see Section 3.5). The key for the Image Source column is as follows: [1] Pan-STARRS, [2]Magellan/PISCO, [3] DES, [4] Magellan/FourStar, [5] *Spitzer*/IRAC, [6] WISE, [7] Literature photometric redshift, [8] Spectroscopic redshift. Generally, data from Pan-STARRS is deep enough to confirm clusters to $z \sim 0.6$, DES and PISCO to $z \sim 0.8-1.0$, FourStar to $z \sim 1.2$ and *Spitzer* to $z \sim 1.5$.

Table 9. Confirmed galaxy clusters $4 < \xi < 5$ in the SPTpol Extended Cluster Survey.

SPT ID	R.A.	Decl.	Best		Redshift	M_{500c}	λ	Imaging	Notes
	(J2000)	(J2000)	ξ	θ_c		$(10^{14}h_{70}^{-1}M_\odot)$			
SPT-CL J0000−3838	0.0118	−38.6467	4.37	2.25	0.305±0.007	$4.25^{+0.71}_{-0.95}$	49±3	3	-
SPT-CL J0000−2805	0.0906	−28.0947	4.79	2.50	0.23±0.03	$5.05^{+0.91}_{-1.09}$	-	1	-
SPT-CL J0001−3446	0.3080	−34.7729	4.23	0.25	0.73±0.02	$3.72^{+0.57}_{-0.83}$	45±7	3	-
SPT-CL J0011−2841	2.8272	−28.6859	4.13	0.25	0.089±0.006	$4.79^{+0.74}_{-1.05}$	22±5	3	-
SPT-CL J0019−2026	4.7834	−20.4475	4.95	1.25	0.277	$5.12^{+0.98}_{-1.05}$	-	8	-
SPT-CL J0020−2634	5.2048	−26.5799	4.14	0.25	0.233±0.006	$4.62^{+0.74}_{-1.02}$	22±4	3	-
SPT-CL J0023−3252	5.7941	−32.8672	4.28	0.75	0.66±0.01	$3.83^{+0.61}_{-0.84}$	45±4	3	-
SPT-CL J0025−3618	6.3664	−36.3085	4.53	0.25	0.215±0.005	$4.48^{+0.77}_{-0.99}$	21±2	3	-
SPT-CL J0027−3729	6.9845	−37.4854	4.32	0.25	0.83±0.02	$3.66^{+0.56}_{-0.81}$	23±4	3	-
SPT-CL J0033−3413	8.4038	−34.2293	4.52	0.25	0.233±0.005	$4.46^{+0.77}_{-0.97}$	33±3	3	-
SPT-CL J0036−2104	9.1838	−21.0828	4.23	0.25	0.356±0.009	$4.52^{+0.74}_{-1.00}$	72±7	3	-
SPT-CL J0036−3144	9.2171	−31.7460	4.49	1.75	0.41±0.01	$4.23^{+0.73}_{-0.94}$	72±4	3	RC
SPT-CL J0042−2238	10.5870	−22.6412	4.17	0.75	0.71±0.01	$4.06^{+0.62}_{-0.88}$	61±4	3	-
SPT-CL J0044−3202	11.1361	−32.0427	4.28	2.00	0.40±0.01	$4.12^{+0.67}_{-0.92}$	64±4	3	-
SPT-CL J0056−3732	14.0070	−37.5446	4.59	1.25	0.168±0.004	$4.58^{+0.79}_{-0.99}$	66±5	3	-
SPT-CL J0056−3400	14.1260	−34.0022	4.05	0.50	0.96±0.02	$3.40^{+0.50}_{-0.74}$	20±4	3	-
SPT-CL J0100−3246	15.0641	−32.7705	4.19	0.50	0.53±0.01	$3.92^{+0.61}_{-0.88}$	19±3	3	-
SPT-CL J0102−2324	15.6648	−23.4070	4.38	0.25	0.508±0.007	$4.41^{+0.74}_{-0.99}$	85±4	3	-
SPT-CL J0104−2357	16.1591	−23.9648	4.24	2.75	0.168±0.004	$4.75^{+0.80}_{-1.08}$	86±21	3	-
SPT-CL J0106−3719	16.5568	−37.3233	4.55	1.75	0.560±0.008	$4.11^{+0.66}_{-0.89}$	50±4	3	-
SPT-CL J0107−3015	16.8316	−30.2660	4.20	2.75	0.505±0.008	$3.96^{+0.64}_{-0.89}$	47±3	3	-
SPT-CL J0109−3613	17.4714	−36.2292	4.58	1.00	0.92±0.02	$3.66^{+0.62}_{-0.82}$	32±4	3	-
SPT-CL J0115−2917	18.9569	−29.2837	4.59	0.25	0.41±0.01	$4.69^{+0.81}_{-1.02}$	76±4	3	-
SPT-CL J0119−2025	19.9244	−20.4265	4.66	0.25	0.82±0.01	$4.18^{+0.69}_{-0.92}$	130±14	3	-
SPT-CL J0121−3355	20.4786	−33.9197	4.99	1.00	0.568±0.006	$4.34^{+0.79}_{-0.93}$	97±4	3	-
SPT-CL J0122−2420	20.6990	−24.3372	4.49	0.25	0.497±0.007	$4.51^{+0.74}_{-0.98}$	83±11	3	-
SPT-CL J0128−3625	22.1265	−36.4326	4.24	2.75	0.87±0.02	$3.56^{+0.58}_{-0.79}$	19±5	3	-

Table 9 *continued*

Table 9 *(continued)*

SPT ID	R.A.	Decl.	Best		Redshift	M_{500c}	λ	Imaging	Notes
	(J2000)	(J2000)	ξ	θ_c		$(10^{14} h_{70}^{-1} M_\odot)$			
SPT-CL J0134−2949	23.5878	−29.8311	4.35	0.50	0.88±0.01	$3.90^{+0.64}_{-0.88}$	90±7	3	-
SPT-CL J0135−2045	23.9760	−20.7520	4.89	1.75	0.376±0.010	$4.93^{+0.88}_{-1.04}$	94±8	3	-
SPT-CL J0138−2155	24.5192	−21.9212	4.76	0.75	0.338	$4.88^{+0.87}_{-1.05}$	107±17	8	SL
SPT-CL J0143−3515	25.9255	−35.2551	4.31	0.25	0.067	$4.49^{+0.73}_{-1.00}$	-	8	-
SPT-CL J0144−2214	26.1703	−22.2356	4.73	0.50	0.278	$4.97^{+0.88}_{-1.05}$	73±3	8	SL
SPT-CL J0149−3826	27.3489	−38.4364	4.99	1.75	0.38±0.03	$4.62^{+0.81}_{-0.94}$	-	3	-
SPT-CL J0151−3544	27.8176	−35.7372	4.95	0.25	0.533±0.006	$4.36^{+0.78}_{-0.94}$	75±3	3	SL
SPT-CL J0153−2453	28.4398	−24.8910	4.78	1.00	0.40±0.01	$4.81^{+0.84}_{-1.05}$	21±3	3	-
SPT-CL J0157−2359	29.2715	−23.9925	4.85	2.25	0.204±0.006	$5.13^{+0.92}_{-1.10}$	32±9	3	-
SPT-CL J0158−2910	29.5388	−29.1775	4.06	0.50	0.574±0.007	$4.15^{+0.65}_{-0.92}$	85±4	3	-
SPT-CL J0158−2240	29.6302	−22.6692	4.45	1.25	0.93±0.02	$3.91^{+0.64}_{-0.87}$	37±7	3	-
SPT-CL J0159−3010	29.9314	−30.1737	4.59	0.50	0.69±0.01	$3.67^{+0.62}_{-0.82}$	96±5	3	-
SPT-CL J0200−2836	30.0345	−28.6124	4.07	0.50	0.39±0.01	$3.76^{+0.57}_{-0.83}$	24±3	3	-
SPT-CL J0200−2236	30.0889	−22.6113	4.46	1.50	0.280±0.006	$4.77^{+0.80}_{-1.04}$	79±4	3	-
SPT-CL J0202−2812	30.6699	−28.2145	4.01	1.00	0.116±0.005	$3.97^{+0.63}_{-0.89}$	24±3	3	-
SPT-CL J0203−2404	30.7609	−24.0771	4.20	0.25	0.66±0.02	$3.51^{+0.55}_{-0.79}$	19±3	3	-
SPT-CL J0206−2921	31.5045	−29.3611	4.37	3.00	0.278±0.009	$4.02^{+0.65}_{-0.88}$	43±20	3	-
SPT-CL J0206−3831	31.5740	−38.5185	4.41	1.25	0.457±0.009	$3.54^{+0.57}_{-0.78}$	67±4	3	-
SPT-CL J0209−2730	32.2704	−27.5137	4.85	1.00	0.314±0.008	$4.25^{+0.76}_{-0.91}$	47±8	3	-
SPT-CL J0210−2446	32.5036	−24.7828	4.53	0.25	0.70±0.01	$3.64^{+0.61}_{-0.81}$	60±4	3	-
SPT-CL J0212−2051	33.1258	−20.8589	4.31	1.50	0.575±0.007	$3.68^{+0.57}_{-0.81}$	79±7	3	-
SPT-CL J0213−2912	33.2510	−29.2084	4.08	0.75	0.90±0.02	$3.23^{+0.50}_{-0.71}$	38±5	3	-
SPT-CL J0213−2758	33.2731	−27.9713	4.32	0.50	0.323±0.008	$3.94^{+0.67}_{-0.87}$	36±10	3	-
SPT-CL J0214−3349	33.5258	−33.8296	4.82	1.25	0.238	$3.98^{+0.71}_{-0.85}$	72±6	8	-
SPT-CL J0214−3631	33.6778	−36.5296	4.65	2.75	0.248±0.005	$3.85^{+0.66}_{-0.83}$	72±4	3	-
SPT-CL J0215−3518	33.8536	−35.3061	4.26	1.25	0.90±0.02	$3.03^{+0.48}_{-0.67}$	52±5	3	-
SPT-CL J0215−2948	33.9047	−29.8134	4.15	0.25	0.253±0.007	$3.59^{+0.57}_{-0.80}$	22±2	3	-
SPT-CL J0217−2534	34.3638	−25.5795	4.59	1.00	0.71±0.02	$3.67^{+0.62}_{-0.80}$	111±15	3	-
SPT-CL J0223−2753	35.8629	−27.8888	4.26	0.50	0.44±0.01	$3.77^{+0.61}_{-0.85}$	37±3	3	-
SPT-CL J0224−3223	36.0950	−32.3846	4.00	0.25	0.540±0.008	$3.28^{+0.49}_{-0.72}$	31±3	3	-
SPT-CL J0224−3415	36.1966	−34.2591	4.53	0.25	0.593±0.008	$3.45^{+0.56}_{-0.77}$	74±4	3	-
SPT-CL J0224−3811	36.2148	−38.1997	4.81	0.25	0.281±0.006	$3.93^{+0.69}_{-0.84}$	62±3	3	-
SPT-CL J0225−3635	36.3562	−36.5931	4.21	0.25	0.46±0.01	$3.44^{+0.54}_{-0.76}$	25±3	3	-
SPT-CL J0225−3550	36.4416	−35.8458	4.41	0.25	0.289±0.006	$3.68^{+0.62}_{-0.83}$	79±5	3	-
SPT-CL J0226−2648	36.5273	−26.8164	4.24	1.00	0.99±0.03	$3.21^{+0.49}_{-0.69}$	36±5	3	-
SPT-CL J0227−2448	36.7836	−24.8158	4.38	0.25	0.65±0.01	$3.63^{+0.57}_{-0.80}$	63±4	3	-
SPT-CL J0227−2852	36.8027	−28.8688	4.83	0.50	0.214	$4.36^{+0.77}_{-0.93}$	44±16	8	-
SPT-CL J0228−3522	37.0114	−35.3713	4.23	1.25	0.283±0.008	$3.61^{+0.57}_{-0.81}$	22±2	3	RC
SPT-CL J0228−2427	37.0731	−24.4585	4.58	1.00	0.305±0.006	$4.12^{+0.70}_{-0.91}$	89±6	3	-
SPT-CL J0228−2835	37.1156	−28.5848	4.76	1.75	0.83±0.01	$3.61^{+0.62}_{-0.80}$	58±5	3	-
SPT-CL J0229−3737	37.3520	−37.6211	4.45	0.25	0.93±0.02	$3.09^{+0.51}_{-0.68}$	135±7	3	-
SPT-CL J0230−3054	37.6388	−30.9136	4.32	1.25	0.505±0.007	$3.43^{+0.54}_{-0.76}$	41±3	3	-
SPT-CL J0233−2952	38.3538	−29.8805	4.20	1.00	0.96±0.03	$2.95^{+0.45}_{-0.64}$	19±4	3	-
SPT-CL J0237−2948	39.3819	−29.8115	4.24	1.00	0.71±0.02	$3.50^{+0.55}_{-0.77}$	19±3	3	-
SPT-CL J0239−2455	39.9299	−24.9307	4.18	0.25	0.65±0.01	$3.53^{+0.55}_{-0.78}$	80±5	3	SL

Table 9 *continued*

Table 9 *(continued)*

SPT ID	R.A.	Decl.	Best		Redshift	M_{500c}	λ	Imaging	Notes
	(J2000)	(J2000)	ξ	θ_c		$(10^{14}h_{70}^{-1}M_\odot)$			
SPT-CL J0240−3023	40.1761	−30.3953	4.15	1.50	0.46±0.01	$3.41^{+0.53}_{-0.75}$	20±2	3	-
SPT-CL J0242−3123	40.6110	−31.3992	4.42	0.25	0.499±0.007	$3.49^{+0.56}_{-0.78}$	43±3	3	-
SPT-CL J0244−2246	41.2402	−22.7825	4.68	0.25	0.96±0.02	$3.43^{+0.58}_{-0.76}$	64±6	3	-
SPT-CL J0245−2622	41.3516	−26.3756	4.02	1.25	0.138±0.005	$3.98^{+0.62}_{-0.87}$	25±2	3	-
SPT-CL J0249−3636	42.3244	−36.6030	4.86	0.75	0.69±0.02	$3.54^{+0.63}_{-0.75}$	40±4	3	-
SPT-CL J0251−2457	42.8439	−24.9606	4.31	1.25	0.120±0.005	$4.15^{+0.70}_{-0.92}$	88±3	3	-
SPT-CL J0251−2636	42.9824	−26.6036	4.13	1.00	0.353±0.009	$3.82^{+0.60}_{-0.85}$	65±8	3	-
SPT-CL J0252−1959	43.0900	−19.9950	4.98	0.50	0.74±0.02	$3.84^{+0.69}_{-0.83}$	47±4	3	-
SPT-CL J0254−3106	43.5213	−31.1020	4.05	0.50	0.531±0.007	$3.31^{+0.50}_{-0.72}$	61±4	3	-
SPT-CL J0256−3504	44.1048	−35.0757	4.75	0.50	0.75±0.01	$3.42^{+0.56}_{-0.73}$	76±6	3	-
SPT-CL J0257−2009	44.4290	−20.1507	4.88	0.50	0.70±0.01	$3.82^{+0.68}_{-0.83}$	152±6	3	SL
SPT-CL J0258−2613	44.6704	−26.2251	4.25	1.50	0.73±0.01	$3.47^{+0.55}_{-0.76}$	71±4	3	-
SPT-CL J0301−3708	45.4931	−37.1375	4.20	0.25	0.491±0.009	$3.41^{+0.52}_{-0.75}$	26±2	3	-
SPT-CL J0302−3209	45.7042	−32.1586	4.51	2.75	0.322±0.007	$3.72^{+0.63}_{-0.81}$	55±2	3	-
SPT-CL J0303−2736	45.8170	−27.6129	4.76	0.75	0.268±0.006	$4.26^{+0.72}_{-0.92}$	75±5	3	-
SPT-CL J0305−2441	46.3298	−24.6965	4.44	1.25	0.372±0.010	$3.94^{+0.66}_{-0.88}$	67±4	3	-
SPT-CL J0308−2915	47.0287	−29.2578	4.69	1.00	1.01±0.05	$3.39^{+0.55}_{-0.74}$	50±5	7	-
SPT-CL J0308−2947	47.2319	−29.7914	4.57	0.75	0.90±0.02	$3.16^{+0.54}_{-0.70}$	40±4	3	-
SPT-CL J0312−2025	48.1172	−20.4274	4.36	0.50	0.68±0.02	$3.60^{+0.56}_{-0.79}$	49±4	3	-
SPT-CL J0314−2453	48.6625	−24.8922	4.26	0.25	0.41±0.01	$3.83^{+0.60}_{-0.85}$	71±4	3	-
SPT-CL J0316−2046	49.1042	−20.7832	4.89	2.25	0.236±0.004	$4.39^{+0.77}_{-0.93}$	66±3	3	-
SPT-CL J0317−3027	49.4890	−30.4644	4.18	2.25	0.71±0.02	$3.18^{+0.46}_{-0.69}$	56±4	3	-
SPT-CL J0318−2844	49.7493	−28.7464	4.39	0.25	0.92±0.02	$3.35^{+0.54}_{-0.74}$	20±4	3	-
SPT-CL J0322−2500	50.5695	−25.0089	4.26	0.50	0.41±0.01	$3.84^{+0.61}_{-0.83}$	38±3	3	-
SPT-CL J0329−3629	52.3111	−36.4917	4.04	1.75	0.361±0.009	$3.44^{+0.53}_{-0.77}$	50±4	3	-
SPT-CL J0330−3912	52.5489	−39.2105	4.56	0.50	0.543±0.007	$3.52^{+0.58}_{-0.77}$	64±3	3	-
SPT-CL J0330−2948	52.7327	−29.8105	4.45	0.25	0.86±0.02	$3.42^{+0.56}_{-0.76}$	35±4	3	-
SPT-CL J0336−3012	54.0448	−30.2112	4.90	0.25	1.03±0.08	$3.47^{+0.61}_{-0.76}$	33±5	3	-
SPT-CL J0336−3144	54.1887	−31.7345	4.24	0.50	0.42±0.01	$3.48^{+0.55}_{-0.78}$	122±5	3	-
SPT-CL J0338−3742	54.5844	−37.7021	4.87	1.75	0.475±0.008	$3.76^{+0.66}_{-0.81}$	38±3	3	-
SPT-CL J0339−3952	54.7938	−39.8734	4.64	0.25	1.24±0.07	$2.88^{+0.47}_{-0.63}$	-	7	-
SPT-CL J0339−2205	54.9318	−22.0992	4.43	2.50	0.256±0.005	$4.09^{+0.67}_{-0.90}$	56±4	3	-
SPT-CL J0340−2855	55.1962	−28.9299	4.17	0.50	0.326±0.008	$3.84^{+0.61}_{-0.86}$	23±3	3	-
SPT-CL J0340−2823	55.2270	−28.3862	4.28	1.00	0.350±0.009	$3.90^{+0.63}_{-0.87}$	48±3	3	-
SPT-CL J0340−2805	55.2448	−28.0999	4.02	0.25	0.462±0.009	$3.65^{+0.56}_{-0.81}$	33±3	3	-
SPT-CL J0346−2127	56.6939	−21.4545	4.71	0.50	0.69±0.01	$3.74^{+0.66}_{-0.83}$	59±5	3	-
SPT-CL J0350−3801	57.6594	−38.0256	4.35	0.75	0.38±0.01	$3.59^{+0.60}_{-0.80}$	58±4	3	-
SPT-CL J0356−3602	59.0954	−36.0421	4.41	0.25	0.77±0.01	$3.22^{+0.51}_{-0.71}$	59±7	3	-
SPT-CL J0359−3011	59.8978	−30.1892	4.64	0.25	0.113±0.005	$4.48^{+0.78}_{-0.98}$	33±3	3	-
SPT-CL J0400−2914	60.1335	−29.2445	4.82	0.25	0.79±0.01	$3.81^{+0.67}_{-0.82}$	92±7	3	-
SPT-CL J0413−2748	63.2874	−27.8097	4.18	0.25	0.61±0.01	$3.65^{+0.59}_{-0.80}$	42±3	3	-
SPT-CL J0418−3504	64.7175	−35.0833	4.04	0.25	0.294±0.008	$3.87^{+0.59}_{-0.87}$	27±2	3	-
SPT-CL J0420−3837	65.0115	−38.6212	4.21	0.50	0.349±0.009	$3.92^{+0.60}_{-0.87}$	39±3	3	SL
SPT-CL J0420−2710	65.0950	−27.1718	4.15	1.25	0.44±0.01	$3.85^{+0.60}_{-0.85}$	54±3	3	-
SPT-CL J0421−2753	65.2684	−27.8865	4.24	0.25	0.611±0.010	$3.68^{+0.58}_{-0.82}$	48±3	3	-

Table 9 *continued*

Table 9 *(continued)*

SPT ID	R.A.	Decl.	Best		Redshift	M_{500c}	λ	Imaging	Notes
	(J2000)	(J2000)	ξ	θ_c		$(10^{14}h_{70}^{-1}M_\odot)$			
SPT-CL J0421−2022	65.3372	−20.3831	4.63	0.75	0.389±0.010	$4.16^{+0.73}_{-0.93}$	141±4	3	-
SPT-CL J0423−3644	65.7701	−36.7372	4.38	0.25	0.541±0.006	$3.76^{+0.64}_{-0.85}$	80±4	3	-
SPT-CL J0426−3648	66.5965	−36.8017	4.00	1.25	0.40±0.01	$3.77^{+0.56}_{-0.81}$	48±4	3	-
SPT-CL J0427−2441	66.8854	−24.6936	4.59	1.75	0.41±0.01	$4.11^{+0.72}_{-0.90}$	51±3	3	-
SPT-CL J0428−3002	67.0420	−30.0391	4.11	1.00	0.98±0.03	$3.21^{+0.46}_{-0.70}$	49±6	3	-
SPT-CL J0428−3014	67.1185	−30.2438	4.60	0.75	0.93±0.02	$3.51^{+0.60}_{-0.77}$	34±7	3	-
SPT-CL J0433−3942	68.3179	−39.7038	4.11	1.50	0.339±0.009	$3.86^{+0.62}_{-0.87}$	27±3	3	-
SPT-CL J0434−2227	68.6864	−22.4528	4.13	0.50	0.88±0.02	$3.37^{+0.51}_{-0.75}$	35±4	3	-
SPT-CL J0437−2449	69.3041	−24.8317	4.95	0.25	1.01±0.06	$3.63^{+0.61}_{-0.78}$	47±5	7	-
SPT-CL J0438−2210	69.6687	−22.1764	4.25	3.00	0.095±0.006	$4.25^{+0.71}_{-0.95}$	50±4	3	-
SPT-CL J0440−3353	70.2323	−33.8836	4.34	0.50	0.514±0.007	$3.80^{+0.60}_{-0.84}$	52±3	3	-
SPT-CL J0441−3817	70.2698	−38.2961	4.16	1.00	0.222±0.004	$4.00^{+0.63}_{-0.90}$	68±5	3	-
SPT-CL J0445−2510	71.2805	−25.1684	4.12	1.25	0.585±0.007	$3.67^{+0.57}_{-0.82}$	61±4	3	-
SPT-CL J0445−1950	71.3557	−19.8385	4.46	0.25	0.42±0.01	$4.01^{+0.68}_{-0.90}$	35±3	3	-
SPT-CL J0448−3020	72.0507	−30.3359	4.17	1.00	0.75±0.01	$3.47^{+0.55}_{-0.76}$	83±5	3	SL
SPT-CL J0448−2909	72.0985	−29.1577	4.93	1.00	0.299±0.007	$4.49^{+0.78}_{-0.93}$	46±4	3	-
SPT-CL J0448−2718	72.1646	−27.3019	4.10	0.25	0.39±0.01	$3.87^{+0.62}_{-0.86}$	44±4	3	-
SPT-CL J0453−3933	73.3914	−39.5531	4.60	0.25	0.525±0.007	$3.93^{+0.66}_{-0.85}$	82±7	3	-
SPT-CL J0453−3405	73.4587	−34.0998	4.70	0.25	1.21±0.15	$3.22^{+0.54}_{-0.72}$	-	6	-
SPT-CL J0456−3836	74.1795	−38.6143	4.30	1.25	0.40±0.01	$3.90^{+0.63}_{-0.88}$	54±5	3	-
SPT-CL J0458−3710	74.6327	−37.1706	4.10	1.25	0.74±0.01	$3.46^{+0.52}_{-0.75}$	70±4	3	-
SPT-CL J0458−2706	74.6424	−27.1048	4.63	0.50	0.558±0.006	$4.00^{+0.67}_{-0.86}$	79±5	3	-
SPT-CL J0502−3104	75.5621	−31.0722	4.11	1.00	0.72±0.02	$3.47^{+0.53}_{-0.76}$	54±4	3	-
SPT-CL J0503−3553	75.7879	−35.8929	4.12	0.75	0.63±0.01	$3.53^{+0.54}_{-0.80}$	85±5	3	-
SPT-CL J0505−3335	76.4319	−33.5968	4.49	0.25	0.65±0.01	$3.70^{+0.63}_{-0.85}$	50±4	3	-
SPT-CL J0506−2551	76.5394	−25.8521	4.60	0.50	0.38±0.01	$4.16^{+0.71}_{-0.91}$	61±3	3	-
SPT-CL J0516−2749	79.2139	−27.8303	4.14	0.25	0.99±0.03	$3.29^{+0.47}_{-0.70}$	21±4	3	-
SPT-CL J0517−3221	79.2564	−32.3546	4.26	2.00	0.168±0.005	$4.11^{+0.68}_{-0.92}$	27±3	3	-
SPT-CL J0517−2037	79.3416	−20.6231	4.80	0.25	1.03±0.09	$3.50^{+0.62}_{-0.78}$	-	3	-
SPT-CL J0519−3930	79.9642	−39.5125	4.06	0.50	0.40±0.01	$3.77^{+0.58}_{-0.86}$	31±3	3	-
SPT-CL J0520−2625	80.1113	−26.4298	4.31	0.50	0.276±0.006	$4.11^{+0.67}_{-0.92}$	77±4	3	-
SPT-CL J0521−2812	80.3767	−28.2127	4.93	0.25	0.598±0.009	$4.10^{+0.71}_{-0.89}$	50±4	3	-
SPT-CL J0524−2507	81.2213	−25.1275	4.22	1.75	0.74±0.02	$3.56^{+0.54}_{-0.78}$	45±4	3	-
SPT-CL J0528−3328	82.2466	−33.4772	4.36	1.00	0.43±0.01	$3.89^{+0.65}_{-0.86}$	22±5	3	-
SPT-CL J0533−3713	83.2840	−37.2245	4.34	0.25	0.97±0.02	$3.30^{+0.52}_{-0.75}$	42±6	3	-
SPT-CL J0536−3055	84.0106	−30.9247	4.13	3.00	0.75±0.02	$3.45^{+0.52}_{-0.75}$	25±4	3	-
SPT-CL J0536−3946	84.0439	−39.7731	4.67	0.50	0.266±0.005	$4.26^{+0.73}_{-0.93}$	80±4	3	-
SPT-CL J0538−2924	84.5920	−29.4151	4.81	0.25	0.356±0.009	$4.33^{+0.76}_{-0.93}$	39±3	3	-
SPT-CL J0538−2540	84.6743	−25.6692	4.45	1.25	0.609±0.010	$3.78^{+0.61}_{-0.85}$	48±4	3	-
SPT-CL J0543−3210	85.8831	−32.1783	4.24	1.00	0.98±0.03	$3.27^{+0.49}_{-0.72}$	35±5	3	-
SPT-CL J0544−2842	86.0724	−28.7163	4.02	0.75	0.493±0.008	$3.73^{+0.55}_{-0.83}$	44±3	3	-
SPT-CL J0546−3139	86.5928	−31.6509	4.48	0.25	0.76±0.01	$3.60^{+0.60}_{-0.79}$	81±5	3	-
SPT-CL J0546−2013	86.6206	−20.2241	4.81	0.50	0.584±0.007	$4.02^{+0.70}_{-0.87}$	100±5	3	-
SPT-CL J0546−4017	86.6537	−40.2961	4.62	0.75	0.44±0.01	$4.03^{+0.70}_{-0.89}$	19±3	3	-
SPT-CL J0547−2916	86.8424	−29.2750	4.69	2.50	0.43±0.01	$4.15^{+0.72}_{-0.91}$	47±4	3	-

Table 9 *continued*

Table 9 *(continued)*

SPT ID	R.A.	Decl.	Best		Redshift	M_{500c}	λ	Imaging	Notes
	(J2000)	(J2000)	ξ	θ_c		$(10^{14} h_{70}^{-1} M_\odot)$			
SPT-CL J0552−4008	88.1231	−40.1363	4.36	2.00	0.363±0.009	$3.95^{+0.65}_{-0.90}$	66±5	3	-
SPT-CL J0554−3149	88.5286	−31.8306	4.62	0.25	0.218±0.005	$4.29^{+0.73}_{-0.94}$	21±3	3	-
SPT-CL J0556−2502	89.1563	−25.0424	4.13	0.25	0.62±0.01	$3.64^{+0.54}_{-0.81}$	20±3	3	-
SPT-CL J0557−2626	89.3717	−26.4374	4.01	0.75	0.598±0.009	$3.62^{+0.54}_{-0.80}$	45±4	3	-
SPT-CL J0559−2628	89.7502	−26.4826	4.09	1.25	0.275±0.006	$3.98^{+0.62}_{-0.89}$	91±4	3	-
SPT-CL J1015−2604	153.8879	−26.0716	4.60	0.75	0.38±0.04	$4.76^{+0.83}_{-1.03}$	-	1	-
SPT-CL J1022−2337	155.7469	−23.6277	4.37	0.25	0.41±0.04	$4.57^{+0.78}_{-1.00}$	-	2	RC
SPT-CL J1025−2041	156.2867	−20.6880	4.19	2.00	0.31±0.02	$4.61^{+0.74}_{-1.01}$	-	2	-
SPT-CL J1039−2609	159.8641	−26.1622	4.58	0.75	0.41±0.04	$4.70^{+0.76}_{-1.03}$	-	2	-
SPT-CL J1042−2142	160.6896	−21.7163	4.62	1.25	0.47±0.05	$4.67^{+0.81}_{-1.00}$	-	1	-
SPT-CL J1042−2012	160.7066	−20.2083	4.64	0.25	0.33±0.05	$4.87^{+0.81}_{-1.05}$	-	1	-
SPT-CL J1113−2214	168.3704	−22.2382	4.63	0.25	0.46±0.04	$4.68^{+0.81}_{-1.02}$	-	1	-
SPT-CL J1126−2046	171.5991	−20.7753	4.77	2.50	0.64±0.04	$4.51^{+0.81}_{-1.00}$	-	1	-
SPT-CL J1141−2127	175.4930	−21.4629	4.83	1.50	0.30±0.02	$5.01^{+0.90}_{-1.08}$	-	2	SL
SPT-CL J1204−2814	181.0500	−28.2361	4.65	0.25	0.141	$4.29^{+0.76}_{-0.93}$	-	8	-
SPT-CL J1217−2928	184.3107	−29.4804	4.66	1.00	0.20±0.03	$4.26^{+0.76}_{-0.93}$	-	1	-
SPT-CL J1239−2915	189.7973	−29.2603	4.61	1.75	0.65±0.04	$3.73^{+0.63}_{-0.82}$	-	2	SL
SPT-CL J1251−2230	192.7899	−22.5053	4.38	0.75	0.045	$4.22^{+0.71}_{-0.94}$	-	8	-
SPT-CL J1251−2308	192.8977	−23.1401	4.47	0.25	0.29±0.05	$4.06^{+0.69}_{-0.90}$	-	1	-
SPT-CL J1252−2711	193.0096	−27.1926	4.59	0.50	0.43±0.04	$3.97^{+0.68}_{-0.88}$	-	1	RC
SPT-CL J1254−2408	193.5557	−24.1344	4.40	0.25	0.65±0.04	$3.62^{+0.60}_{-0.80}$	-	2	-
SPT-CL J1259−2129	194.9025	−21.4986	4.83	0.25	0.65±0.06	$3.85^{+0.67}_{-0.84}$	-	1	-
SPT-CL J1309−2244	197.3718	−22.7484	4.75	0.75	0.35±0.04	$4.14^{+0.73}_{-0.91}$	-	1	RC
SPT-CL J1312−2505	198.2329	−25.0925	4.40	0.25	0.63±0.04	$3.66^{+0.58}_{-0.81}$	-	2	-
SPT-CL J1332−2017	203.0721	−20.2878	4.77	0.25	0.55±0.05	$3.92^{+0.69}_{-0.86}$	-	1	-
SPT-CL J1341−2346	205.4910	−23.7710	4.86	0.50	0.21±0.04	$4.39^{+0.77}_{-0.94}$	-	1	-
SPT-CL J2159−2846	329.9360	−28.7745	4.72	2.00	0.43±0.04	$4.24^{+0.70}_{-0.92}$	-	1	-
SPT-CL J2204−2515	331.2228	−25.2517	4.43	1.75	0.213	$4.30^{+0.73}_{-0.94}$	-	8	-
SPT-CL J2213−2806	333.3115	−28.1065	4.89	0.50	0.75±0.05	$3.94^{+0.71}_{-0.85}$	-	1	-
SPT-CL J2218−3227	334.5189	−32.4524	4.66	0.25	0.97±0.14	$3.62^{+0.62}_{-0.81}$	-	6	-
SPT-CL J2219−2809	334.8726	−28.1534	4.61	0.25	0.18±0.05	$4.44^{+0.77}_{-0.96}$	-	1	-
SPT-CL J2236−2458	339.0403	−24.9738	4.82	1.25	0.32±0.05	$4.42^{+0.78}_{-0.94}$	-	1	-
SPT-CL J2238−2452	339.6265	−24.8725	4.61	1.25	0.44±0.04	$4.14^{+0.70}_{-0.91}$	-	1	-
SPT-CL J2238−2458	339.6890	−24.9707	4.76	0.75	0.218	$4.49^{+0.79}_{-0.96}$	-	8	-
SPT-CL J2251−2037	342.7878	−20.6261	4.66	0.25	0.80±0.20	$3.74^{+0.64}_{-0.82}$	-	1	-
SPT-CL J2259−2615	344.9579	−26.2596	4.32	1.25	0.68±0.04	$3.66^{+0.59}_{-0.84}$	-	2	-
SPT-CL J2305−2451	346.4351	−24.8609	4.56	0.50	0.48±0.05	$4.06^{+0.69}_{-0.90}$	-	1	-
SPT-CL J2312−2130	348.0778	−21.5149	4.88	1.00	0.109	$4.70^{+0.85}_{-0.99}$	-	8	-
SPT-CL J2326−2255	351.6831	−22.9213	4.71	0.50	0.83±0.06	$3.73^{+0.65}_{-0.82}$	-	1	-
SPT-CL J2331−2033	352.8570	−20.5595	4.44	0.25	0.149	$4.38^{+0.74}_{-0.95}$	-	8	-
SPT-CL J2352−2525	358.0919	−25.4179	4.53	1.50	0.42±0.05	$4.10^{+0.71}_{-0.90}$	-	1	-
SPT-CL J2353−2547	358.2635	−25.7847	4.60	1.00	0.48±0.04	$4.08^{+0.73}_{-0.90}$	-	2	-

NOTE—The same as Table 8 now for confirmed candidates at $4 < \xi < 5$.

Table 10. Newly confirmed galaxy clusters at $\xi > 4.5$ in the SPT-SZ Survey.

SPT ID	R.A.	Decl.	Best		Redshift	M_{500c}	λ
	(J2000)	(J2000)	ξ	θ_c		$(10^{14} h_{70}^{-1} M_\odot)$	
SPT-CL J2352−5846	358.0510	−58.7758	5.18	0.75	0.167±0.006	$3.86^{+0.67}_{-0.77}$	23±6
SPT-CL J0013−5714	3.3029	−57.2373	5.11	1.50	0.63±0.01	$3.70^{+0.67}_{-0.76}$	29±3
SPT-CL J2328−4616	352.0576	−46.2802	4.84	2.75	0.224±0.005	$3.94^{+0.70}_{-0.84}$	25±3
SPT-CL J0048−4450	12.1743	−44.8475	4.82	0.50	0.595±0.009	$3.55^{+0.61}_{-0.77}$	55±5
SPT-CL J2339−4058	354.7996	−40.9697	4.75	0.25	0.60±0.01	$3.50^{+0.61}_{-0.76}$	31±3
SPT-CL J2136−5723	324.1203	−57.3968	4.72	1.00	0.284±0.007	$3.65^{+0.63}_{-0.78}$	42±3
SPT-CL J2158−4851	329.5692	−48.8533	4.64	0.25	0.490±0.008	$3.69^{+0.65}_{-0.82}$	58±6
SPT-CL J0501−4455	75.2932	−44.9270	4.59	0.25	0.433±0.010	$3.80^{+0.65}_{-0.85}$	80±5
SPT-CL J0353−5312	58.3058	−53.2095	4.54	0.25	0.65±0.01	$3.24^{+0.54}_{-0.70}$	31±3
SPT-CL J0323−4913	50.9166	−49.2215	4.54	0.50	0.37±0.01	$3.51^{+0.59}_{-0.77}$	29±3
SPT-CL J0437−5307	69.2599	−53.1206	4.52	0.25	0.301±0.007	$3.54^{+0.60}_{-0.79}$	38±3
SPT-CL J0500−4551	75.2108	−45.8564	4.51	0.75	0.242±0.005	$3.96^{+0.68}_{-0.88}$	38±4
SPT-CL J0250−4714	42.6656	−47.2385	4.50	1.25	0.475±0.008	$3.50^{+0.57}_{-0.77}$	39±3

Note—SPT-SZ clusters newly confirmed using the RM algorithm in "scanning mode", see Section 4.2.1. When overlapping, column entries match Table 8.